Microsystems for *C. elegans* Mechanics and Locomotion Study

Shazlina Johari

A thesis submitted in partial fulfilment
of the requirements for the degree of
Doctor of Philosophy
in
Mechanical Engineering
at the
University of Canterbury
Christchurch, New Zealand
April 2013

To my parents, Johari and Zaleha,
for their unconditional love and support throughout.

Abstract

Studying animal mechanics is crucial in order to understand how signals in the neuromuscular system contribute to an organism's behaviour and how force-sensing organs and sensory neurons interact. In particular, the connection between the nerves and the muscles responsible for the force generation in the neuromuscular system needs to be established. Knowledge of the locomotion forces can be beneficial for the development of therapies for muscle disorders, neurodegenerative and human genetic diseases, such as muscular dystrophy. The simplicity of the nematode *Caenorhabditis elegans*' (*C. elegans*) nervous system, which is limited to 302 neurons, has made it an excellent model organism for studying animal mechanics which include mechanosensation and locomotion at the neuronal level.

The advent of miniaturized force sensing devices has led to the proposal of various approaches for measuring *C. elegans* locomotion forces. However, these existing devices are relatively complex, involving complicated microfabrication procedures and are incapable of measuring forces exerted by *C. elegans* in motion. This thesis addresses these shortcomings by introducing a force sensor capable of continuously measuring the forces generated by *C. elegans* in motion. The system consists of a micropillar-based device made of polydimethylsiloxane (PDMS) only and a vision-based algorithm for resolving the worm force from the deflection of the cantilever-like pillars. The measured force is horizontal and equivalent to a point force acting at half of the pillar height. The microdevice, sub-pixel resolution for visual tracking of the deflection, and experimental technique form an integrated system for measuring dynamic forces of moving *C. elegans* with force resolution of 3.13 μN for worm body width of 100 μm. A simple device fabrication process based on soft-lithography and a basic experimental setup, which only requires a stereo microscope with off-the-shelf digital camera mean that this method is accessible to most biological science laboratories.

The results demonstrate that the proposed device is capable of quantifying multipoint forces of moving *C. elegans* rather than single-point forces for a worm sample. This allows one to simultaneously collect force data from up to eight measurements points on different worm body parts. This is a significant step forward

as it enables researchers to explicitly quantify the relative difference in forces exerted by the worm's different body segments during the worms' movements. The device's capability to determine multipoint forces during nematode motion can also generate meaningful data to compare forces associated with different worm body muscles, gaining new understanding on how these muscles function. The forces measured during locomotion in the micropillars could also be used to differentiate mutant phenotypes. Apart from locomotion forces, the device is also capable of conducting concurrent measurement of other locomotion parameters such as speed, body amplitude and wavelength, as well as undulation frequency. This additional information can be useful to further quantify phenotypic behaviour of *C. elegans* and deepen the understanding of the theory behind worm locomotion forces.

The relationship between *C. elegans* locomotion forces and their environment has also been analyzed by variation of the pillar arrangement and spacing. The results indicate that the microstructured environment significantly affects the worm's contraction force, locomotion speed and the undulation frequency. In addition, an alternative measurement technique was provided to measure worm forces on other substrates, such that worm locomotion behaviour in varying environments can be investigated further. The combination of the conventional measurement technique with the findings of worm locomotion on a glass substrate reported show promise for biological measurements and other sensing application such as tactile force. Additional functions of on-chip worm selection, sorting, and imaging have also been integrated with the device, rendering its potential to accommodate for high-throughput application of *C. elegans* force measurement and locomotion studies in the future.

The primary contributions of this thesis are centered around four topics: the development of the PDMS micropillar array and its application to study *C. elegans* locomotion forces, the analysis of *C. elegans* muscular forces and locomotion patterns in microstructured environments, the investigation of the worm locomotion forces using different substrates and finally the integration of the PDMS micropillar with PDMS microvalve for on-chip worm selection and imaging. Although the results presented in this thesis focus on wild type *C. elegans*, the method can be easily applied to its mutants and other organisms.

Acknowledgements

First and foremost, I would like to thank Dr. Wenhui Wang for the given opportunity to work on this research and introducing me to the world of research life. Your constant guidance, patience and high expectations always motivate me to be a better researcher and produce work of a good quality. Your professional direction and genuine care for my best interests have made my days as a postgraduate student both pleasant and productive.

To Dr. Volker Nock, I am extremely lucky to have you as part of my supervisory team. Thank you for introducing me to SU-8 and PDMS, and teaching me the fabrication method necessary to complete this thesis. I learned a lot from you especially when working my way around in the fabrication lab. You are always full of ideas and your enthusiasm for this project sometimes makes me believe you are the one who is doing this research. You are always there for questions and discussions. In my moments of deepest doubt, you lifted me up with your words of encouragement and those delicious chocolate brownies. Your hard work and tenacity will always stand as a model for me.

To Dr. Sid Becker, thank you for helping me during the final stage of my PhD. Your sense of humor and awesomeness will always be remembered. I enjoyed every single minute of working on my thesis writing with you. I thank you for your patience and guidance in editing and proof reading my thesis for this past 8 months.

I would also like to thank and acknowledge Associate Professor Maan Alkaisi and Professor XiaoQi Chen for their feedbacks and comments, and always being helpful and supporting my research potential.

I would like to thank the brilliant people working in the Nanofabrication Laboratory, especially Helen Devereux and Gary Turner for their technical assistance. To Julian Murphy, thank you for your technical guidance and help in the Mechatronics Research Lab. To Craig Galilee, thank you for your help in the maintenance and

culture of the worms. Without you, I would have never managed to keep the worms alive for these past three years.

I would also like to gratefully acknowledge the Ministry of Higher Education Malaysia (MOHE) and Universiti Malaysia Perlis (UniMAP) for their financial support.

To my officemates: Robert, Ali, Mostafa, Craig, Michael, Prateek, Steve, Sayyed, and Syafiq thank you for your companion and making the work environment enjoyable and productive. To Mervin in particular, thank you for your constant critics, help, inputs and knowledge. Special thanks also to my friends and colleagues who have made living in New Zealand such a great experience.

Finally, to my parents, family and close friends back home, thank you for your unconditional and unwavering support and encouragement. I look forward to seeing you all soon.

Abbreviations

Abbreviations used in this thesis are listed here for easy reference.

AFM	atomic force microscopy
ALML	anterior lateral microtubule cell left
ALMR	anterior lateral microtubule cell right
AVM	anterior ventral microtubule cell
DI	de-ionized
DP	detection points
DRIE	deep reactive-ion etching
DXF	drawing interchange format
FPGA	field-programmable gate array
IPA	Isopropyl alcohol
LB	Lysogeny broth
LSCD	least-square circle detection
MEMS	microelectro-mechanical system
MMF	multimode fiber
NGM	nematode growth medium
PDMS	polydimethylsiloxane
PEB	post-exposure bake
PGMEA	(1-methoxy-2-propyl) acetate
PLML	posterior lateral microtubule cell left
PLMR	posterior lateral microtubule cell right
PVM	posterior ventral microtubule cell
RIE	reactive ion etching
SMF	single mode fiber
SEM	scanning electron microscopy
TMCS	trimethylchlorosilane
UV	ultraviolet

Publications and Presentations

Johari, S., Nock, V., Alkaisi, M.M. and Wang, W. (2013)
On-chip analysis of *C. elegans* muscular forces and locomotion patterns in microstructured environments. *Lab on a Chip* vol. 13, pp. 1699-707.

Ghanbari, A.[*], Nock, V.[*], **Johari, S**.[*], Blaikie, R.J., Chen, X-Q. and Wang, W. (2012)
A micropillar-based on-chip system for continuous force measurement of *C. elegans*. *Journal of Micromechanics and Microengineering* 22(9): 095009. ([*]equal contributions)

Johari, S., Nock, V., Alkaisi, M.M. and Wang, W. (2012)
Elastomeric pillar arrays for integrated measurement of *C. elegans* locomotion forces. *Proceedings of MicroTAS 2012.*

Johari, S., Nock, V., Alkaisi, M.M. and Wang, W. (2011)
High-Throughput Microfluidic Sorting of *C. elegans* for Automated Force Pattern Measurement. *Materials Science Forum* 700: 182-187.

Johari, S., Nock, V., Alkaisi, M.M. and Wang, W. (2012)
Elastomeric pillar arrays for integrated measurement of *C. elegans* locomotion forces. Okinawa, Japan: 16th International Conference on Miniaturized Systems for Chemistry and Life Sciences (MicroTAS 2012), 28 Oct-1 Nov 2012. (Poster presentation)

Johari, S., Nock, V., Alkaisi, M.M. and Wang, W. (2011)
Worms on a chip - High-throughput Microfluidic Sorting of *C. elegans* for Automated Force Pattern Measurement. Wellington, New Zealand: 5th International Conference on Advanced Materials and Nanotechnology (AMN-5), 7-11 Feb 2011. (Poster presentation)

Johari, S., Nock, V., Alkaisi, M.M. and Wang, W. (2011)

Microfluidic for *C. elegans* sorting and automated force pattern measurement. Sydney, Australia: 2nd Australian and New Zealand Micro and Nanofluidics Symposium, 14-15 April 2011. (Oral presentation)

Johari, S., Nock, V., Alkaisi, M.M. and Wang, W. (2012)

C. elegans: Partners is slime. Christchurch, New Zealand: 8th MacDiarmid Institute Student and Post-Doc Symposium, 22-23 November 2012. (Poster presentation)

Johari, S., Nock, V., Alkaisi, M.M. and Wang, W. (2011)

Micropillar-based On-chip System for Dynamic Force Measurement of *C. elegans.* Wellington, New Zealand: 7th MacDiarmid Institute Student and Post-Doc Symposium, 17-18 November 2011. (Poster presentation)

Johari, S., Wang, W., Nock, V., Alkaisi, M.M. and Chen, X. Q. (2010)

High-throughput Microfluidic Sorting of *C. elegans* for Automated Force Pattern Measurement. Wellington, New Zealand: 6th MacDiarmid Institute Student and Post-Doc Symposium, 18-19 November 2010. (Oral presentation)

Johari, S., Wang, W., Nock, V., Alkaisi, M.M. and Chen, X. Q. (2010)

Worms on a chip: High-throughput Microfluidic Sorting of *C. elegans* for Automated Force Pattern Measurement. Christchurch, New Zealand: University of Canterbury College of Engineering Postgraduate Poster Competition, August 2010. Runner-up Best Poster Prize.

Johari, S., Wang, W.H. and Garrill, A. (2009)

Electrical detection of carbon nanopipettes contact with biological cells. Victoria University, Wellington, New Zealand: New Zealand Postgraduate Conference (NZPGC), 20-21 Nov 2009. (Conference Contribution - Poster presentation)

Johari, S., Nock, V., Alkaisi, M.M. and Wang, W. (2012)

Micropillar-based On-chip System for continuous Force Measurement of *C.elegans*. Canterbury University, Christchurch, New Zealand: Nanofabrication Laboratory Group Meeting, University of Canterbury, 9 July 2012. (Oral presentation)

Johari, S., Nock, V., Alkaisi, M.M. and Wang, W. (2011)

Microvalve-based microfluidic device for *C. elegans* force measurement. Canterbury University, Christchurch, New Zealand: Nanofabrication Laboratory Group Meeting, University of Canterbury, 4 October 2011. (Oral presentation)

Johari, S., Nock, V., Alkaisi, M.M. and Wang, W. (2010)

Microsystems for *C. elegans* mechanics and locomotion study. Canterbury University, Christchurch, New Zealand: Nanofabrication Laboratory Group Meeting, University of Canterbury, 24 May 2010. (Oral presentation)

Johari, S., Nock, V., Alkaisi, M.M. and Wang, W. (2009)

Electrical Detection of Carbon Nanopipettes Contact with Biological Cells. Canterbury University, Christchurch, New Zealand: Nanofabrication Laboratory Group Meeting, University of Canterbury, 9 November 2009. (Oral presentation)

Table of Contents

List of Figures

List of Tables

CHAPTER 1

Introduction

1.1 Overview and Objectives

One of the focuses in the field of biology is the study of function, structure, growth and reproduction of living organisms. The practice in this field often adopts a model organism in order to gain insight into the complex behaviours of an organism, or to study human diseases. The choice of using a specific animal model organism depends on the simplicity and validity of the model when conducting experiments for a particular research.

The nematode *C. elegans*, whose main phenotype is locomotion, has been used as a genetic model to investigate the relationship between genes and locomotion behaviour at the neuronal level. This is primarily because of its simple nervous system with only 302 neurons and a fully sequenced genome. Understanding the nervous system, which coordinates the movements/actions and transmits signals between different body parts, can lead to discovering basic mechanisms behind organisms' more complex behaviours. To investigate *C. elegans* locomotion, research has been conducted to quantify the worm's movement force which is induced by the contraction of their body wall muscles. The connection between the nerves and the muscles responsible for the force generation in the neuromuscular system during locomotion can be established. Knowledge of the locomotion forces can also be advantageous for the development of therapy for muscle disorders, neurodegenerative [1] and other genetic diseases observed in humans, such as muscular dystrophy [2-4].

The classical approach to studying *C. elegans* locomotion is to visually observe moving nematodes on a Petri dish. The nematode behaviour and movement patterns are visually inspected and monitored continuously. While this method has been well

established, the process is time consuming, labor intensive, and prone to human error. To overcome these limitations, microfabrication technology and microfluidic devices in particular have been used to conduct worm locomotion force study. Several tools have been developed to quantify the contraction force of the nematode, likewise the development of *C. elegans* force measurement device is still in its early stage, and only three devices designed specifically for the worm have been reported.

This research aims to contribute to the development of miniaturized force-sensing devices for the study of *C. elegans* locomotion forces. In line with this aim, this thesis describes the device design, fabrication and the related force measurement model, experimental setup and analysis of the locomotion forces obtained from systematic study of *C. elegans* motion. The thesis statement of this work is:

"To develop an experimental apparatus employing both novel Polydimethylsiloxane (PDMS) micropillars and a visual feedback system consisting of an optically-based algorithm which resolves the nematode force by quantifying the deflection of the cantilever-like pillar. The sensor is capable of estimating continuous worm forces in motion without the use of strain gauges, which can add considerable complexity. In addition to the dynamic force, the regular structure and transparency of the device allow for measurements of transient effects such as speed, wavelength and wave amplitude which continuously monitor the worm's locomotive behaviour during the entire range of motion. The analysis of* C. elegans*' muscular forces and its locomotion patterns in microstructured environments and on different substrates are also included. The experimental results demonstrate the efficacy of force measurement, leading to preliminary but interesting findings on the* C. elegans *locomotion force patterns. These are: (i) the generated force depends on the worm's head motion, in particular when changing its movement direction, (ii) the worm sinusoidal body shape affects the exhibited force pattern, (iii) the mid-body of the worm generates the maximum force level as predicted by Shen et al. [5], (iv) C. elegans locomotion forces are highly dependent on the structure of the surrounding environment, and (v) C. elegans managed to adapt their natural sinusoidal movement in the microstructured device, despite the existence of PDMS micropillars."

1.2 Thesis Outline and Contributions

The primary contribution of this thesis is focused on four topics: (1) the development of the PDMS micropillar substrate and its application to study *C. elegans* locomotion forces, (2) the analysis of *C. elegans* muscular forces and locomotion patterns in microstructured environments, (3) the investigation of the worm locomotion forces using different substrates and finally (4) the integration of the PDMS micropillar with PDMS microvalve for on-chip worm selection and imaging. In line with the four-fold contribution, nine chapters are organized as follows.

Chapter 2 begins with a comprehensive review of prior works focused on the study of *C. elegans* force mechanics. A brief overview on *C. elegans* and its function as a model organism is presented. This is followed by a review of currently available microfluidic devices for a range of worm applications. An explicit explanation of the motivation behind this work is made in terms of both the novelty of this thesis and the gap in the literature that this work fills. Finally, the contribution of this thesis in developing a novel analytical tool is presented.

Chapter 3 explains the development of the model used to quantify the force that *C. elegans* exerts on the PDMS micropillars, which interprets the force through the experimentally observed pillar deflection by computer vision. The theoretical background behind the force equation and the equivalent force location from the force distributed along the pillar height is introduced. A sensitivity analysis of the equivalent point force measurement model is conducted in order to verify the calculated force from the measured deflection. Description of the image processing algorithm which quantifies the observed deflections is also included in this chapter.

Chapter 4 describes the PDMS device designs and their respective fabrication procedures. The first section explains the features that must be considered when designing the device and the resulting design that was chosen to be used in this research. The fabrication process of the PDMS device is also explained in detail, along with the device casting procedures. The final section discusses the challenges and limitations tackled in this research, in particular during the fabrication process.

Chapter 5 discusses specifically the finalized experimental setup that uses the PDMS device developed in Section 3.8. This includes the device preparation, data collection and the post-processing using a vision-based algorithm in order to resolve the deflection of the micropillars during the worms' movements. The preparation of the *C. elegans* Petri dishes are also discussed in this chapter. Subsequently, the results obtained from the experiment are presented and analyzed. The generated force pattern from the studied locomotion pattern is discussed. To further validate the findings from the results, comparison has been made with published work. The presented work in this chapter demonstrates the potential and applicability of the device which is discussed in the following two chapters.

Chapter 6 investigates the correlation between *C. elegans* locomotion forces and their environment by introducing variation into the microstructured pillar arrangement and spacing. Two different micropillar layouts were investigated, namely the *'Honeycomb'* and *'Lattice'* design structure with the spacing between micropillars for each design also varied. The device introduced in this thesis allows for simultaneous measurements of *C. elegans* locomotion forces, amplitude, wavelength and velocity in the microstructured environment, which are reported in this chapter. In addition to the force measurement capability provided as described in Chapter 5, this chapter highlights the benefits of this device which allow the researcher to take simultaneous measurements from multiple locations on the worm's body: a new development previously unavailable to the research community.

Chapter 7 investigates further into a common scenario that the preceding experimental set up failed to accommodate by performing the worm locomotion study on a different material/substance instead of PDMS. A preliminary investigation on *C. elegans* locomotion forces on a different substrate is conducted. The goal of this chapter is to provide an alternative to the environment parameters used to study *C. elegans* locomotion as discussed from Chapter 3 to Chapter 6. This is achieved by modifying the measurement technique provided by the proposed PDMS device. By inverting the existing PDMS device, the measurement method is modified in a way that the force is calculated based on a point force acting at the pillar tip and the worm's substrate can be varied and is no longer limited to PDMS.

Chapter 8 discusses the combination of the force measurement application with an enhanced capability of worm selection and manipulation. This is accomplished by adding new components to the entire system which consists of a series of controllable microvalves. These microvalves, enabled by a thin PDMS layer and pneumatic supply, function as a switch to select and direct worm movement and at the same time increase the experimental output of the number of force measurement results collected. This technique is also expected to increase the probability of worm survival during experiments and thus to provide higher system throughput. In addition, further integration with complex external control circuits would facilitate the automated operation of the microvalves, leading to size selection and force measurement in a comparable manner.

Chapter 9 summarizes the theories, methods, experimental setup, results and conclusions of the previous eight chapters in this thesis. This is followed by suggestions for continuing this work and a few recommendations for future avenues in this research.

CHAPTER 2

Literature Review

This chapter provides a comprehensive review of the previous work published on the study of *C. elegans* force mechanics. It begins with a brief overview on *C. elegans* and its function as model organism. The primary incentives that drive the field to study the worm's locomotion are provided. This is followed by a survey of currently available microfluidic devices for various worm applications. The shortcomings of each existing method are listed: this provides the gap in the field that this thesis fills. Finally, the contribution of this thesis is explained, which relates the research presented to current *C. elegans* force measurement methods.

2.1 Motivations

Research devoted to the study of *C. elegans* locomotion is imperative in order to fulfil the need of understanding the basic mechanism behind complex behaviours of an organism from the genetic level right up to the system level. *C. elegans* is a microscopic roundworm (nematode) which inhabits in mild soil environments. The average size of adult wild nematode is approximately 1 mm in length and 100 μm diameter (see Fig. 2.1(a)) [6].

In 1963, Nobel Prize winner Sydney Brenner introduced *C. elegans* as a genetic model organism to address fundamental neurobiological questions [6]. This is because *C. elegans* has a simple nervous system with fully mapped 302 neurons compared to human (more than 1000 billion [7]). An additional benefit of *C. elegans* is that it has a short life cycle which makes it fast and convenient to be maintained in a laboratory within a Petri dish (see Fig. 2.1(b)). A typical Escherichia coli (*E. coli)* spread-Petri dish contains about 10,000 worms. The transparency of the nematodes' body enables every nucleus in the worm to be imaged using light microscopy. This allows the study

of biological processes at the resolution of a single cell. Subsequently, *C. elegans* has been widely used in research laboratories as an excellent model for study of neurodevelopment [8].

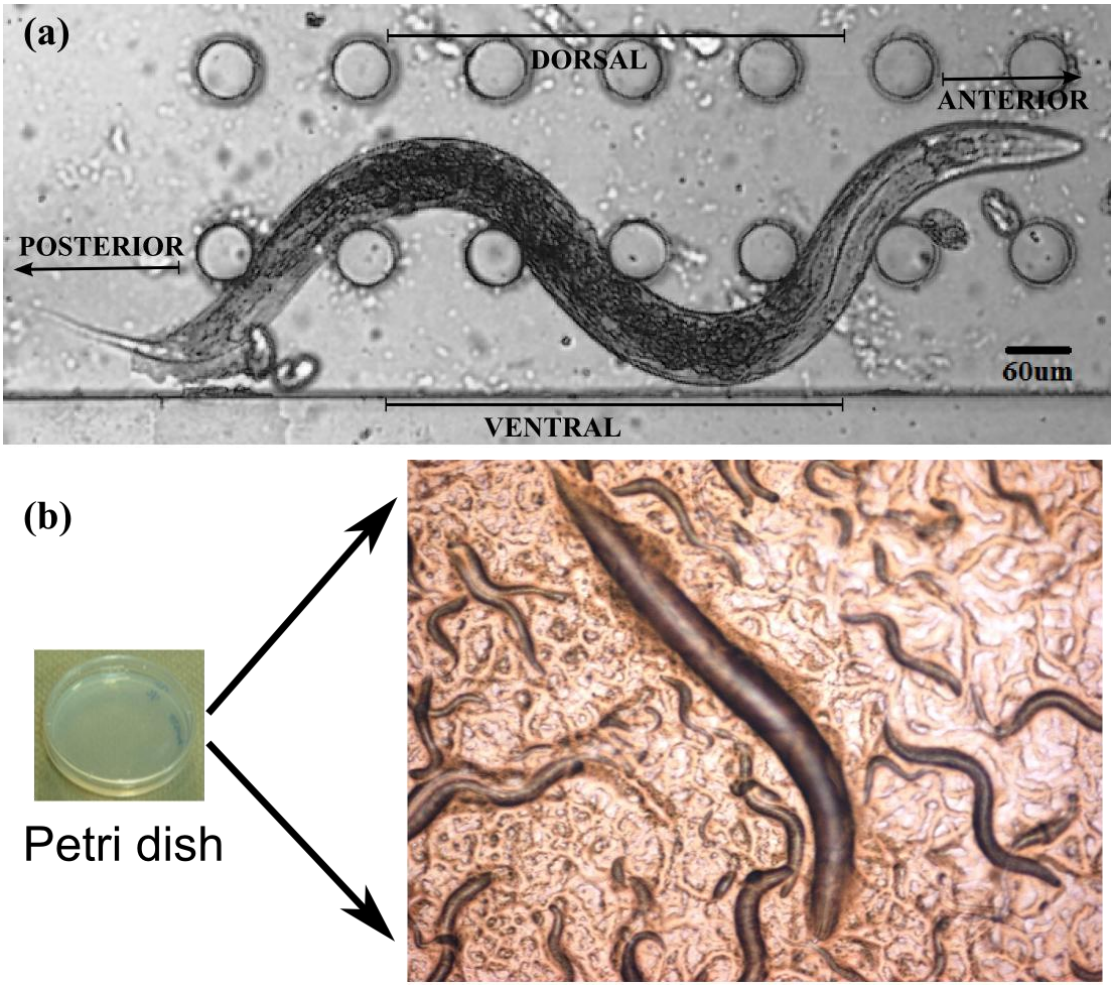

Figure 2.1: *The nematode* C. elegans. *(a) A young adult* C. elegans *crawling inside PDMS micropillar device (b) The typical habitat of* C. elegans *is in a Petri dish cultured in a laboratory on the surface of agar that has been seeded with E. coli. The inset shows worms of mixed ages.*

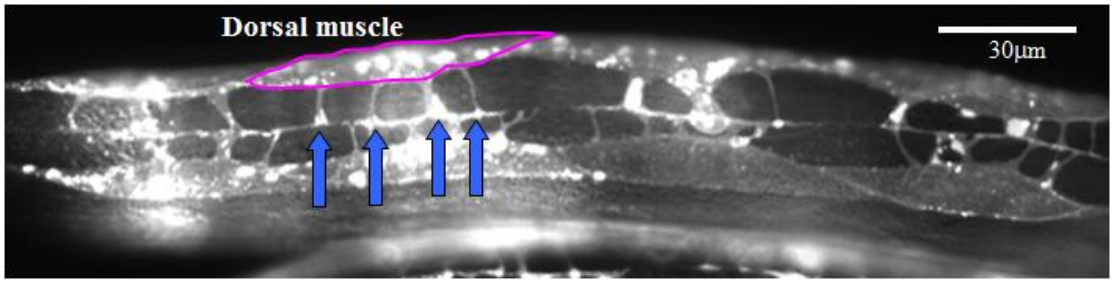

Figure 2.2: *Four muscle arms indicated by blue arrows in young adult* C. elegans. *Image adapted from Dixon and Roy [9].*

The *C. elegans* nematode is a model organism whose main physical trait is locomotion [6]. Because of its simple nervous system and a fully-sequenced genome, the worm has served predominantly as an excellent model organism for studying mechanosensation and locomotion at the neuronal level. The worm's locomotion is controlled by its nervous system, where its neural circuits produce and regulate the muscle activity that actuates *C. elegans* movement. In order to investigate the neuronal mechanisms of *C. elegans* locomotion, the worm locomotion behavior has been analyzed by Shingai et al. [10] for a period of time using an automatic tracking system. By using laser ablation, they found that the regulation of the worm locomotion involved nine sensory neurons and four interneurons; where loss of any one of these neurons will affect the worm locomotion. The same group also developed an automated tracking system to analyze the worm locomotion [11]. The system was able to identify *C. elegans* locomotion patterns such as forward and backward motion, rest, and curl from 230 wild-type and 22 mutants with error less than 1%.

One of the active component involves in the locomotion subsystem of the worm is its body wall muscles. *C. elegans* body wall muscles consist of 95 muscle cells. These muscle cells are arranged in four quadrants along the length of the worm body (see Fig. 2.1) [9]. Each muscle typically has three to five muscle arms, which consists of a thin stalk that originate from the cell body with branches that contact the nerve cord. Figure 2.2 shows an example of *C. elegans* muscle arms indicated by the four arrows. The muscle arms function as pathways for the body wall muscles to receive stimulation from the nerve [9].

The influence of muscle arms on the locomotion of the nematodes is yet to be fully understood. Thanks to genetic manipulation, in particular at the neuronal level, the development of the muscle arm in *C. elegans* has been investigated by Dixon and Roy[9] by creating mutants with variation in the muscle arms characteristics. The characterization of such mutations has been valuable in understanding the correlation between the muscle arms and the worm locomotion forces. In the study conducted by Wang et al. [12], a positive relationship was found to exist between the number of muscle arms and the amplitude of the waves that *C. elegans* exhibit during locomotion. Since the wave amplitude is generated from the contraction force of the

dorsal-ventral muscles, it is of significant interest to investigate the correlation between the contraction force and the wave amplitude. Aside from this, there are several other motivations behind the research interest in the nematode locomotion, in particular the locomotion forces generated from the contraction of the worm's body wall muscle. These include:

(i) Studying animal mechanics is crucial in order to understand how signals in the neuromuscular system contribute to the organism behaviour and how force-sensing organs and sensory neurons work. The connection between the nerves and the muscles responsible for the force generation in the neuromuscular system can be established. This is advantageous for the development of therapy for muscle disorders, neurodegenerative diseases [1] and humans genetic disease such as muscular dystrophy [2-4].

(ii) To assist in the field of neuromechanics, which investigate how the brain, muscles, sensing organs, and motor pattern generators, interact in order to produce coordinated movement. This can improve treatment of human health problems e.g. movement recovery following brain or spinal cord injury [13].

(iii) Drug resistance screening application. Because drug resistance of the worms may be affiliated with the variation in the signalling-muscle-contraction pathways in the worm's body as shown by [14, 15], it is possible to monitor the drug resistance using the nematode as an animal model by determining the muscular locomotion forces of *C. elegans* under different drug or chemical exposure.

(iv) To validate the phenotypic effects of genetic modification as it can create mutants with different muscles and locomotion behaviour characteristics compared to wild type species. Therefore a force sensor compatible with the worm size is required in order to identify the muscular force of these mutants.

In order to quantify the contraction force, a dedicated force sensor compatible with the worm size (approximately 1 mm in length and 100 μm in width for young adult wild type) is highly desirable. The force sensing device needs to be able to quantify worm locomotion forces with higher precision and accuracy than the existing devices

and simultaneously allow for continuous natural worm movement. Since the nematode *C. elegans* main phenotype is its locomotion, it would be sensible to quantify the dynamic body forces of the nematode while the worm is moving naturally. The ability to instantly measure multi-point forces for a worm sample of *C. elegans* in motion is also critical. This will allow for the generation of multiple worm locomotion force data to be reviewed, hence improving the accuracy of the force measurement results.

2.2 Prior Work

In this section, the existing methods used to perform *C. elegans* force measurement will be reviewed. The limitation of these devices will also be discussed. Since the worm is small (~ 1 mm in length and 100μm in width), the existing sensors used in millimeter and larger scales are not capable of detecting the forces at the micro-Newton level. Force measurements at the micro/nano-scale level are often conducted using microelectro-mechanical system (MEMS) transducers such as capacitive force sensors [16-18] and piezoresistive cantilevers [19, 20]. MEMS force sensors are more cost-effective and provide flexibility for system integration, compared to other cellular force measurement techniques such as optical tweezers [21], atomic force microscopy (AFM) [22], magnetic bead measurement [23] and micropipette aspiration [24]. Nevertheless, the fabrication of MEMS force transducers usually requires the use of silicon micromachining techniques which necessitate complicated facilities hence increasing the fabrication process difficulty. Another limitation with regards to using MEMS force transducers is compatibility of material used in fabrication with biology application which often requires aqueous environments. The use of mathematical model to resolve the worm bending force has also been demonstrated by Shen et al. [5]. By using hydrodynamic model, the nematode internal bending force when crawling on wet agar surfaces was estimated to be 8.5 nN and typically associated with the middle section of the worm body. This method however involved both experiment and modeling using complex mathematic equations.

The introduction of polydimethylsiloxane (PDMS) as a core material for microfluidic devices as well as automated imaging techniques has made it possible to create miniature systems and devices well-suited for the nematode *C. elegans*. Several unique properties of microfluidic devices that make them compatible as *C. elegans* research tools are that: i) they require simple and cheap microfabrication techniques; ii) the use of transparent materials i.e. PDMS enables light transmission for optical imaging; iii) microfluidic devices has the ability to manipulate small amounts of liquids in small dimensions; iv) microfluidic devices also has the scalability to handle a large population of worms in high-throughput fashion; v) it is possible to integrate microfluidic devices with other available technology.

A number of pioneering applications using microfluidic devices technology to perform novel assays on *C. elegans* have been published (see Fig. 2.3) [25-27]. These devices have facilitated numerous experiments related to *C. elegans* behaviour [28-36] and locomotion [37-39], techniques for nematode immobilizing and phenotype screening[40-45], and high-throughput screening and sorting of the worms [46-50]. Nevertheless, because of the lack of force sensing devices used to study *C. elegans* compared to the wide range of tools used in the studies of cell mechanics, the current field is still behind in this particular domain. In the next sections, the existing microdevices developed to quantify *C. elegans* locomotion forces will be discussed and reviewed.

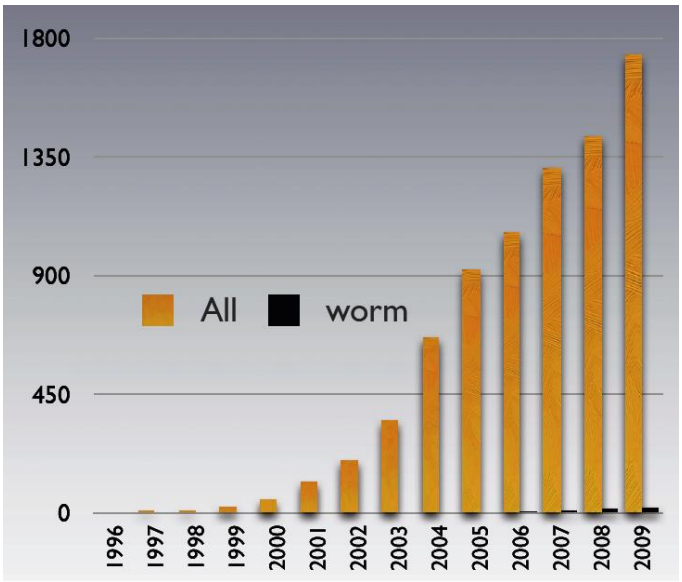

Figure 2.3: *Microfluidics publications from NCBI PubMed. Image taken from [51].*

2.2.1 Piezoresistive cantilever displacement clamp

The first measurement method used to characterize *C. elegans* body mechanics was pioneered by Park et al. [52]. This work developed a silicon piezoresistive cantilever-based force-displacement sensor in order to measure the mechanical properties of the worm (see Fig 2.4). By delivering force profiles through the cantilever tip on the worm cuticle, the nematode force-displacement curve and its stiffness could be obtained from the resistance changes in the piezoresistive material of the cantilever. The advantage of this system includes the ability to provide a wide range of force (10^{-8} to 10^{-3} N) and 100 μm displacements that are compatible with the properties of the biological samples with force resolution of 12nN. The system was also capable of measuring force without the need for an additional optical instrument. The indentation method provided by the cantilever limited the worm movement as the worm was constraint on an agar plate and partially immobilized on the head and tail section of its body. While this method does capture the peak magnitude of worm forces, it excludes the sensor from measuring the continuous force of moving *C. elegans.* The measurement was focused on passive worm stiffness rather than active muscle force. Because *C. elegans'* main behaviour is locomotion, it would be sensible to quantify the dynamic body forces of the nematode while the worm is moving naturally. The measurement system of this work was very complex as it required several different components (see Fig. 2.4). Apart from the piezoresistive cantilever, the system also used a piezoelectric actuator to move the cantilever and a FPGA controller. It also appears that the experiment is difficult to perform and that only a single force measurement point can be obtained during experiment. This limited the device capability of measuring multi-point forces for a worm sample.

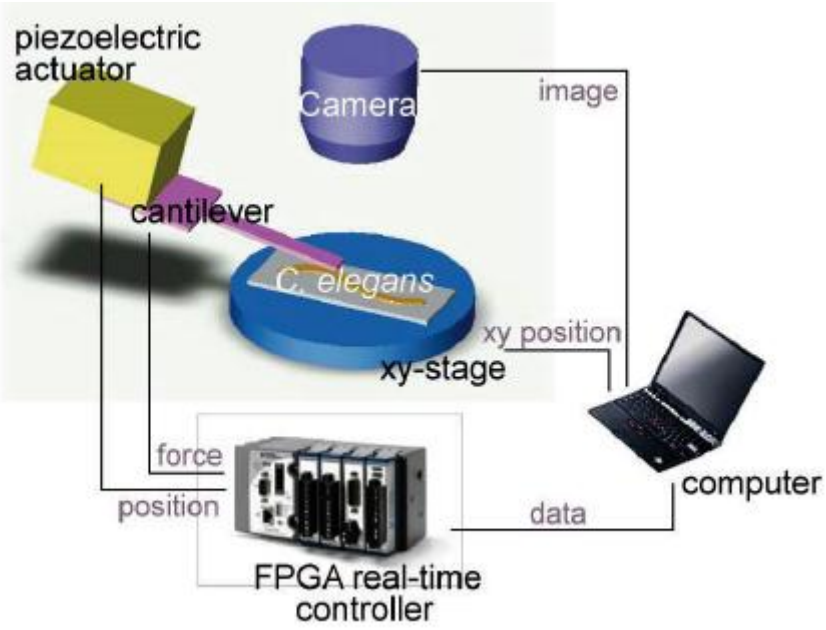

Figure 2.4: *Schematic of the force-displacement system using a piezoresistive cantilever-based sensor. Image adapted from [53].*

2.2.2 SU-8 force sensing pillar

In order to quantify the force of moving worms, the same research group [54] have demonstrated the use of microfabricated SU-8 pillar arrays to measure the *C. elegans* touch sensitivity during locomotion. The device consists of four fixed-guided cantilever arms with gold resistors acting as strain gauges, deployed on the bottom base of the pillar (see Fig 2.5).

The applied force from the worm at the pillar tip causes changes in the strain gauges resistance values and a Wheatstone bridge configuration was used to measure the displacement. The micro strain gauge force sensor was constructed from multiple layers of SU-8 and metal using quartz as the substrate material. The developed system was capable of measuring tactile sensitivity and interaction forces of *C. elegans* exerted during locomotion. The achieved force resolution was less than 1 μm and sampled at kHz rates, with forces recorded up to approximately 10 μN.

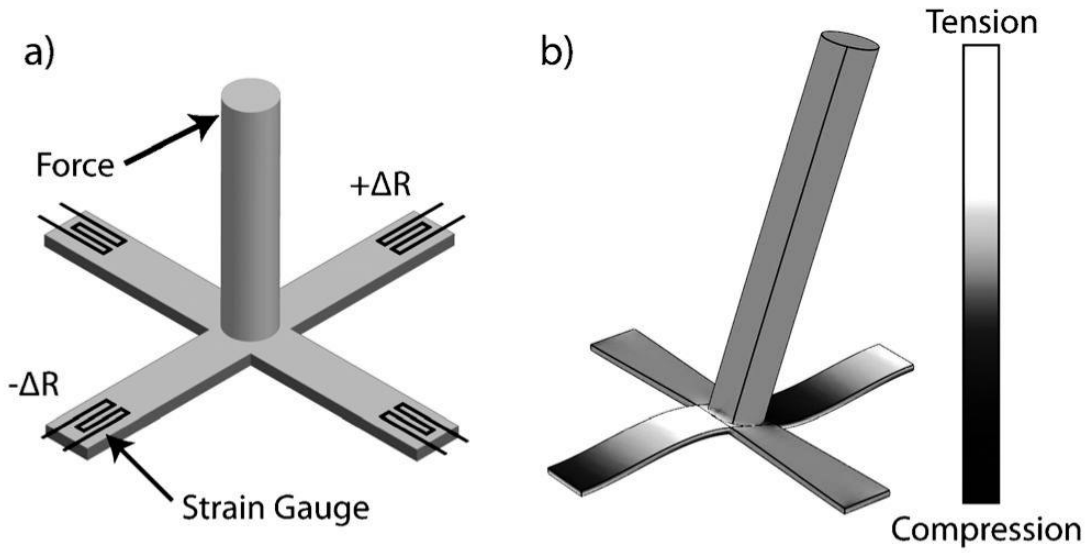

Figure 2.5: *SU-8 force sensing pillar with four strain gauges at the base of the cantilever used to measure worm forces from pillar tip deflection. Image adapted from [54].*

Despite the capability, the structure of the device was relatively complicated as it required complex procedures when fabricating the strain gauges. The pillars were formed from five layers of SU-8 resist which were deposited during the fabrication process. An additional step of attaching the device to a package by using glue followed by wire-bonding was also required. Because *C. elegans* is a temperature sensitive nematode [55], the heat dissipation from the gold resistors is anticipated to disturb the nature of the worm locomotion behaviour. This prevented the measurement of natural worm locomotion forces to be conducted.

2.2.3 Integrated fiber-optic microfluidic device

The most recent work was from Liu and co-workers [56] where an integrated fiber-optic microfluidic device with the capability to measure muscular forces of nematodes was developed. The device consists of sinusoidal wave microchannels with an opening at the lower part to accommodate for a silica single mode fiber (SMF) cantilever suspended horizontally in parallel with the channel (see Fig. 2.6). The worm force was calculated from the deflection of the SMF cantilever as the worm squeezed between multiple detection points (DPs) of the trench of the sinusoidal microchannels and the cantilever. The deflection caused by the worm reduces the

optical coupling from the SMF to a receiving multimode fiber (MMF) which was aligned and fixed in the channel with the SMF. An external photo-detector connected to the MMF was also attached within the device in order to receive the transmitted optical power caused by the SMF cantilever deflection. The device allow for multiple worm force data from a continuously moving *C. elegans* to be collected, which solved the problem of constraining worm movement and collecting single measurement point as reported by the first researcher in Section 2.2.1. This work was able to measure normal to translational motion forces of orders of tens of μN, with uncertainty of order of 1 μN. Deflections of the SMF were up to 20 μm with the resolution of ~ 1 μN were imaged at 10 Hz.

The inclusion of fibre-optics in their microfluidic devices has the advantage of providing high sensitivity force measurement, but the fabrication process of the device structure is highly complicated especially with the insertion of the fiber-optic materials. The measurement conducted in this work was also focused only on *O. dentatum* instead of *C. elegans*.

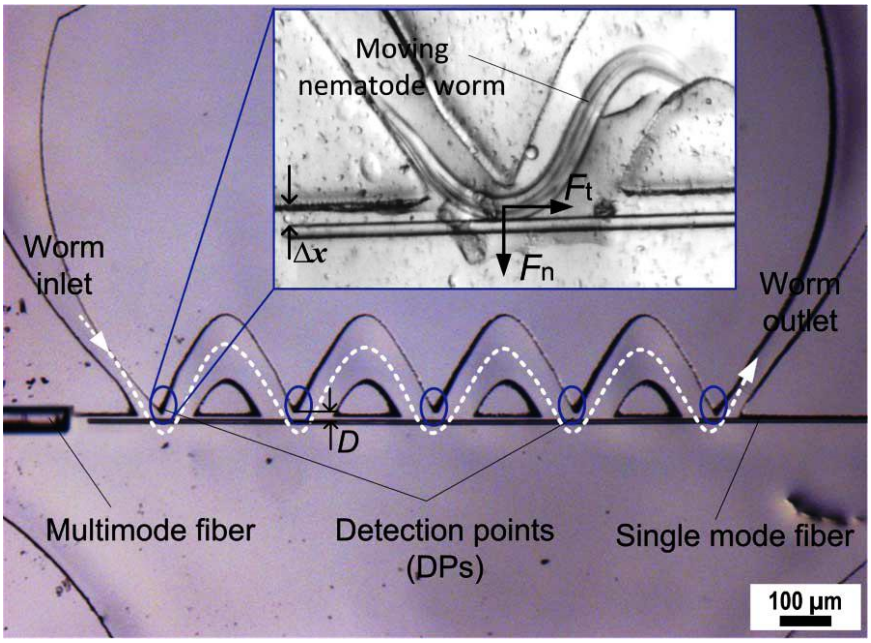

Figure 2.6: *Adapted image of fiber-optic microfluidic devices from [56] used to detect worm forces.*

2.3 This Thesis

Several motivations behind the study of *C. elegans* force measurement have been previously discussed. Although progress has been made towards the methods used to measure *C. elegans* locomotion forces, the development of *C. elegans* force measurement devices is just past its infancy, with only three microsystem devices specifically designed for the nematode having been reported. The current field of studying *C. elegans* locomotion forces is also missing some key components that will help accelerate the studies. Existing force measurements apparatus include a piezoresistive cantilever displacement clamp, an SU-8 force sensing pillar and an integrated fiber-optic microfluidic device. However, these existing devices have the following shortcomings:

(i) Relatively complex device structure which requires multiple SU-8 layers materials and complicated fabrication procedures [54].

(ii) Interference of the gold resistors material used in the device with the worm's movement where the heat dissipated from the resistors is likely to affect the worm's movement [54].

(iii) Unable to measure the dynamic force of *C. elegans* in motion as the worm is constrained on agar [52].

It is clear that the existing field lacks a micro-device that is both easy to fabricate and operate while at the same time has the capacity to provide high accuracy and resolution in force measurement. Therefore, this thesis aims to fill the current gap in the existing field by providing a simpler *C. elegans* force sensor that could overcome the drawbacks of the existing devices. The PhD research here will address these shortcomings by introducing a force sensor which is capable of continuously measuring the force of *C. elegans* in motion. The proposed system consists of a micropillar-based device made of PDMS only and a vision-based algorithm for resolving the force deflection of the cantilever-like pillars. The microdevice, sub-pixel resolution for visual tracking of the deflection, and experimental technique will form an integrated system for measuring dynamic forces of moving *C. elegans* with high resolution.

PDMS pillar structure has been widely adopted in other cellular force measurement applications than *C. elegans.* The structural deformations of the flexible thin substrate made of silicone or polyacrylamide can be visually tracked and subsequently transformed into forces [57].

Nevertheless, adopting this structure in *C. elegans* as a new application aims to offer researchers with enabling capabilities in *C. elegans* study. Firstly, the system is capable of instantly measuring *multi-point* forces rather than single-point forces for a worm sample. This can generate meaningful data to compare forces associated with different worm body muscles, gaining new understanding on how these muscles function.

While the applicability of the proposed method to measure worm forces is credible, the device is not solely limited to this task. Due to the transparency of the device, related locomotion parameters, such as the average locomotion velocity, body amplitude and the bending wavelength can be simultaneously quantified. Additionally, the device can also be incorporated with PDMS microvalves, which can simplify individual worm selection and manipulation for force measurement. Through automation of valve control, the system has the potential to enable high-throughput nematode force screening in the future.

2.4 Summary

As previously discussed, there is a need for a dedicated force sensor in order to quantify the worm contraction force during locomotion. The quantified worm force can provide useful information for the analysis of muscle disorders, human genetic and neurodegenerative diseases. It can also improve the understanding in the field of neuromechanics. Besides, *C. elegans* muscular forces can also help in the drug screening application of worms under different drug or chemical exposure. The quantified force value can also be used to validate the effects of genetic modification on *C. elegans* mutants. Due to the relatively small size of the nematode, constant progress in the microfabrication technologies has enabled microdevices to be developed to quantify worm forces. Nevertheless, the development of *C. elegans* force measurement devices is just past its infancy; only two works specifically designed for the nematode have been reported, while another device is designed for *O. dentatum*. Although the current devices accomplished the function of force measurement capabilities, all three existing devices reviewed require complex microfabrication procedures. The first device limits the worm from locomotion as the worm is constrained on a plate, while the inclusion of gold resistor as strain gauge and the single mode fiber optics cantilever in the other two devices requires highly complicated manufacturing process. In order to overcome these limitations, a simpler PDMS device consisting of vertical pillar arrays used for measuring force generated by moving *C. elegans* in real time is proposed in this thesis. Fabricated via soft lithography technique using only PDMS material, the current micropillar-based system is able to measure force with a resolution in the order of μNs for worm body widths of 100 μm. By using a vision-based algorithm to detect the pillar deflection, the incident force exerted by a worm can be resolved.

CHAPTER 3

Force Measurement Model

This chapter explains the development of the model used to quantify the force that *C. elegans* exerts on PDMS micropillars, based on experimental observation of the pillar deflection. The theoretical background behind the force equation and the equivalent force location from the force distributed along the pillar height is introduced. A sensitivity analysis of the equivalent point force measurement model is conducted in order to verify the calculated force from the measured deflection. Later, the details are presented on how the observed deflection is quantified experimentally through a custom image processing algorithm.

3.1 Introduction

The microfabricated device consists of several parallel rows of vertical cantilever-like micropillars supported by the channel base. Each pillar functions as an independent force-measuring unit dedicated to one individual *C. elegans*. According to the diameter of an adult *C. elegans*, the height of the pillars was set to 100 μm, to ensure that the worm moved inside the arrays of pillars rather than on the top of them. The diameter of the pillars was initially set to be 40 μm. However, owing to the limitation in the fabrication facilities, the diameter was increased to 60 μm.

To calculate the force imposed by *C. elegans* on the pillars, the relationship between pillar deflection and force has to be derived. Figure 3.1(a) and (b) show the schematic of *C. elegans* movement deflecting the micropillars and the scanning electron micrograph (SEM) of the micropillars respectively. Figure 3.2 shows an actual side view image of *C. elegans* inside the device.

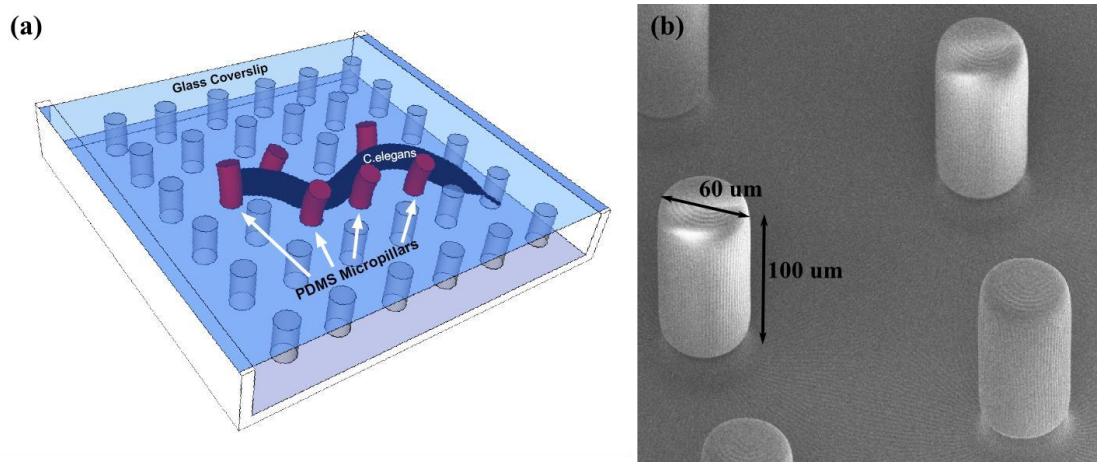

Figure 3.1: *(a) Schematic of C. elegans movement deflecting micropillars in the PDMS device. The device consists of an array of PDMS micropillars with each individual pillar regarded as a cantilever beam. The distance between the enclosed glass coverslip and the pillar tip is approximately 20 μm. (b) SEM micrograph of the pillars with the dimensions labeled.*

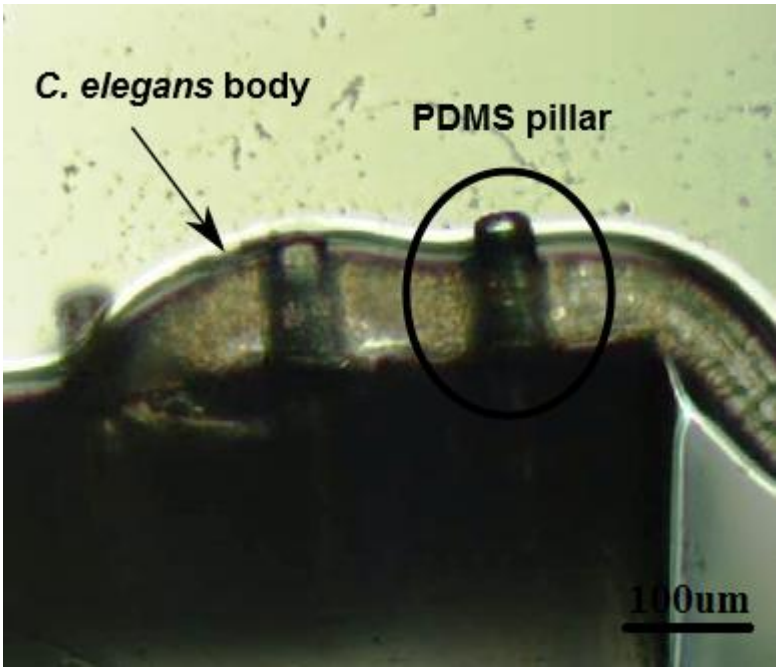

Figure 3.2: *A side-view optical micrograph of an actual* C. elegans *inside the device. The worm body diameter is approximately the size of the pillar height. Note, the glass coverslip was removed to facilitate imaging.*

Although the worm-pillar contact force is actually distributed over the contact area which causes local deformation in both the pillar and the worm, in this study the distributed force was represented by an equivalent point load on the pillar. This load results in an equivalent deflection of the pillar tip. In this sense, a force-deflection model would work, irrespective of a soft worm body. On account of the isotropic properties in the radial direction for the worm and pillar, the equivalent force is treated as a concentrated or focused point load at the pillar half height. This point is conceptually represented by a single contact point where two undeformed cylinders touch. This contact point corresponds to point *A* as shown in Fig. 3.3(a). The worm–pillar equivalent contact force is actually composed of two forces: the friction force, f_r, and the normal force, f_n, as shown in Fig. 3.3(b). The frictional force, f_r provides an equal force $f_{r'}$ crossing the pillar center plus a torque, *T*. The torque, *T*, does not produce deflection of the pillar, and so only $f_{r'}$ and f_n cause deflection. Therefore, the total equivalent force is *f*, corresponding to the total deflection of the pillar. It should be noted that drag forces applied to the pillar by the fluidic environment can be safely ignored. These were determined to be at a force magnitude of 10^{-13} N using a fluidic drag model [58]. Also, no measurable adhesion force was observed when worms disestablished contact with the pillar. Thus, adhesion was also safely neglected. Through an imaging system (a camera mounted on a microscope), the deflection Δ of the free end of the pillar is recorded and measured via a custom image-processing algorithm. Using the deflection available, the equivalent force f is subsequently obtained by a linear spring force-deflection model

$$f = k\Delta \tag{3.1.1}$$

where k is the stiffness of the pillar and Δ is the deflection. The stiffness is described below in section 3.5.

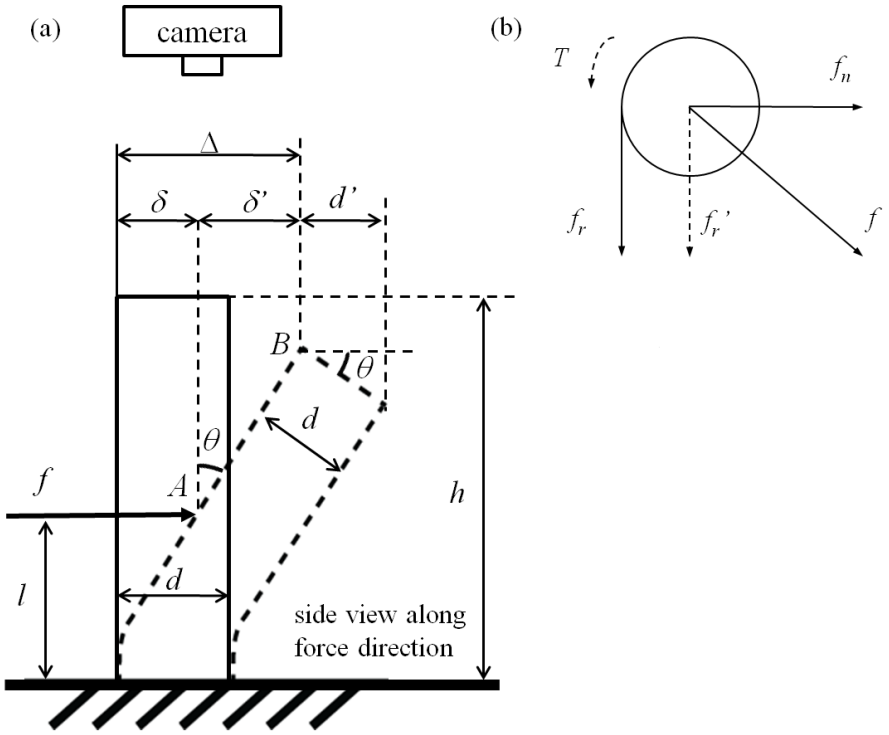

Figure 3.3: *Sketch visualizing equivalent force analysis (not to scale). (a) Schematic of the bending pillar for force analysis, where h is the height of the pillar, f is the force, l is the length from the load to the support, δ is the deflection at force point and Δ is the deflection at the free end of the pillar. (b)The worm-pillar contact force is a composite force f including normal force f_n and friction force f_r.*

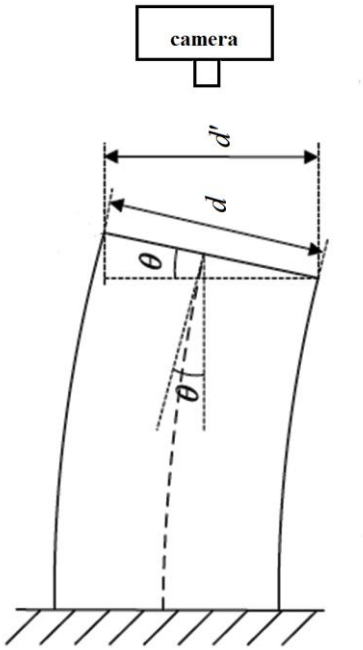

Figure 3.4: *Post deflection slope measurement, validating the small-deflection assumption of linear elasticity.*

3.2 Force-deflection Mechanics Model

As the worm moves inside the array of pillars, the equivalent force is applied at the contact point *A*, which does not correspond to the free end of the pillar. Thus the total deflection of the free end is attributed to two parts: (i) the deflection δ proportional to the equivalent load force at the force loading point *A*, and (ii) the linear displacement δ' of the free end, *B*, which is geometrically transmitted from point *A*. A valid application of linear elasticity requires small pillar deflections, which can be evaluated by the slope of the posts' free ends, θ (see Fig. 3.4):

$$\theta = \cos^{-1}\left(\frac{d'}{d}\right) \tag{3.2.1}$$

where *d* is the pillar diameter and *d'* is the projection of the deflected pillar measured from the recorded image sequence. The maximum value of θ is determined to be 17°, which satisfies $\sin\theta \approx \theta$; therefore validating the small-deflection assumption of linear elasticity [59]. The deflection is assumed to be purely horizontal because the small vertical force component and hydrostatic pressure exerted by the fluidic environment are at least three orders of magnitude lower than those required for the buckling of a vertical pillar [60]. Deflection of a cantilever beam is attributed to both bending and shear incurred by the equivalent force load. When the aspect ratio (i.e. height-to-diameter ratio) of a cantilever beam is greater than 5, deflection due to the shear can be safely ignored as it contributes less than 5% to the total deflection [61]. However, as the aspect ratio of the microfabricated pillar is 1.67 (i.e. 100:60), both bending and shear must be considered in the force-deflection mechanics model given by

$$\delta = \left(\frac{l^3}{3EI} + \frac{d^2(1+\gamma)l}{4EI}\right).f \tag{3.2.2}$$

where *f* is the equivalent force, *l* is the length from the load to the support, *I* is the area moment of inertia which is calculated for a pillar slice about the axis in the neutral surface perpendicular to the cylindrical axis, and *E* and γ are Young's

modulus and Poisson's ratio for PDMS, respectively. The first term and second term in Equation (3.2.2) correspond to pure bending and shear respectively. Pillar diameters are considered uniform along the height, which was verified by high-magnification SEM imaging (see Fig. 3.1(b)), thus *I* can be given by

$$I = \frac{\pi d^4}{64} \tag{3.2.3}$$

From the equivalent point of contact, *A*, to the pillar's free end, *B*, the load, the displacement will be linear because no other force exists. Therefore, this displacement can be derived based only on bending where *h* is the pillar height:

$$\delta' = \frac{l^2}{2EI}(h-l).f \tag{3.2.4}$$

The total free-end deflection of the pillar is a superposition of the two components in Equations (3.2.2) and (3.2.4):

$$\Delta = \delta + \delta' \tag{3.2.5}$$

$$\Delta = \left\{\left(\frac{l^3}{3EI} + \frac{d^2(1+\gamma)l}{4EI}\right) + \frac{l^2}{2EI}(h-l)\right\} f \tag{3.2.6}$$

Thus the equivalent force can be calculated as follows:

$$f = \frac{\Delta}{\left(\frac{l^3}{3EI} + \frac{d^2(1+\gamma)l}{4EI}\right) + \frac{l^2}{2EI}(h-l)} \tag{3.2.7}$$

Substituting *f* from Equation (3.1.1) into Equation (3.2.7) yields *k*, the stiffness of the pillar:

$$k = \left\{ \left(\frac{l^3}{3EI} + \frac{d^2(1+\gamma)l}{4EI} \right) + \frac{l^2}{2EI}(h-l) \right\}^{-1}. \quad (3.2.8)$$

To quantify *k*, the only unknown parameter is the Young's modulus, *E* of the PDMS, which will be calibrated and this is described below. The Poisson's ratio for PDMS is 0.5. It should be noted that Equation (3.1.1) implies that the direction of the load follows that of the deflection, permitting the continuous equivalent force of a moving worm to be resolved with both magnitude and direction.

3.3 Force-deflection Mechanics Model Analysis

In this thesis, the equivalent worm force was quantified based on the observed deflection of the PDMS pillars. Once the observed deflection of the pillar was measured, and the pillar geometrical and mechanical properties were obtained, Equation (3.2.7) can be used to calculate the magnitude of an equivalent point force that would result in the same deflection given it is applied at a position, *l*, on the pillar's axis. It was anticipated that this contact point would lie within $\pm$20% from the middle of the pillar height. In this study and in the following analysis, the location where this equivalent force acted was chosen to be at the pillar half height *h/2*, so that for a given deflection Δ, the equivalent force F_e was defined as:

$$F_e \equiv \frac{\Delta}{EI\left(\frac{5}{48}h^3 + \frac{1}{8}d^2(1+\gamma)h \right)}. \quad (3.3.1)$$

Since there was no information regarding the actual distribution of the worm's force on the pillar, and because the worm's location of contact area on the pillar could vary, choosing the half height at *h/2* provided a way of homogenizing the interpretation of the worm's force. It is strongly emphasized that F_e, which was the equivalent calculated force based on the force location acting at *h/2,* should not be taken out of context. A brief discussion is provided here that quantifies the error associated if the force F_e is taken out of context. For instance, as previously mentioned, the actual

worm-pillar contact force was not a point load, but instead was actually distributed over the contact area which caused the measured deflection on the pillar. The equivalent force F_e should not be confused with or interpreted as the integrated distributed load.

A uniformly distributed worm-pillar force per unit length, ω over the pillar length, *h* causes a deflection of

$$\delta = \frac{\omega . h^4}{8EI} \tag{3.3.2}$$

and a total free-end deflection of the pillar is shown in Equation (3.2.6). Since the deflection can be regarded as equivalent for both cases,

$$\frac{\omega . h^4}{8EI} = \left\{ \left(\frac{l^3}{3EI} + \frac{d^2(1+\gamma)l}{4EI} \right) + \frac{l^2}{2EI}(h-l) \right\} f \tag{3.3.3}$$

the contact point, *l* was found to be equal to 22, which is not in the middle of the pillar height of 100 μm. This indicates clearly that the calculated equivalent force F_e should not be interpreted as the equivalent of the distributed load acting uniformly over the pillar height.

That being said, it is important to note that the exact force distribution of the worm on the pillar cannot be known using this method. If the worm body is not distributed over the entire pillar height, the equivalent force is still the same, but the contact point varies according to the actual distribution of the worm's body on the pillar height. Although the calculated equivalent force F_e which is derived based on the pillar deflection at half pillar height *h/2* is adequate, it can represent a number of possible distributions. The actual equivalent worm-pillar contact point that results from the integrated force distributions and results in the same pillar deflection will obviously vary according to the distribution. In practice, the worm's body may not have been distributed across the entire pillar height for two different reasons: variations in the *C.*

elegans young adult body widths which are not exactly 100 μm in diameter; and the worm might not have touched the bottom of the device. This was caused occasionally by the 20 μm gap between the pillar tip and the glass coverslip as depicted in Fig. 3.5. Another obvious reason for a non-uniform force distribution is that the worms are cylindrical, so they do not contact uniformly across the body width. Given that the actual worm-pillar contact point force was unknown, and for the sake of uniformity to quantify the force exerted by the worm, the normalized/equivalent contact point was chosen to be at the middle of the pillar *h/2*.

Although the above explanation justifies the reason for using *h/2* for quantifying F_e, the discussion below shows how the misinterpretation of F_e could be dangerous. The sensitivity analysis that was conducted explains how much variation on the calculated point force *f* would be if the calculated point force were taken out of context, that is, when the location of the equivalent contact point from the irregular worm-pillar body distribution was not equal to *h/2*. This calculated point force was not the equivalent integrated force distributed on the pillar and it was also not acting at the point where the integrated load would have acted. The graph in Fig. 3.6(a) shows the force calculated for a given deflection of 5 μm with a varying worm-pillar contact point from 40 μm to 60 μm. As the contact point value increases, the calculated force decreases. When the force F_e is calculated based on the normalized contact point of *h/2* at 50 μm, and the possible actual point of contact is at 55 μm, there is a slight deviation of 1.74 μN in the force.

The % error is calculated based on the equation below

$$\%error = \frac{f - F_e}{F_e} x100\% \qquad (3.3.4)$$

where *f* equals the calculated point force when the contact point is not equal to *h/2*.
The plot in Fig. 3.6(b) shows that there is 20% to -40% variations in the calculated equivalent force for the contact point range of 40 to 60 μm. Given that it was not possible for the worm-pillar contact point to be at the pillar tip because of the glass coverslip, the contact point was likely to be from 40 to 60 μm as plotted in the graph.

In summary, given the nature of the variation in the actual positioning of the worm's body on the PDMS pillar and the difference between worm sizes, the calculated equivalent worm force F_e was chosen to act at the pillar midpoint which was *h/2*. This was done to provide a uniform method of analysis of the worm-pillar interaction. Errors could occur if F_e is taken out of context. The equivalent point force calculations *f* varies according to the reasonable estimation and is at least somewhat sensitive to the normalized worm-pillar contact point force, F_e.

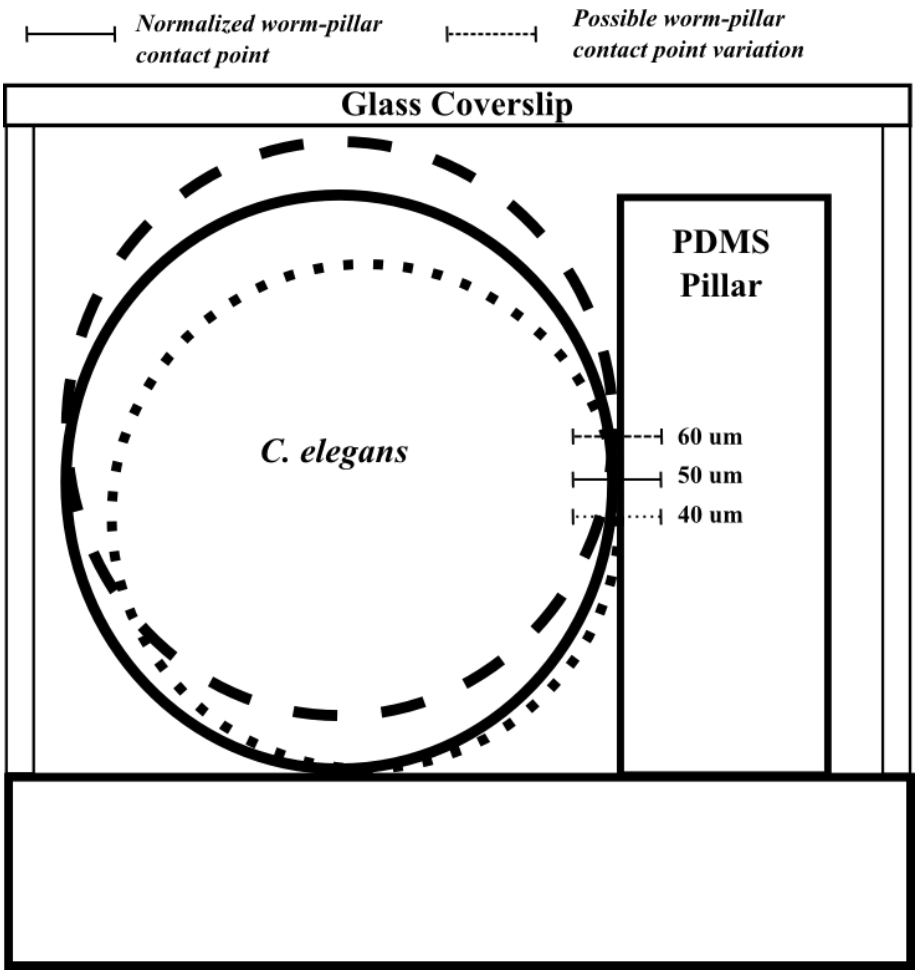

Figure 3.5: *A schematic showing the normalized equivalent worm-pillar contact point and the possible equivalent contact point from the variation in the distribution of the worm's body (dashed and dotted worm profile) on the pillar height.*

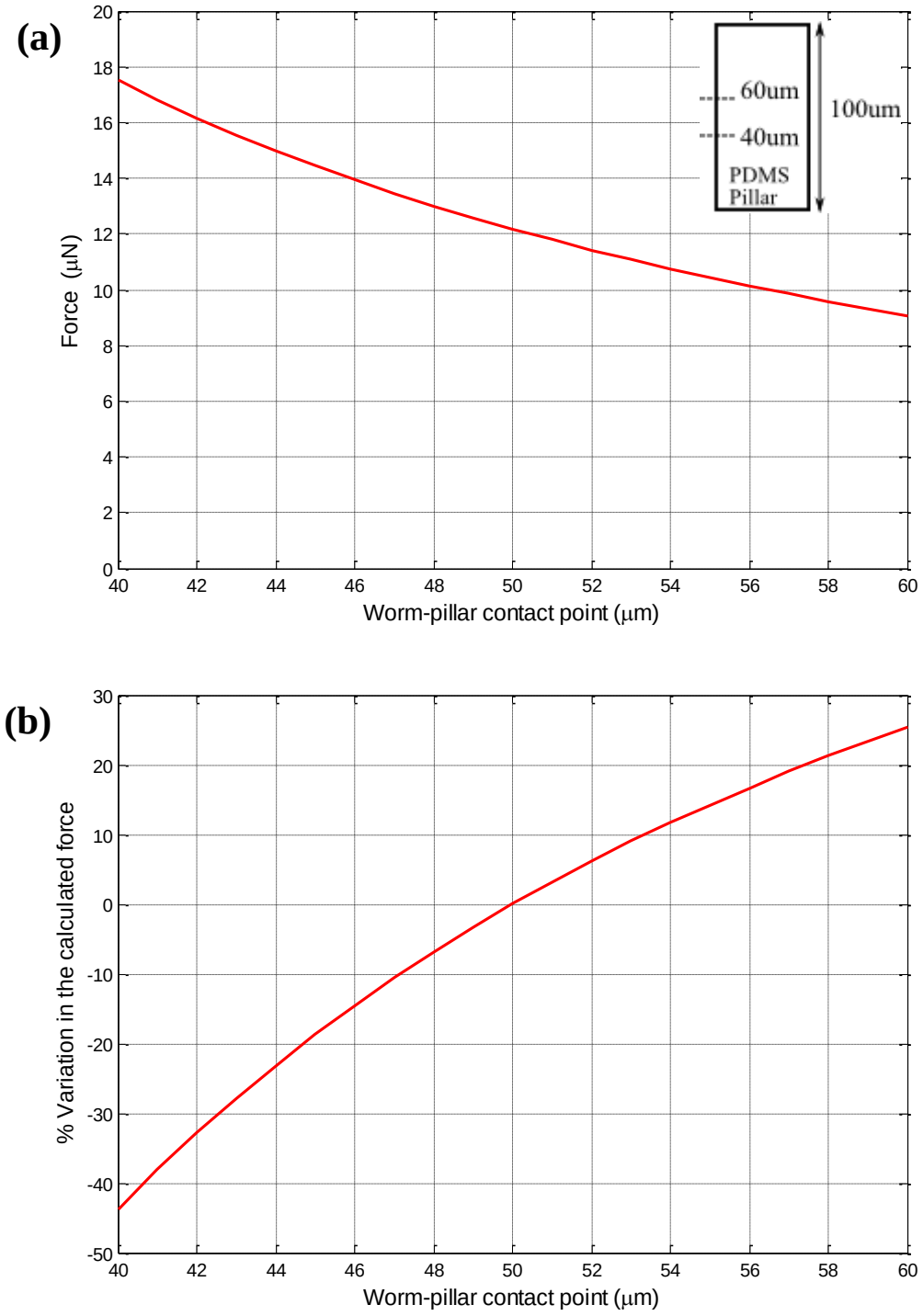

Figure 3.6: *(a) For a given 5μm deflection, the force is calculated based on the possible actual worm-pillar contact point which varies from 40 to 60 μm shown in inset.(b) Percentage variation in the calculated force with reference to the normalized contact point at 50 μm.*

3.4 PDMS Young's Modulus Calibration

To determine the Young's modulus value, a bulk PDMS cantilever beam produced under the same processing conditions was calibrated with a piezoresistive silicon force sensor (AE801, SensorOne, USA). This process was similar to that described by Liu et al. [62]. The method of using bulk PDMS was adopted in this thesis because it is inexpensive and readily available while providing reasonable accuracy. It has been demonstrated that Young's modulus showed a difference of 5% between bulk PDMS and a micro-PDMS structure, when both were constructed with the same microfabrication parameters [63], indicating a 5% error in force measurement with bulk PDMS.

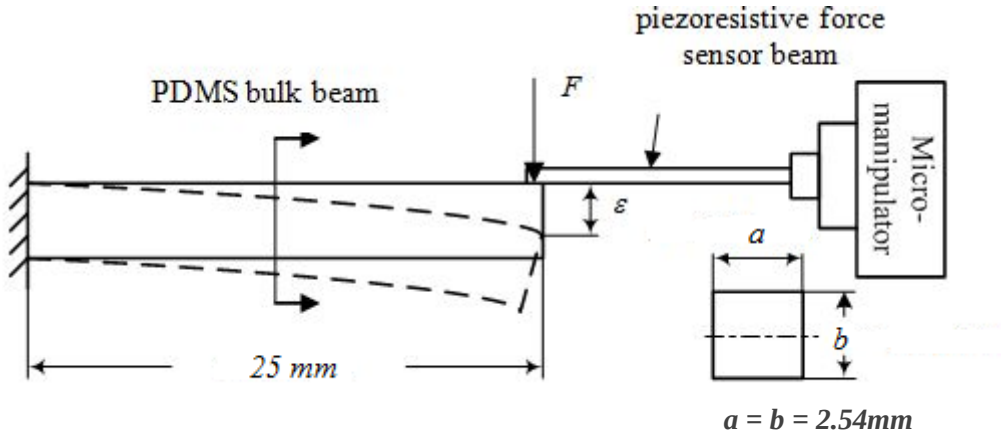

Figure 3.7: *PDMS Young's modulus calibration experiment setup [62].*

As shown in Fig. 3.7, the sensor was controlled to push the free end of the PDMS cantilever beam. In the calibration experiment, the contact area was carefully controlled so that the loads applied to the PDMS cantilever beam could be treated as concentrated forces. The stiffness of the silicon force sensor is 2 N mm^{-1}, from which deflections of the sensor beam were calculated. The deflection of the PDMS bulk cantilever beam was thus equivalent to the difference between the displacement of the micromanipulator (MP-285, Sutter, USA) and the deflection of the sensor beam. The calibration data points pairing the applied force F and free-end deflection ε of the bulk beam, shown in Fig. 3.7, were substituted into the following mechanics model describing pure-bending cantilever beams to calibrate the Young's modulus [59]:

$$\varepsilon = \frac{Fl^3}{3EI} \tag{3.4.1}$$

with area moment of inertia of the beam being

$$I = \frac{ab^3}{12} \tag{3.4.2}$$

where *a* and *b* are rectangular cross-section dimensions of the beam and *b* is the dimension in the plane of bending.

The PDMS device was prepared by mixing Sylgard 184 (Dow Corning) base:curing agent in a 10:1 w/w ratio. The pre-polymer was thoroughly mixed and degassed to remove any air bubbles. Then the polymer was poured onto the mold and degassed again to allow for bubble-free filling of the pillar holes. The mold was then placed on a hotplate and cured for 1 hr at 80°C. For a shorter baking time, a higher baking temperature can be used, but in this work, the baking temperature was fixed at 80°C. After cooling to room temperature, the replica was carefully peeled off and cured for a further 3 hrs at 80 °C to ensure that the pillars' structure was hardened and ready to be used. For calibration purposes, four sets of PDMS devices were prepared using the same method as described above. This was to ensure that the PDMS fabrication process used in this work was capable of producing consistent material properties. From each device, three pieces of PDMS were cut to the same size (namely Sample 1, Sample 2 and Sample 3) and tested using the sensor. Figure 3.8 shows the force vs. deflection curve for each sample where their Young's Modulus values were recorded and shown in Table 3.1. Even though there was a slight variation in the E values, the consistency in the values for each sample was sufficiently convincing. The Young's Modulus was determined to be 1.47 MPa, which is the average from the calibrated results. The results also indicate that the reproduction of the PDMS device for usage in this work did not affect its material properties as it had a consistent Young's Modulus value, hence demonstrating the PDMS device's reliability. Table 3.2 shows the Young's Modulus values measured in other research using different methods and different sample preparation procedures and the values were found to be between 0.36 to 2.2 MPa.

Table 3.1: *Young's Modulus values recorded from four different devices.*

Device / Sample	1	2	3	4
1	1.499 MPa	1.4849 MPa	1.397 MPa	1.6176 MPa
2	1.4995 MPa	1.7013 MPa	1.439 MPa	1.6245 MPa
3	1.6242 MPa	1.2069 MPa	1.4664 MPa	1.0527 MPa

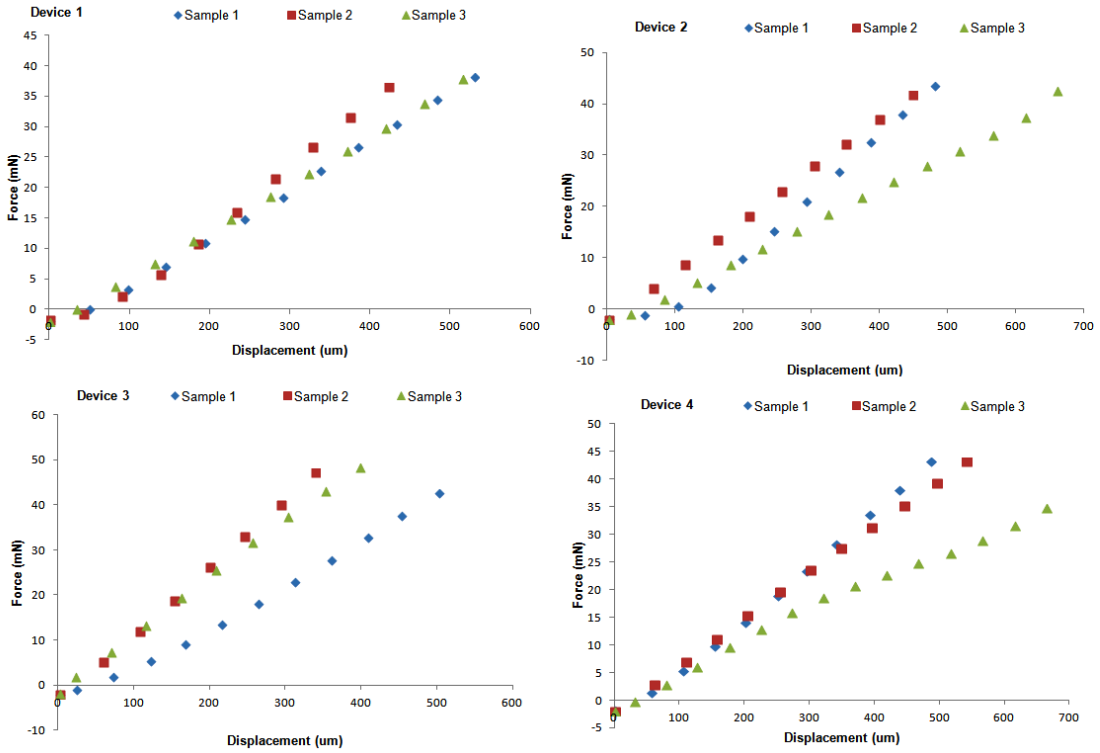

Figure 3.8: *Measured displacement as a function of force for four different devices prepared separately using the same exact method. The calibrated data points are then used to calculate the Young's Modulus values of each device.*

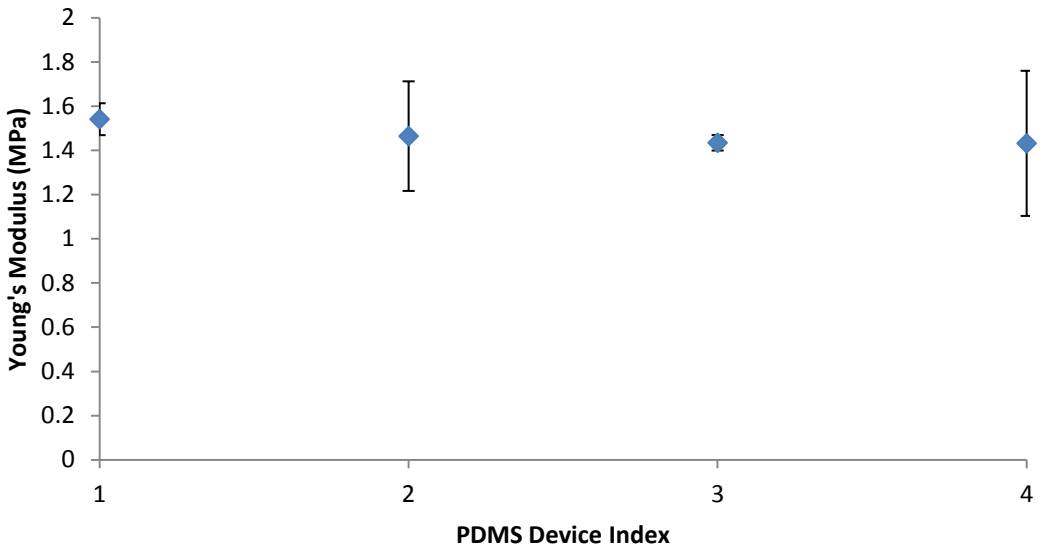

Figure 3.9: *Comparison of the Young's Modulus of each device. The average value corresponds to 1.47 MPa. The error bars represent the standard deviation of the measurements.*

Table 3.2: *PDMS Young's Modulus determined by various methods.*

PDMS Young's Modulus (MPa)	Measurement Technique	PDMS Sample Preparation
1.09	AFM [64]	24 hrs at 65°C
1.31	Material Testing Machine (Instron 5542) [65]	2 hrs at 85°C
1.45	Dynamic Mechanical Analysis (DMA) [66]	90 min at 65°C
0.36-0.87	Microscopic observation [67]	15 min at 90°C
2.2	Stretching tool (EMKA Technologies) [68]	2 hrs at 100°C
1.9-2.1	Compression measurement [69]	12 hrs at 65°C

3.5 Stiffness of the Pillars

As *C. elegans* has a nearly cylindrical body shape [52] apart from its tapered head and tail, it was also assumed that the worm applies forces to the pillar at its half height location. Thus, l in Equation (3.2.7) was taken as half of the worm width, indicating that the apparent stiffness of the pillar varies with the worm width. It is important to note that in this thesis; only adult wild-type *C. elegans* were used, which typically have the body diameter of 100 μm (equivalent to the pillar height). Thus, the assumption that the equivalent force is treated as a concentrated or focused point load at the pillar half height still applies. Normally, a worm has a relatively constant body width except at its tapered head and tail. The worm width was measured manually at the contact body part to compensate for these variations. Given the Poisson ratio (γ = 0.5) for PDMS [70], substituting the calibrated Young's modulus E, diameter (d) and height (h) of the pillar, and worm width ($2l$) into Equation (3.2.8) gives the quantitative stiffness, as shown in Table 3.3, for varying worm widths in a typical range.

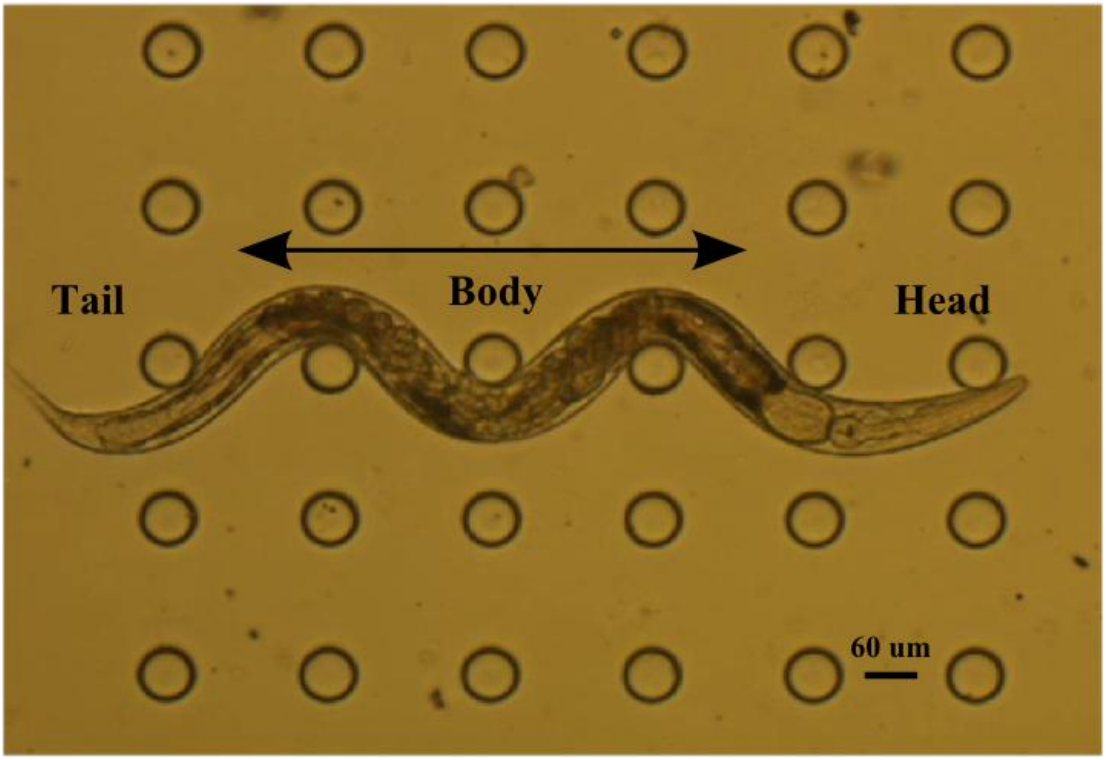

Figure 3.10: *Optical micrograph illustrating* C. elegans *cylindrical body shape with constant body width apart from its tapered head and tail.*

Table 3.3: *Stiffness of the pillars for varying worm widths.*

Parameters	Worm Width - $2L$ (μm)	Stiffness of Pillars (μN/μm^{-1})
γ = 0.5	10	114.01
E = 1.47 MPa	20	49.62
d = 60 μm	40	19.92
h = 100 μm	60	11.23
	80	7.38
	100	5.30

3.6 Force Resolution

For the imaging system (DS-5Mc, Nikon) with equal pixel size in both *x*- and *y*-directions, which is the case for this study, force resolution, ∂f, is given by the following expression:

$$\partial f = k.\mu.\sigma \tag{3.7.1}$$

where k is the stiffness of the pillar given by Equation (3.2.8), u is the pixel size in either direction, and σ is the visual tracking resolution for the pillar deflection, taken as the standard deviation obtained in the least-squares circle detection (LSCD) algorithm.

Visual tracking of the pillar centre was conducted with 33-45 image patches (depending on the video duration), with each image containing a certain number of pillars. The visual tracking resolution was found to be 0.5 ± 0.01 pixel from the standard deviation obtained in the least-squares circle detection (LSCD) algorithm. Detail regarding (LSCD) is explained later in Section 3.8. The pixel size was calibrated to be 1.18×1.18 μm. Using the stiffness of pillars in Table 3.3, the force resolutions for varying worm width were calculated and shown in Table 3.4. For a

typical *C. elegans* young adult with the body width of 100 μm, the force resolution is therefore 3.13 μN.

Table 3.4: *Force resolution for varying worm width or contact point.*

Parameters	Worm Width - $2L$ (μm)	Force Resolution (μN)
γ = 0.5	10	67.27
E = 1.47 MPa	20	29.28
d = 60 μm	40	11.75
h = 100 μm	60	6.63
u = 1.18 μm	80	4.35
σ = 0.5 pixel	100	3.13

Another important characteristic of the force model was the pillar diameter, which affects the moment of inertia, I in the force Equation (3.2.7). The moment of inertia varies proportionally with the diameter of the cylindrical pillar to the fourth power. In this sense, it was reasonable to use as small a diameter as possible in order to achieve higher force measurement sensitivity. The plot in Fig. 3.11 shows the calculated force resolution based on varying the diameter of the micropillar from 20 to 60 μm. Owing to limitations in the fabrication procedure, the micropillar diameter in this work was set to 60 μm which gives the force resolution of 3.13 μN. Details regarding this are explained in the next chapter.

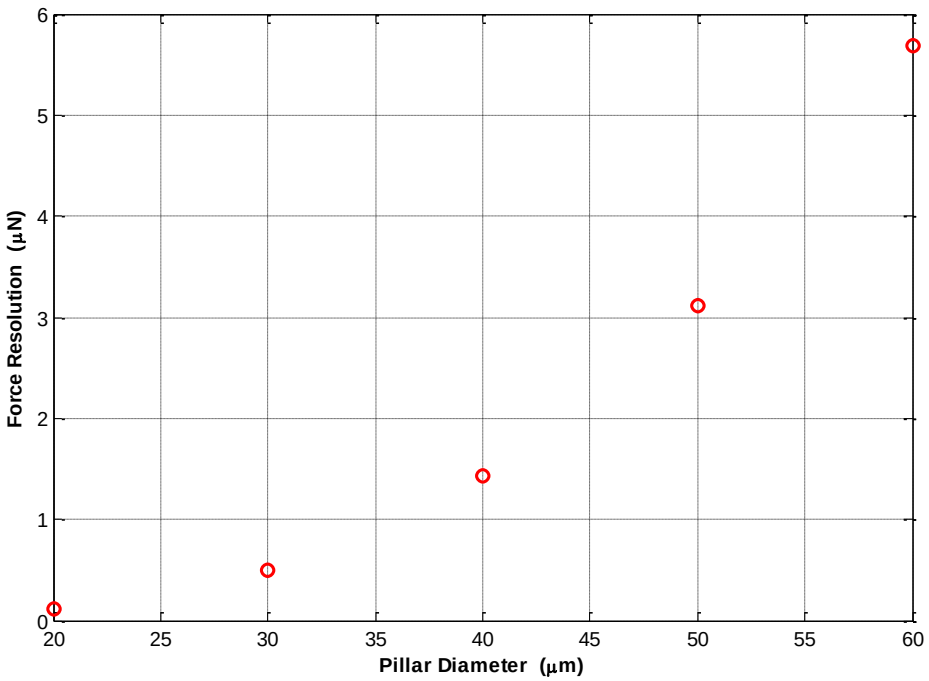

Figure 3.11: *Plot of calculated force resolution versus increasing pillar diameter.*

3.7 Force Measurement Error Discussion

The accuracy of the force measurement depends on the contact point for the point force equivalent to the actual force, the PDMS device material properties and the image resolution. Although it has been noted that the worm-pillar contact point was normalized and determined based on the worms' body width, minor variations in worm body width can result in a slight variation of the calculated force. The small deflection assumption error validating the linear elasticity can be quantified at less than 2% for θ equal to 17°. The reliability of the device material properties could also be improved by using a more precise calibration method for Young's modulus. Error associated with Young's modulus is 5% and the Young's modulus is assumed to be constant. The diameter of the pillars can also affect the force measurement resolution. For a 5 μm deflection, error in the pixel resolution is approximately 10%. Initially, the pillar diameter was set at 40 μm. However, owing to the limitation in the fabrication facilities, the diameter was increased to 60 μm. If a very high level of resolution or precision is desired, the resolution or precision of the system can be modified by

decreasing the stiffness of the pillar (e.g., using a higher aspect ratio for the pillar) and decreasing the pixel size (e.g., using a higher microscopic magnification factor).

3.8 Pillar Deflection Visual Tracking

An image processing algorithm was developed in-house to track the pillar deflection with sub-pixel accuracy. Figure 3.12(a) shows a worm moving inside a pillar array. As an example, four pillars in contact with a worm were chosen and labeled with different colors. For each pillar subject to deflection, the tracking is twofold: (i) to track the image patch containing the top circular surface of the pillar and (ii) to accurately detect the circular center position. The deflection is equivalent to the displacement of the circle center with respect to its neutral position where the load is zero, neglecting the small effects of pillar tilt and compression. In this study, similar to previous work by Liu et al. [62], a template-matching algorithm with a template update was used to track the motion of the deflecting pillars. Template matching is a technique used in image processing which compare an image template to the portion of the image being tracked. Initially, a square patch (i.e. initial template) containing the pillar top surface is acquired. This provides processing areas for the subsequent least-squares circle detection (LSCD) in order to determine the pillars' center positions. Template matching with constant template update permits the detection of very small changes in image patterns between successive frames of images; therefore, it is capable of robustly tracking the top surfaces of the deflecting pillars. Cumulative errors caused by updating the templates are eliminated in the subsequent detection of the circular centers using the LSCD algorithm. The image patch tracked by this template matching contains the deflecting pillar, whose circular surface or contour is used to detect the center position with LSCD. Original image is converted into grayscale image to avoid loss of image information. The grayscale image is then converted into black and white binary image. This method is called thresholding, where a tracked image patch, as shown in Fig. 3.12(b) is converted, which results in the binary image displayed in Fig. 3.12(c). The curved edge of the pillar top surface is then extracted for circle fitting. During curved edge extraction, only the half portion which was not in contact with the worm was selected for circle fitting as depicted in

Fig. 3.12(d), in order to minimize the error in the circle detection process. The other half was discarded as it was distorted because the view was blocked by a portion of the worm's body which can cause significant errors in circle fitting. When a number of consecutive frames had been selected for processing, the frames were initially converted to black and white in order to obtain binary images for subsequent extraction of the edge coordinates. Following this, four zones were defined to extract each pillar image in an assigned square window. The following algorithm was then applied to trace the outline of the outer circle of the deflected pillar:

(i) The square window is scanned from bottom left until a nonzero pixel belonging to the outer circle of the pillar from the top view is found. Pixel P_0 is a starting pixel of the circle tracing.

(ii) The tracing direction is defined

(iii) A 3×3 neighbourhood of the current pixel is searched in an anti-clockwise direction, beginning the neighbourhood search in the pixel positioned in the defined tracing direction. The first non-zero pixel found is the second circle point P_1.

(iv) The circle point trace is repeated up to detection of the n^{th} pixel P_n, where the algorithm stops.

A least-squares fitting algorithm was then used to fit the extracted curve edge points to a circle. The traced points were $(x_i, y_i), i = 0,1,2,.....,n-1$. The LSCD algorithm minimizes the sum of squares of algebraic distance from the *n* curve edge points to the circle center:

$$G(x_c, y_c, r) = \sum_{i=0}^{n-1}\left[(x_i - x_c)^2 + (y_i - y_c)^2 - r^2\right]^2 \quad (3.8.1)$$

Here, x_c and y_c are the coordinates of the circle center and *r* is the circle radius. First, define:

$$A = -2x_c \quad (3.8.2)$$

$$B = -2y_c \quad (3.8.3)$$

$$C = x_c^{\,2} + y_c^{\,2} + r^2 \quad (3.8.4)$$

Equation (3.8.1) can then be rewritten as

$$G(A,B,C)=\sum_{i=0}^{n-1}\left(x_i^{\,2}+y_i^{\,2}+Ax_i+By_i+C\right)^2 \tag{3.8.5}$$

Differentiating Equation (3.8.5) with respect to *A*, *B* and *C* yields a set of linear equation as follows:

$$\sum_{i=0}^{n-1}\left(x_i^{\,2}+y_i^{\,2}+Ax_i+By_i+C\right)x_i=0 \tag{3.8.6}$$

$$\sum_{i=0}^{n-1}\left(x_i^{\,2}+y_i^{\,2}+Ax_i+By_i+C\right)y_i=0 \tag{3.8.7}$$

$$\sum_{i=0}^{n-1}\left(x_i^{\,2}+y_i^{\,2}+Ax_i+By_i+C\right)_i=0 \tag{3.8.8}$$

By solving this equation set, the pillars' center coordinates and their radii were calculated. Figure 3.12 (e) shows the final fitted circle on top of the deflected pillars. The deflection of the pillar is therefore a directional vector pointing from its neutral (fixed) center to its updated center. To conclude, the image-processing algorithm follows five steps in order to measure the pillar deflection: 1) reading the image, 2) thresholding the image using binary conversion, 3) extracting the initial boundary location point for the selected pillar, 4) tracing the boundaries, and 5) fitting a circle to the boundary.

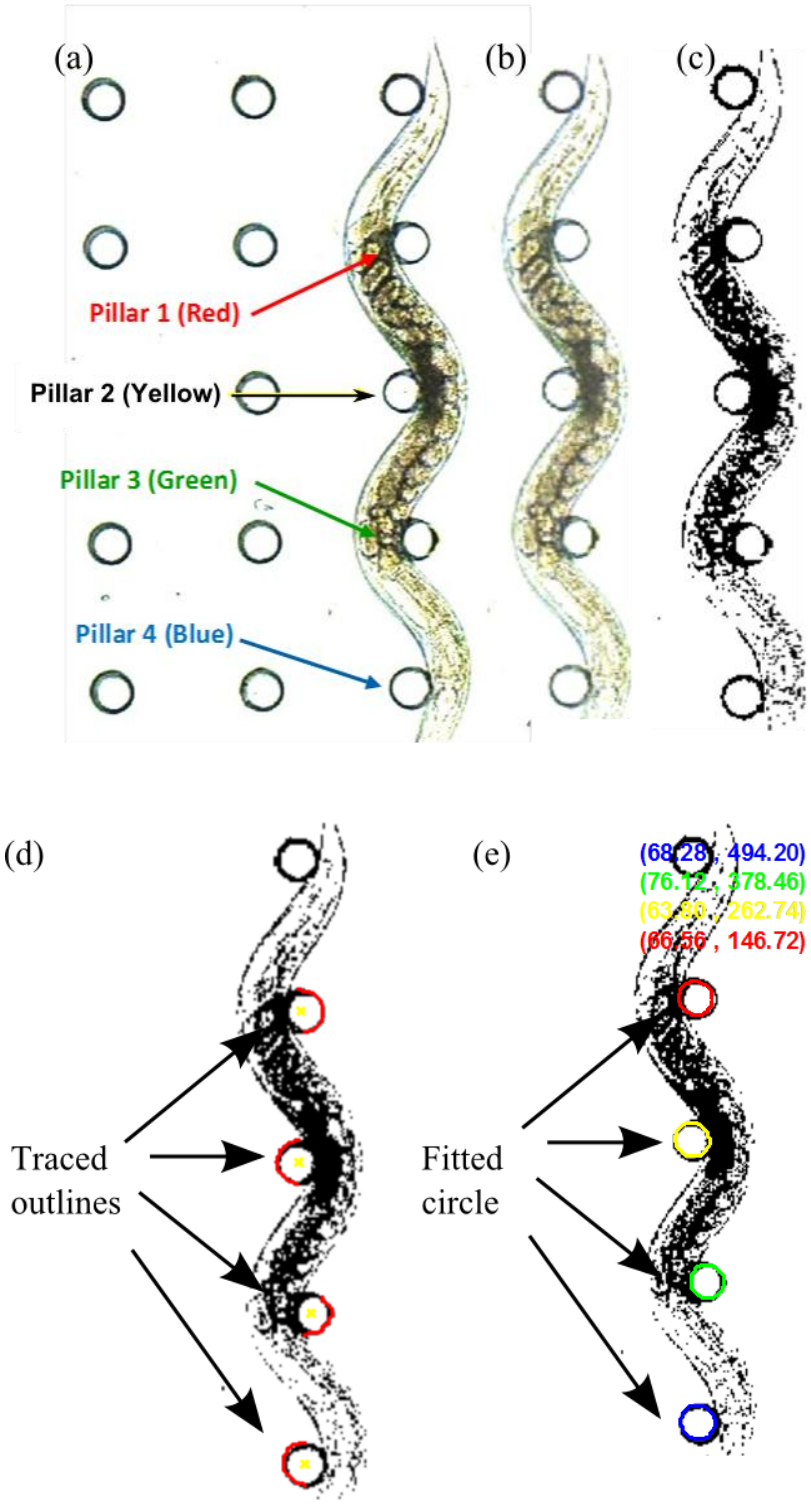

Figure 3.12: *(a) Worm moving inside the pillar array deflecting four different color-coded pillars. (b) Sub-pixel visual tracking result showing original image (c) Resulting image after conversion to binary. (d) The outmost portions along the deflection of the pillars used for circle fitting. The red drawing indicates the outline trace of the outer circle for each deflected pillar (e) Final fitted circles with each pillar center coordinate tracked and displayed at the top right corner for every single image frame.*

3.9 Summary

A method to estimate an equivalent point load to quantify the force exerted by the *C. elegans* on a PDMS pillar was developed by considering the distributed force as a concentrated contact point force. The contact point *h/2* was chosen and normalized to be at the middle of the pillar. The sensitivity of the system was analyzed by calculating the force *f* and the associated error based on the variation provided from the possible contact point with respect to the force F_e. This includes an investigation of the pillar stiffness and the force resolution based on varying the worm-pillar contact point. The calibration of the PDMS Young's Modulus is also explained and the Young's Modulus was determined to be 1.47 MPa. For a typical *C. elegans* young adult with a body diameter of 100 μm, the micropillar-based system is able to measure force with a resolution of 3.13 μN.

CHAPTER 4

Device Design and Fabrication

In this chapter, the design and fabrication procedures for the micropillar force-sensing PDMS device are described. The first section explains the features that must be considered when designing the device and the resulting design that was chosen to be used in this research. The fabrication process of the PDMS device is also explained in detail, along with the device casting procedures. The final section discusses the challenges and limitations faced in this research, in particular during the fabrication process.

4.1 PDMS Device Design

The nematodes *C. elegans* reside in a complex, three-dimensional soil environment and feed on bacteria. In the laboratory, these worms are typically cultured in agar-filled Petri dishes with a layer of *E. coli* in the middle as the source of food. The small size and continuously moving body of the worm make its manipulation very challenging. The motivation behind this work is to be able to study *C. elegans* locomotion forces using cantilever beam bending theory at the scale that is comparable to their natural habitat. In order to achieve this, a simple-to-reproduce device that enables simultaneous visual observation at micrometer resolution is essential. In addition, the device has to be safe for the nematodes in a way that it should not provide any chemical or toxic harm to the worms. Recently, new tools for studying and manipulating *C. elegans* using PDMS microfluidic devices have emerged, which have led to various experimental possibilities for extensive neurobiology and developmental research [26, 71]. The combination of microfluidic devices with *C. elegans* as a model organism is believed to be able to resolve the challenges that lie within the scope of neurobiology. In this study, PDMS is chosen

for the device because it has the following unique features that are compatible with the goal of this research:

(i) The microfabrication technique to reproduce the device is cheap and simple,
(ii) the microfluidic devices channel dimensions can be matched with the worm size,
(iii) device transparency enables continuous visual observation and is compatible with high-resolution optical imaging, and
(iv) the material properties of PDMS make it non-toxic, which is safe for the worm.

4.1.1 System considerations

The initial process of developing the PDMS device involved the choice of several key parameters regarding the geometry of the device as well as the specific arrangement of the micropillar layout. Because the worm moves in a sinusoidal wave shape, the device was initially envisioned to be a straight channel in which the worm would move in the middle of two parallel rows of vertical cantilever-like micropillars. The concept is that each pillar functions as an independent force-measuring unit dedicated to one individual *C. elegans*. The size of the nematode is a primary consideration of the design of the PDMS channel and the force-sensing micropillars. The pillar must have sufficient height to match the worm's body, while the pillar diameter must allow for deflection in order to conduct very sensitive force measurement. Since the typical diameter of an adult *C. elegans* body width is approximately 100 μm, the pillar height was set to this value. Simultaneously, the pillar diameter needs to be sufficiently small as to allow it to deflect far enough for the optical read-out system to resolve the movement. However, due to fabrication constraints relating to the pillar aspect-ratio discussed later in this chapter, 60 μm pillar diameter was used.

In addition to the general geometric considerations are constraints related to the worm's need for a moisture rich environment [6]. To resolve this issue, the device was filled with de-ionized (DI) water for the worm locomotion. It has previously been observed that filling the channel completely with fluid resulted in worms moving by

swimming motion [37].Though this is not an issue, the initial focus of this work was to study the nematode conventional crawling motion as observed in their natural habitat.

In order to keep the high moisture environment while simultaneously avoiding the swimming motion, the amount of water was carefully controlled in order to produce a very thin layer of liquid in the array. Since the idea is to coat the surface of the apparatus with thin layer of water, care must be made regarding the natural hydrophobicity of the PDMS material. This presents an issue because it can inhibit the desired thin fluid layer from forming. In order to render the PDMS surface more hydrophilic, the PDMS device surface was treated using atmospheric plasma.

The next sections detail the geometric development of the experimental apparatus. There were two preliminary designs that helped identify critical flaws in the system, namely Design 1 and Design 2. The final design (Design 3) was obtained by solving the challenges encountered during the first two preliminary designs.

4.1.2 Preliminary design and findings

The development of the PDMS force measurement device involved several iterations in order to identify and remove certain features that inhibited the experiment. This section details the development and findings of each new device design. For all three designs, the PDMS device surface has to be treated using a corona treater (Electro-Technic Products) in order to ensure that the device is hydrophilic. Then, to mimic the nematode natural habitat, the device has to be filled with water to provide a moisturized environment for the worm's locomotion. The amount of water has to be carefully controlled in order to produce a very thin layer of liquid with a negligible thickness relative to the worms' body width throughout the chamber. When loading the worm into the channel, it is imperative to ensure that the worm's body fits comfortably inside the PDMS channel. It was anticipated that the straight channel design would allow for the worm's sinusoidal movement pattern throughout the experiment and that the worm's body position had to be in between the pillars in order to allow for force measurement to be conducted.

4.1.2.1 Design 1

In the initial device, the pillars were set within the channel so that the pillars were arranged in two parallel rows close to the channel wall (see Fig. 4.1). A spacing of 20 μm between the channel wall and the pillar edge was chosen to allow the pillars to deflect sufficiently. In this first preliminary design, three different spacings were attempted. Three channels widths were used: (1) 270 μm, (2) 300 μm, and (3) 320 μm, with the cross-channel distance between the pillar rows set to: (1) 150 μm, (2) 180 μm, and (3) 200 μm. Figure 4.1 depicts this design in which the channel width is 270 μm and the pillars are set 150 μm apart. For all arrangements of Design 1, the pillar-to-pillar distance was set to 20 μm. This was done in an attempt to ensure that the worm would only move in between the parallel rows and at the same time avoiding the worm from squeezing in between two adjacent pillars. As indicated in Fig. 4.1(b), this was not successful.

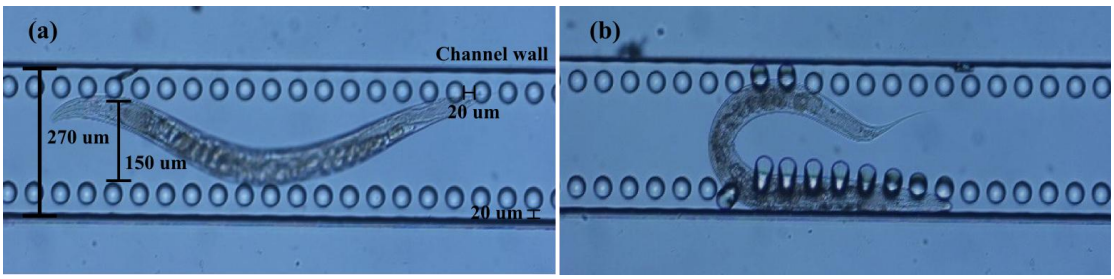

Figure 4.1: *PDMS device Design 1 for* C. elegans *force measurement consists of two parallel rows of micropillars. (a) Minimum contact between the worm body and the pillars resulted in negligible pillar deflection and (b) worm squeezing their body between the channel wall and the pillars edge.*

Once the worm was loaded into the channel, it was found that the worm's body width fitted comfortably inside the PDMS channel. One limitation of this design is the lack of pillar deflection from the worm movement (see Fig. 4.1(a)). When the worms moved in between the two parallel pillar rows, they were observed to display crawling behaviour but there was very little contact between the worm body and the pillars, resulting in negligible deflection of the pillars. Thus, this design was not successful as it was very difficult to collect any experimental data on the worm's locomotion forces.

Furthermore, while it was predicted that the straight channel design would allow for the worm's sinusoidal movement pattern throughout the experiment, to our surprise, the worm managed to squeeze their body to the channel wall and also in between the adjacent pillars. As shown in Fig. 4.1(b), the worms were observed to squeeze themselves in the small gap between the pillar edge and the channel wall. Even though the pillars were deflected during the squeezing condition, this was not the ideal condition for force measurement as the focus was on *C. elegans* natural locomotion forces, which consists of sinusoidal movement pattern. It can be hypothesized that the squeezing to the channel wall mimics their burrowing behaviour when they are in the soil/Petri dishes.

4.1.2.2 Design 2

In order to resolve the issues encountered in Design 1, the number of micropillar rows was increased and the spacing between the pillar center-to-center distances was also increased. The second design, as depicted in Fig. 4.2, consists of four pillar arrays set within a channel. In this design, two sets of pillars arrangement were used where the inter-pillar distances were set to 60 μm and 70 μm in the x- direction while the distances in y- direction were set to 110 μm and 120 μm respectively.

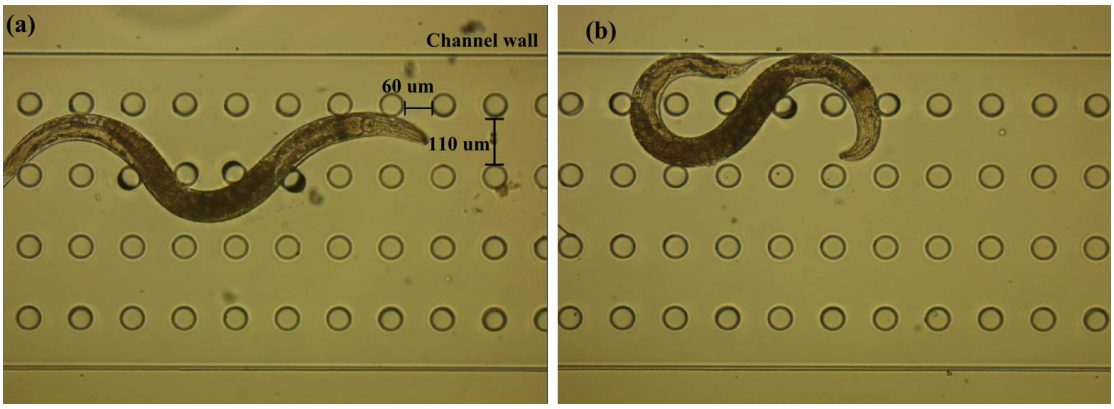

Figure 4.2: *(a) Optical micrograph of a worm inside a four row micropillar array with increased spacing between adjacent pillars where (b) the worm prefers to squeeze their body to the channel wall.*

In this design, different locomotion patterns were observed where the nematodes use the pillar as guidance during propulsion to move in between the pillars and the resulting pillar deflections were measurable. However, even though the number of the

pillars in the arrays was increased, a critical flaw in the design remained: there was still tendency for worms to squeeze their body against the channel wall (Fig. 4.2).

4.1.2.3 Design 3

This unanticipated behaviour of the worm in the previous device designs led to the third design. In order to avoid the constant contact between the worm and the channel wall, a 9 x 9 mm square chamber was fabricated with multiple arrays of PDMS pillars arranged in a lattice and honeycomb structure, as shown in Fig. 4.3. For both pillar configurations, there are four different spacing used between the pillar center-to-centers: 110 μm, 120 μm, 130 μm and 140 μm. From this design, the worms were observed to move in between the micropillars with measurable pillar deflections and the contact between the nematode and the chamber wall was minimized.

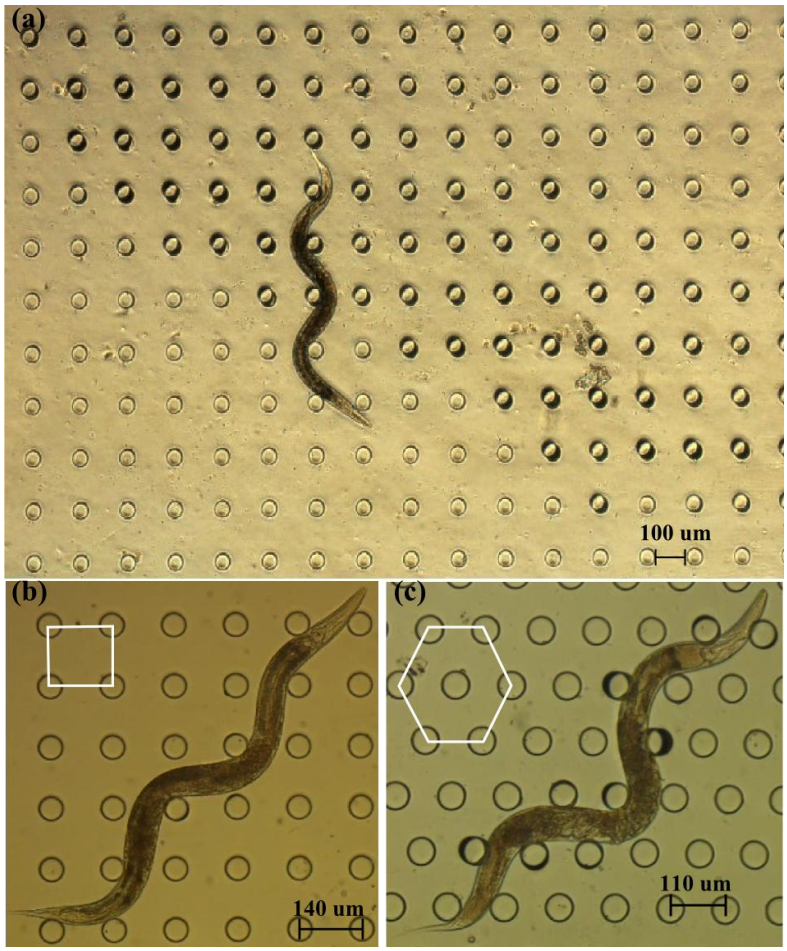

Figure 4.3: *Optical micrograph of Design 3 (a) Square chamber filled with a matrix of PDMS micropillars. Two different layout were used (b)'lattice' design where the distance between x- and y- direction is equal (c) 'honeycomb' design, incorporating an inter-row pillar offset to obtain hexagonal structure.*

4.2 Fabrication of the Device

The experimental work of this research was carried out using microfabrication facilities available at the Department of Electrical and Computer Engineering Nanofabrication laboratory. The PDMS devices in this work were prepared using soft-lithography, a technique which typically is able to produce three-dimensional and curved structures based on replica-molding [72]. In soft-lithography, an elastomeric stamp with patterned structures on its surface can be used to produce structures with sizes ranging from 30 nm to a few hundred microns.

The fabrication process involves a multiple-step sequence of photolithographic and chemical processing during which microscopic structures are gradually created on a wafer made of semiconducting material. Following master fabrication, the microfluidic system is created using soft-lithography. In this process an elastomeric device is generated containing micropatterns and microstructures. The following describes in detail the fabrication processes involved in fabricating the PDMS devices used in *C. elegans* locomotion force measurement.

4.2.1 SU-8 negative resist

In microfabrication technology, photolithography is the process used to transfer a certain pattern using light from a photomask (in this work it is the chrome coated glass mask substrate) to a light-sensitive material/chemical which is often referred to as photoresist. When exposed to radiation (UV light), the resist materials will be modified according to the resist category. There are two types of photoresist, namely positive resist and negative resist. In the case of positive photoresist, the pattern area which is exposed to light will be dissolved by the photoresist developer, while in the case of negative photoresist, the regions hit by light will remain after the development while the unexposed region will dissolve in the developer. SU-8 photoresist consists of three basic components: 1) epoxy resin, 2) photoinitiator, and 3) a solvent.

In soft-lithography, a reusable mold is fabricated using photolithography and for reliable reproduction of uniform features, this mold should be mechanically strong and thermally stable. In this work, SU-8 2000 (MicroChem, Newton, MA) was used as mold material because it is an epoxy-based negative photoresist and thus forms a

highly cross-linked structural layer through UV patterning. Moreover, due to its optical transparency and mechanically stable features, SU-8 enables the fabrication of thick molds (up to several hundred micrometers) and makes it possible to produce multilevel molds by repeating the lithography steps on the same molds [73, 74]. The photoresist is also capable of producing very high aspect-ratio structures and has excellent imaging characteristics. In order to accommodate different thicknesses (see Fig. 4.4) for the *C. elegans* force measurement device, two types of SU-8 are used, namely SU-8 2025 and SU-8 2100. The SU-8 2025 is utilized to produce a thinner structure of less than ~30 μm, while SU-8 2100 is capable of producing thicker features up to a few hundred microns. However, in terms of coating, SU-8 2100 is more challenging to deal with as it has very high viscosity compared to SU-8 2025, as shown in Table 4.1.

Table 4.1: *SU-8 photoresist viscosity [75].*

Photoresist	%Solids	Viscosity(cSt)	Density (g/ml)
SU-8 2025	68.55	4500	1.219
SU-8 2100	75.00	45000	1.237

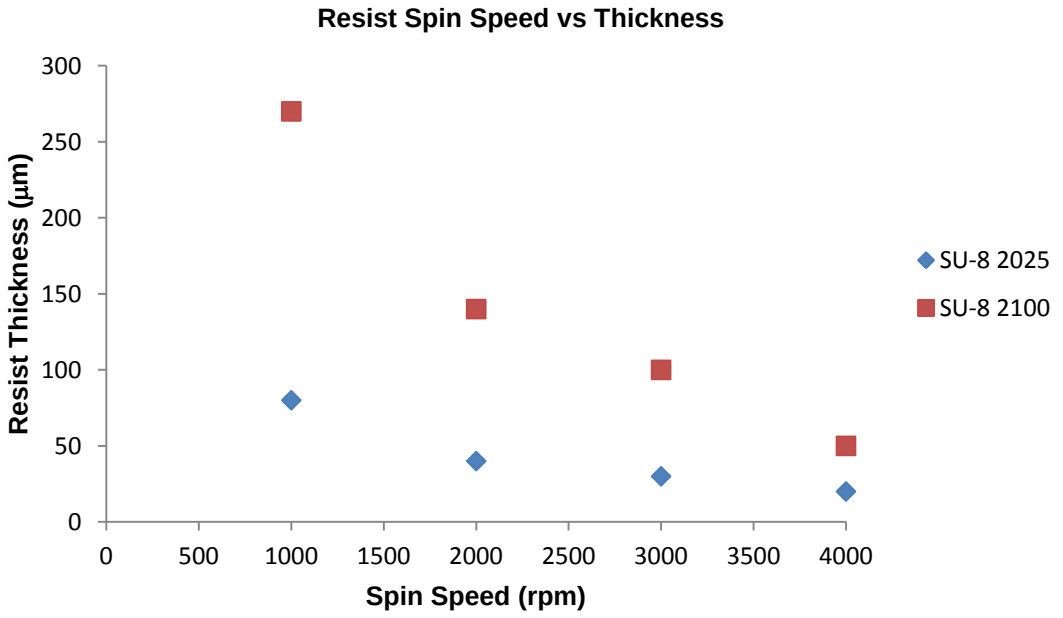

Figure 4.4: *Graph of resist thickness versus spin coater speed [77].*

4.2.2 Mask design

In order to transfer the design concept into reality, the first step of the fabrication is to prepare the visualized design using L-Edit software (Tanner Tools, USA). This is a layout editor mainly used for electronic circuit design, printed circuit board and other computer-aided design work. The design files in this work were prepared in a drawing interchange format (DXF) and were then transferred to a mask writer (Heidelberg μPG 101), which is a microlaser pattern generator used in photomask direct writing. In photolithography, a photomask generally consists of opaque chromium patterns set on a transparent glass plate. The mask writer was used to expose the designed pattern of the *C. elegans* force measurement device onto a chrome glass mask substrate. In this research, four-inch (approximately 100mm) length dark field soda lime glass mask substrates covered with a chrome layer were used (Nanofilm). Since chrome is not transparent to UV light, the dark field area was used to block the UV light while the clear field region allowed the UV light to pass through and cross-link the negative resist underneath.

Once the design had been fully transferred to the mask substrate using the mask writer, the mask had to undergo several further process steps. First, the mask was developed in AZ MIF326 developer for 60 s. This was done to remove unprotected parts of the mask design so that the device design was left visible on the mask. Following this, de-ionized (DI) water was used to rinse the substrate and a nitrogen gun was used to blow-dry it. The chrome layer was then etched away using chrome etchant for 1 minute and the mask substrate was rinsed thoroughly again. The remaining resist was stripped using acetone and then rinsed with isopropyl alcohol (IPA). Finally, the mask was dried using nitrogen, after which it was ready to be used for patterning of the mold in the later stages of production.

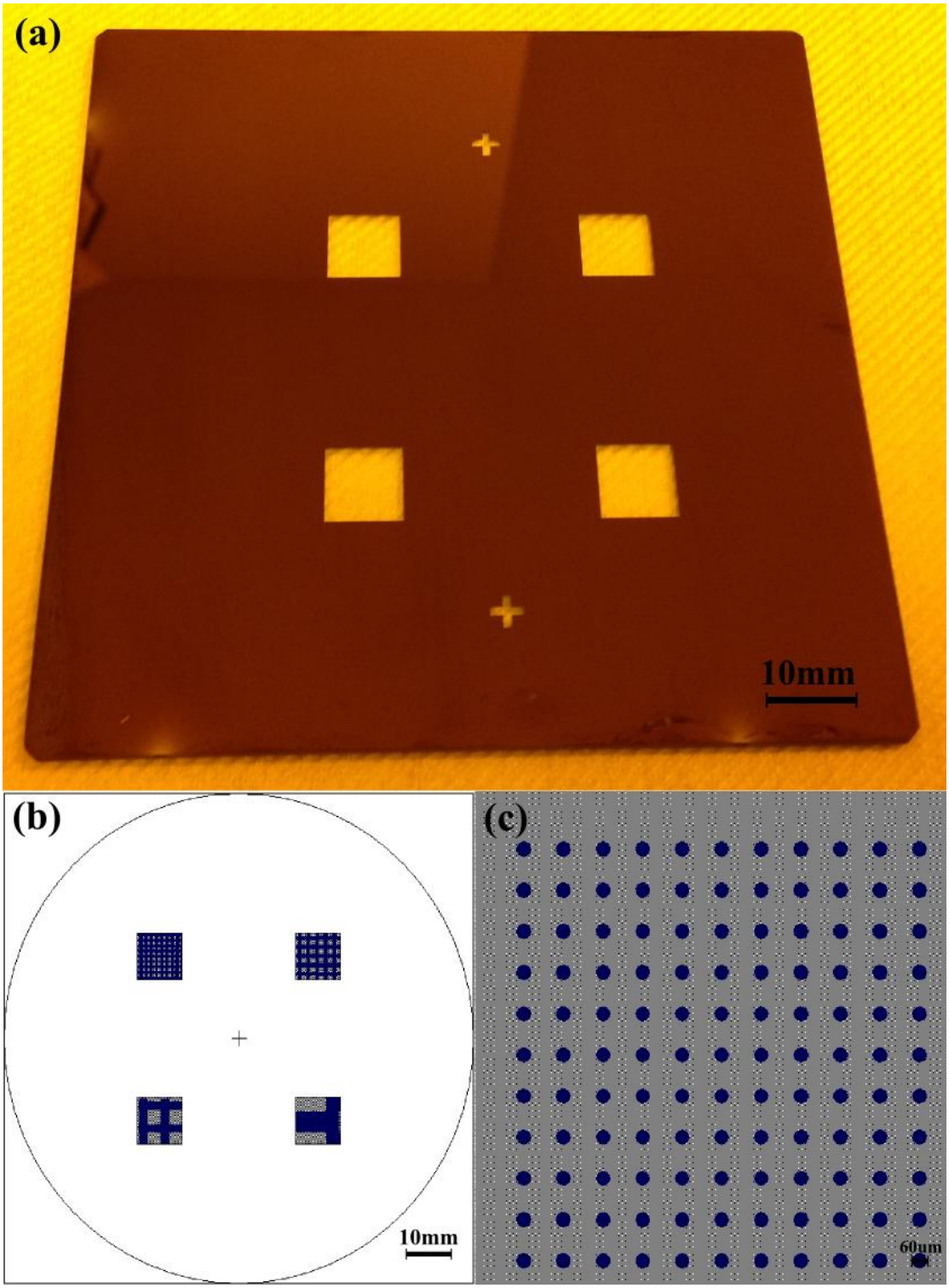

Figure 4.5: *(a) Photograph of chrome mask with the design pattern (b) Schematic of mask design prepared using L-edit software consisting of four chambers filled with micropillar arrays (c) Close-up of the micropillar arrays design as holes structures in the square chamber.*

4.2.3 Substrate preparation

The fabrication of the *C. elegans* force measurement devices required several important steps. The following section will explain in detail the fabrication process of the devices. Figure 4.6 shows the illustration of the fabrication procedures as well as the PDMS device casting method. The complete fabrication process is summarized in Table 4.2.

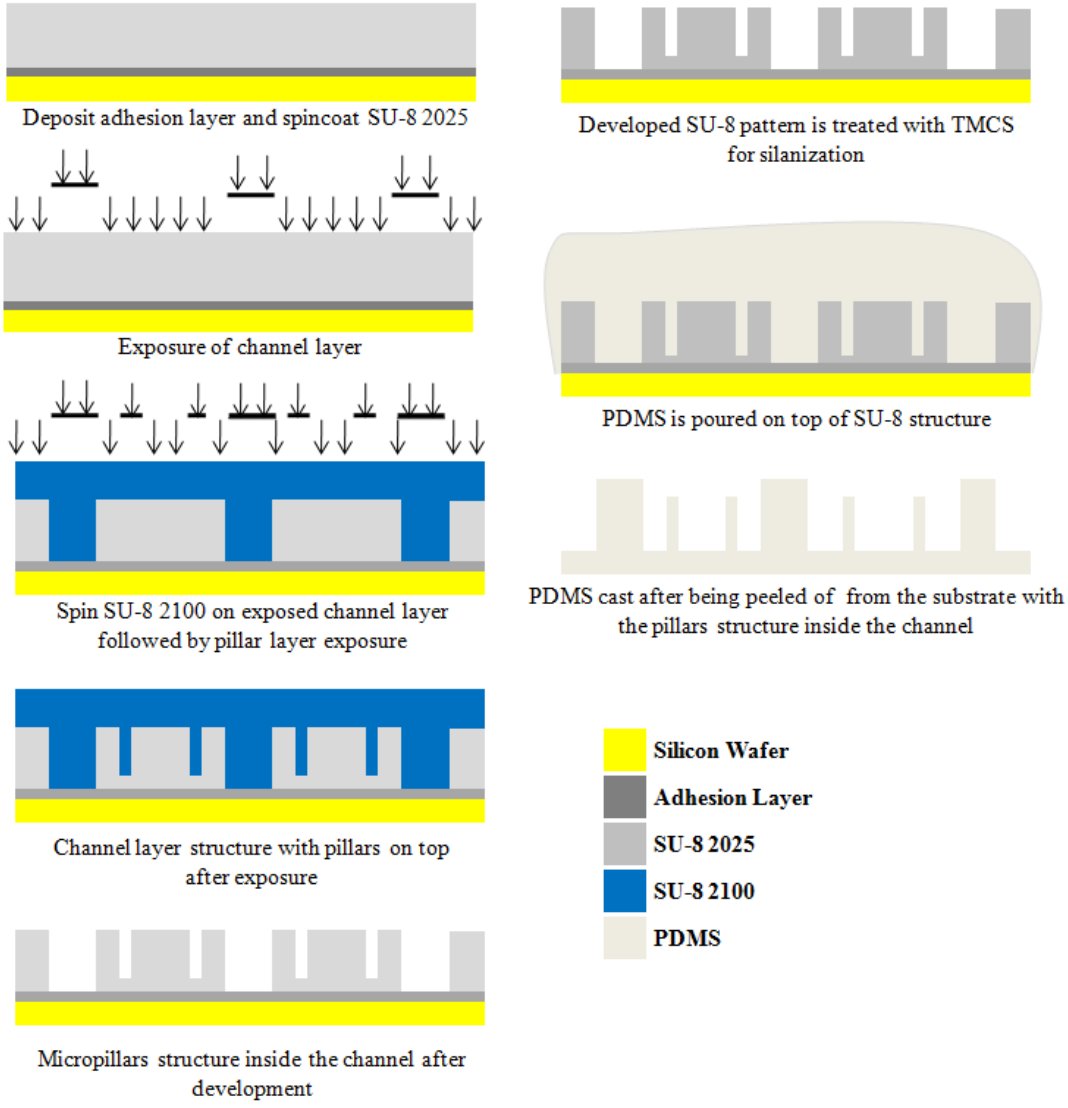

Figure 4.6: *Schematic of the final device fabrication process illustrating the complete fabrication procedure for the* C. elegans *PDMS force measuring device along with the PDMS casting method.*

4.2.3.1 Substrate cleaning

In order to create the mold which was to be used as the *C. elegans* force measurement device, four-inch diameter silicon wafers were used as the substrate. Initially, the substrates were cleaned in order to provide good adhesion between the substrate material and SU-8 photoresist. For optimum adhesion, different cleaning steps are recommended prior to the deposition of the photoresist [77]. One approach is to clean the substrate using piranha wet etch/diluted acid bath followed by a DI water rinse, or using reactive ion etching (RIE) for oxygen plasma removal of organics from the surface. However, since the adhesion of SU-8 depends highly on surface dryness, it was decided to perform dehydration bake of the wafer in a 185 °C oven for at least 24 hours. This was then followed by oxygen plasma ashing for 20 min at 100 W in a barrel asher (Emitech K1050X). Due to the photoresist's susceptibility to UV light, fabrication steps were carried out in a filtered yellow light clean room.

4.2.3.2 Formation of SU-8 2025 as adhesion layer

For good linkage between the pattern structure and the substrate, SU-8 2025 was required as an adhesion layer on the silicon wafer. First, the wafer was carefully placed on the central chuck within the spinner (Laurell WS-400B-6NPP/LITE). To prevent the wafer from spinning off the chuck during high speed rotation a vacuum was applied. Prior to spinning the wafer was centered onto the chuck and an adequate amount of SU-8 was poured onto the middle of the wafer. This was allowed to settle slightly before spinning. While the adequate amount can be estimated from experience, a simple minimum volume guideline is the product of the desired resist thickness and the surface area of the wafer. The resist was then spun for 10 s at 500 rpm (acceleration 84 rpm/s), followed by 30 s at 3000 rpm (acceleration 10030 rpm/s). The substrate was then soft-baked for 3 min at 65 °C and for 6 min at 95 °C subsequently on a hotplate (Stuart Scientific). A level hotplate with good thermal control and uniformity is recommended during this process. The reason for this baking step is to stabilize the resist film and eliminate any remaining solvent through evaporation. This ensures that the resist surface is non-sticking, hence avoiding debris on the chromium mask when transferring the patterns later. This is a critical step because failure to do so will affect the photoresist profile. After cooling down the substrate to room temperature, the whole substrate area was exposed to UV using a

Suess MA6 (Karl Süss GmbH, Germany) mask aligner. This method is called flood exposure, and it was performed to initiate cross-linking of the SU-8 2025 adhesion layer.

A mask aligner functions like a contact printer where it transfers a certain feature from a patterned mask to photosensitive material (SU-8 resist) through UV radiation exposure. During the exposure, a Kopp-34 filter and later PL-360 filter (Omega Optical) was placed on top of the mask to eliminate UV radiation below 350 nm. SU-8 resist polymerizes faster when exposed to shorter wavelength light below 350 nm. This often caused the upper layer of SU-8 to become overexposed and prevented the remaining SU-8 resist from being fully polymerized. This effect is commonly known as the T-topping effect [78].

The exposure dose is defined as the product of light intensity and exposure time as in Equation (4.4.1). Based on the SU-8 datasheet [77], the exposure energy dose of 150 – 160 mJ/cm^2 is administered for the thickness of 25 μm. Since the light intensity of the mask aligner lamp was measured to be 5.9 mW/cm^2 (filter included), the exposure time estimated from Equation (4.1.1) is 25 – 27 s. To simplify and avoid under-exposure, the exposure time was set to 30 s. The substrate was then exposed in multi-exposure mode for 3 cycles with each cycle exposure time of 10 s (3 cycles x 10 s = 30 s), with an interval of 60 s wait for every cycle in order to allow the resist to thermally relax between doses.

$$\text{Exposure Dose (mJ/cm}^2\text{)} = \text{Intensity (mW/cm}^2\text{)} \times \text{Exposure time (s)} \qquad (4.1.1)$$

Post exposure bake should take place directly after the exposure in order to continue polymerization by allowing cross-linking between resist epoxy and the newly exposed area. It also should remove any remaining solvent on the photoresist layer and improve the minor cleft defects structure (if any) on the photoresist layer. According to the resist datasheet, the post bake exposure of the substrate was at the temperature of 65 °C for 1 min followed by 6 min at 95 °C. The purpose of the two-step ramp between 65°C and 95 °C was to avoid high thermal stress in the SU-8 resist which can damage the film with cracks. The substrate was left to cool down to room temperature

with the temperature set to ramp down at 15 °C/hour. This was necessary in order to reduce film stress and avoiding cracking and adhesion problems [77, 79].

4.2.3.3 Formation of SU-8 2025 as channel layer

As previously mentioned, the device has to be covered with a glass coverslip in order to protect the micropillars, worms and channel from potential physical contamination, interference or damage. Thus an additional channel is required in order to provide a sufficient gap between the pillar tip and the glass coverslip. Concurrently, the size of this gap must be limited in order to prevent the worm from squeezing between the pillar tip and the glass coverslip. This additional gap was made by adding an SU-8 channel layer that was 20 μm greater than the height of micropillars. The substrate surface which was coated with the SU-8 2025 layer was then treated with plasma for 30 s at 100 W using the plasma asher. This was done to accommodate better adhesion between already deposited SU-8 resist and the subsequent SU-8 layer.

After that, an additional layer was formed by spinning SU-8 2025 for 10 s at 500 rpm, followed by 30 s at 4500 rpm in order to obtain the desired thickness of 20 μm. After spinning, the wafer substrate was transferred to a 65 °C hot plate, allowed to pre-heat at 65 °C for 1 min and then ramped to 95 °C for another 3 min. Once the substrate was allowed to cool down to room temperature, the outer channel layer pattern was exposed using the mask aligner. When the exposure was complete, post exposure bake was performed once again at 65 °C for 1 min followed by 5 min at 95 °C.

4.2.3.4 Formation of SU-8 2100 as micropillar layer

Since the pillar height was set to be 100 μm thick, the SU-8 2100 was spun for 10 s at 500 rpm, followed by 30 s at 3000 rpm in order to obtain the desired thickness. The substrate was then softbaked again for 5 min at 65 °C, and subsequently for 20 min at 95 °C on a hotplate. Once the substrate has cooled down to room temperature, it was UV-exposed through the formerly prepared chrome mask containing the micropillar pattern using the Suess MA6 mask aligner (filter included).

The UV light intensity was measured to determine the required exposure time for the photoresist thickness. The mask aligner brought both the mask and wafer into contact

(via vacuum mode) in order to limit undesirable diffraction effects and increase overall exposure resolution. The vacuum contact mode renders the closest contact and is implemented by drawing vacuum between the chrome mask and the SU-8 photoresist on the substrate. Consequently, this mode provides the best resolution on the transferred pattern. However, the shortcoming of this method is that part of the photoresist on the substrate can be damaged because, during removal, it often sticks to the chrome mask.

Once in contact, a 365 nm UV source with the measured intensity of 5.9 mW/cm^2 was applied with the exposure time of 10 s for 3 cycles. For every cycle, there was again a wait time of 60 s. The lower exposure dose, compared to the suggested value provided in the datasheet [77] was chosen because of the potentially higher resolution (less unwanted crosslinking), especially with a follow on flood exposure during the formation of the adhesion layer. The mask areas not covered by chrome transmitted the UV light through to the photoresist layer, crosslinking the photoresist in these regions and causing it to adhere to the wafer surface. Post exposure bake was performed once again at 65 °C for 5 min followed by 10 min at 95 °C.

Once the wafer had been ramped-down to room temperature, the substrate was removed from the hotplate for pattern development. Developing the exposed resist consisted of a timed bath in (1-methoxy-2-propyl)-acetate (PGMEA, Sigma-Aldrich) solvent, which removes non-crosslinked photoresist. It will also dissolve the crosslinked areas, albeit very slowly, if left for too long in the developing solution. The substrate was immersed in PGMEA in an ultra-sonic bath for the development for approximately 10 min. Figure 4.7 shows example of fully developed SU-8 holes and the effect of underexposure (see Section 4.5.1) leading to some of the SU-8 structures dissolving during development.

If minor cracks were visible, hard-baking was performed after development. During this, the substrate was baked for 20 min at 120 °C. Then, the substrate was left to cool down to room temperature with the temperature set to ramp down at 15°C/ hour. The effectiveness of hard-baking can be seen in Fig 4.8, where the initial cracks in the resist disappeared after this process was performed.

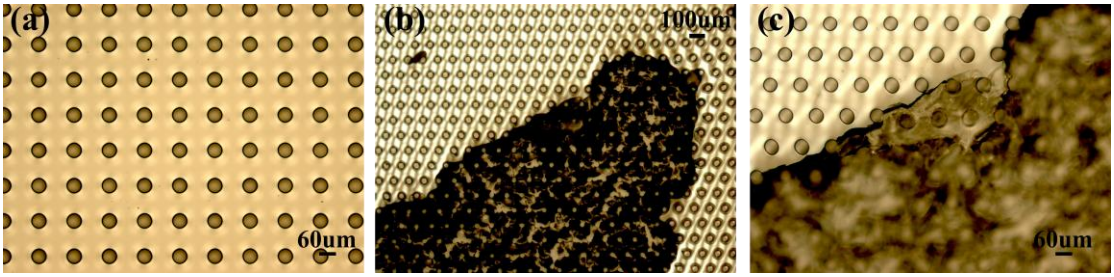

Figure 4.7: *Optical micrographs illustrating technical problems encountered during resist development. (a) An example of fully developed SU-8 holes (b) & (c) Effect of underexposure (See Section 4.5.1) leading to some of the SU-8 structures dissolving during development.*

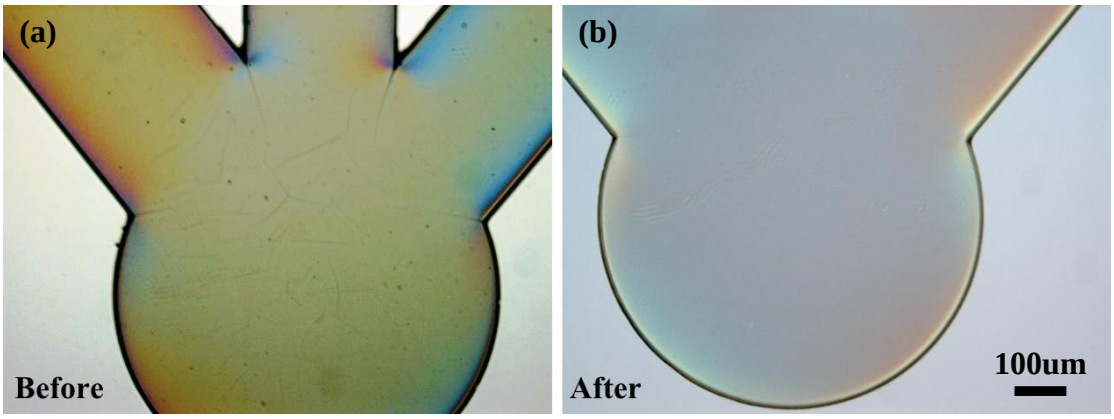

Figure 4.8: *Optical micrograph showing the hardbaking effect. (a) SU-8 before hardbake and (b) after hardbake. Stress cracking at the inlet is no longer visible after undergoing the hardbaking procedure.*

When the entire unexposed region had dissolved in the developer, and the exposed pattern was completely visible, the substrate was rinsed with IPA and finally blow-dried using a nitrogen gun. Afterwards, the substrate was inspected using an optical microscope to ensure that all unwanted structures had been developed/removed properly. At this stage, the final substrate (Fig. 4.9) now consisted of several hole structures with a layer height of 100 μm.

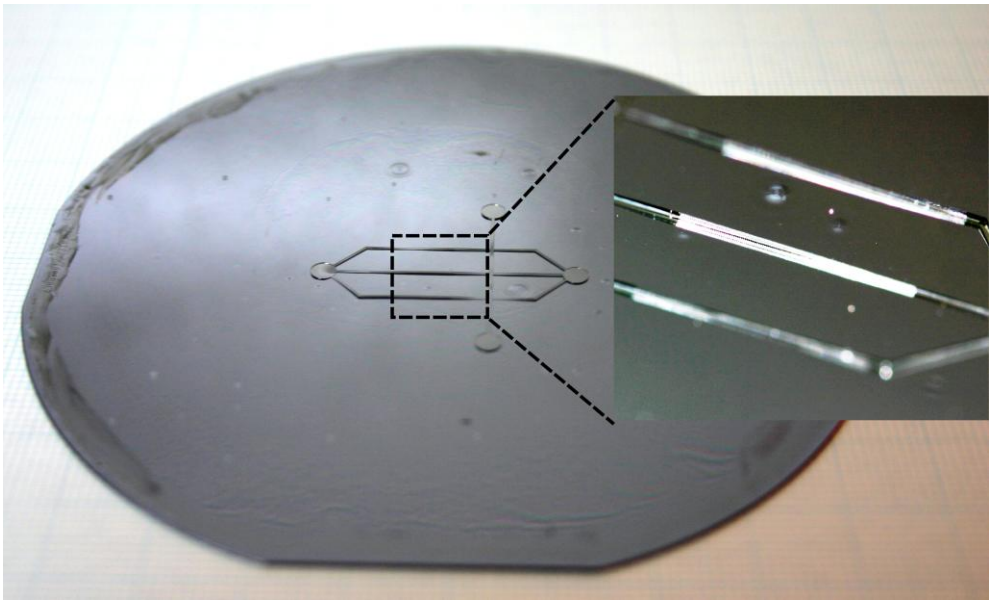

Figure 4.9: *Photograph of a developed SU-8 mold patterned with features of 100 µm height for soft-lithography and replica molding with close-up of the hole structure. The full wafer is four inches in diameter.*

4.3 PDMS Device Casting

The application of PDMS as an elastomeric molding substrate for the replication of well-defined structures from photolithography was developed by Whitesides et al. [72]. PDMS is a two-component heat-curing silicone polymer system which consists of a base part and a curing agent. When both components are mixed and cured at a specified temperature, the viscous polymer liquid crosslinks and changes into a solid elastic structure.

The polymer was weighed (in this work 30 g was able to produce ~ 1 cm thickness of PDMS layer on a 4 inch silicon wafer) and thoroughly mixed according to a base-to-curing agent ratio of 10:1 w/w. The PDMS (Sylgard 184, Dow Corning) mixture was then put into a vacuum desiccator in order to degas it which removes air bubbles that were introduced during the mixing. This was essential in producing a good, clean PDMS device. In the meantime, the surface of the SU-8 mold substrate that had been previously developed was treated by exposure to trimethylchlorosilane (TMCS, Sigma Aldrich) vapour for 2 hours. The coating of TMCS prevented adhesion between the SU-8 mold and the curing PDMS. When the two components of PDMS

were insufficiently mixed, some of the polymer was observed to remain on the mold. This prevents further usage of the SU-8 mold for replica molding application. The surface treatment of the SU-8 mold was conducted inside the fume hood in the Nanofabrication Laboratory yellow room as TMCS is a very corrosive chemical.

In order to confine the liquid PDMS within the area of the SU-8 mold, a metal bounding ring with a size similar to the silicon substrate wafer was placed at the wafer edge. The polymer mixture was then poured onto the mold within the bounding metal ring and enclosed with a weight at the top in order to prevent any leakage of the PDMS liquid polymer. The whole assembly was transferred into the vacuum desiccator and degassed again to ensure that all air bubbles were removed. The mold was then baked on a hot plate for 1 hour at the temperature of 80 °C in order to harden. After cooling it to room temperature, the PDMS replicas were carefully peeled off from the SU-8 mold and were cured for a further 3 hours at 80 °C to ensure that the pillars were fully hardened and that the material properties had stabilized. Individual devices were then cut out using a scalpel and placed on microscope slides for handling. Figure 4.10 depicts the fully developed SU-8 mold structure with the PDMS replication displayed on the right side of the image. The complete process parameters for the fabrication process of the SU-8 mold are summarized in Table 4.2.

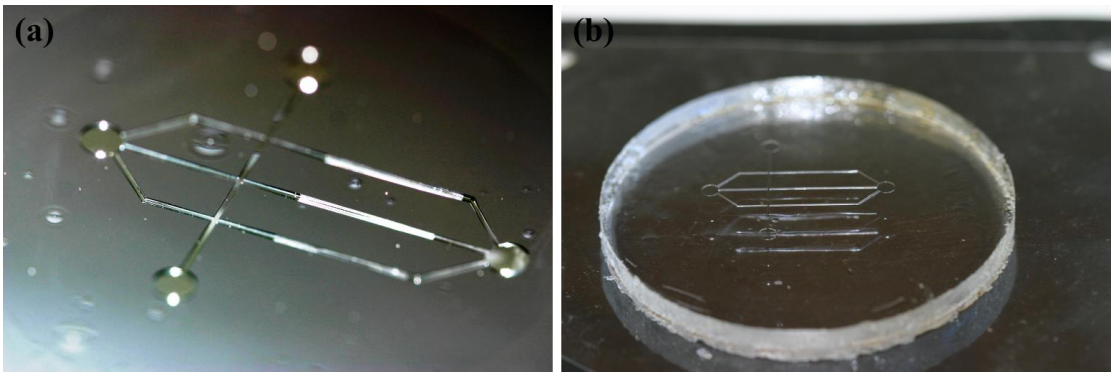

Figure 4.10: *Optical photographs of the fabricated devices (a) Photoresist patterns on the developed silicon master wafer (b) Resulting PDMS cast after de-molding.*

Table 4.2: *Process parameters for fabrication of SU-8 mold for* C. elegans *force measurement device.*

Process	**Parameters**
Substrate pre-treatment	Dehydration bake at 185 °C Plasma O_2 asher 20 min at 100W
Coat SU-8 2025 adhesion layer	500 rpm for 10 s, 3000 rpm for 30 s
Soft-bake	65 °C for 3 min, followed by 95°C for 6 min
Exposure	Flood exposure (multiple) 3x(10 s + 60 s wait)
Post-exposure bake	65 °C for 1 min, followed by 95°C for 6 min. Ramp down to room temperature at 15°/hour
Surface adhesion treatment	Plasma O_2 asher for 30 s
Coat SU-8 2025 channel layer	500 rpm for 10 s, 4500 rpm for 30 s
Soft-bake	65 °C for 1 min, followed by 95°C for 3 min
Exposure	Vacuum contact (multiple) 3x(10 s + 60 s wait)
Post-exposure bake	65°C for 3 min, followed by 95 °C for 6 min. Ramp down to room temperature at 15 °C/hour
Coat SU-8 2100 pillar layer	500 rpm for 10 s, 3000 rpm for 30 s
Soft-bake	65 °C for 5 min, followed by 95 °C for 20 min
Exposure	Vacuum contact (multiple) 3x(10 s + 60 s wait)
Post-exposure bake	65 °C for 5 min, followed by 95 °C for 10 min. Ramp down to room temperature at 15°/hour
Develop	10 to 15 min in PGMEA using ultrasonic bath
Hard-bake	120 °C for 20 min. Ramp down to room temperature at 15 °C/hour

4.4 PDMS Micropillars Visual Inspection

Two types of visualization inspections were performed in order to verify that the micropillars were fabricated correctly. The first method uses the surface profilometry (Dektak 150) to measure feature dimensions and capture micropillar images. Although the main function of this device is surface profile measurement, optical images can also be captured using the camera installed. The PDMS device sample was loaded on the sample stage with the area to be captured centered below the stylus. From the captured images, initial visual inspection can be conducted on the PDMS micropillar arrays (see Fig. 4.11).

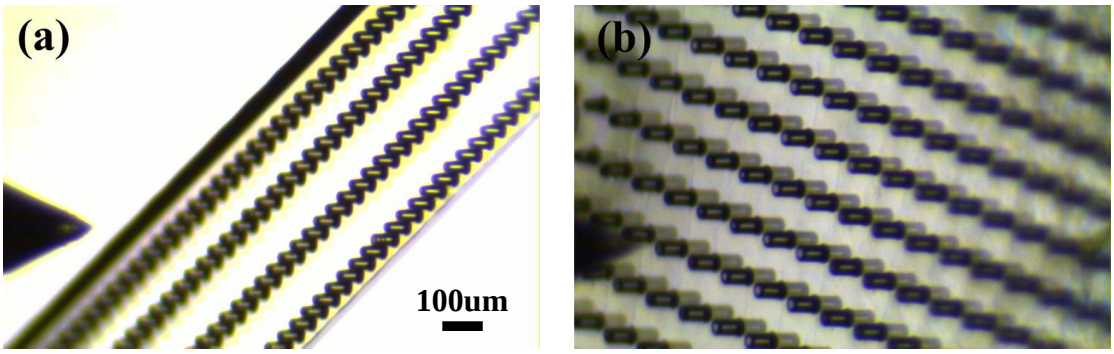

Figure 4.11: *Optical micrographs of PDMS micropillars during visual inspection using the DEKTAK surface profilometry. (a) Four pillar array (Design 2) inside microchannel (b) Large area corresponding to Design 3.Scale bar applies to both images.*

For higher resolution images, Scanning Electron Microscopy (SEM) was used to capture images of the PDMS micropillars. SEM imaging involves scanning the sample surface using an electron beam, and the sample surface will accumulate charge if there is no conductive path for the electrons to escape. Consequently, the image formed by SEM will be very poor if no conductive path exists. Since PDMS is an insulating material, the polymer device was initially coated with thin metal layer (10 nm Gold Palladium) using a sputtering machine to prevent surface charging.
Figure 4.12 shows four different sets of PDMS pillars images captured using SEM.

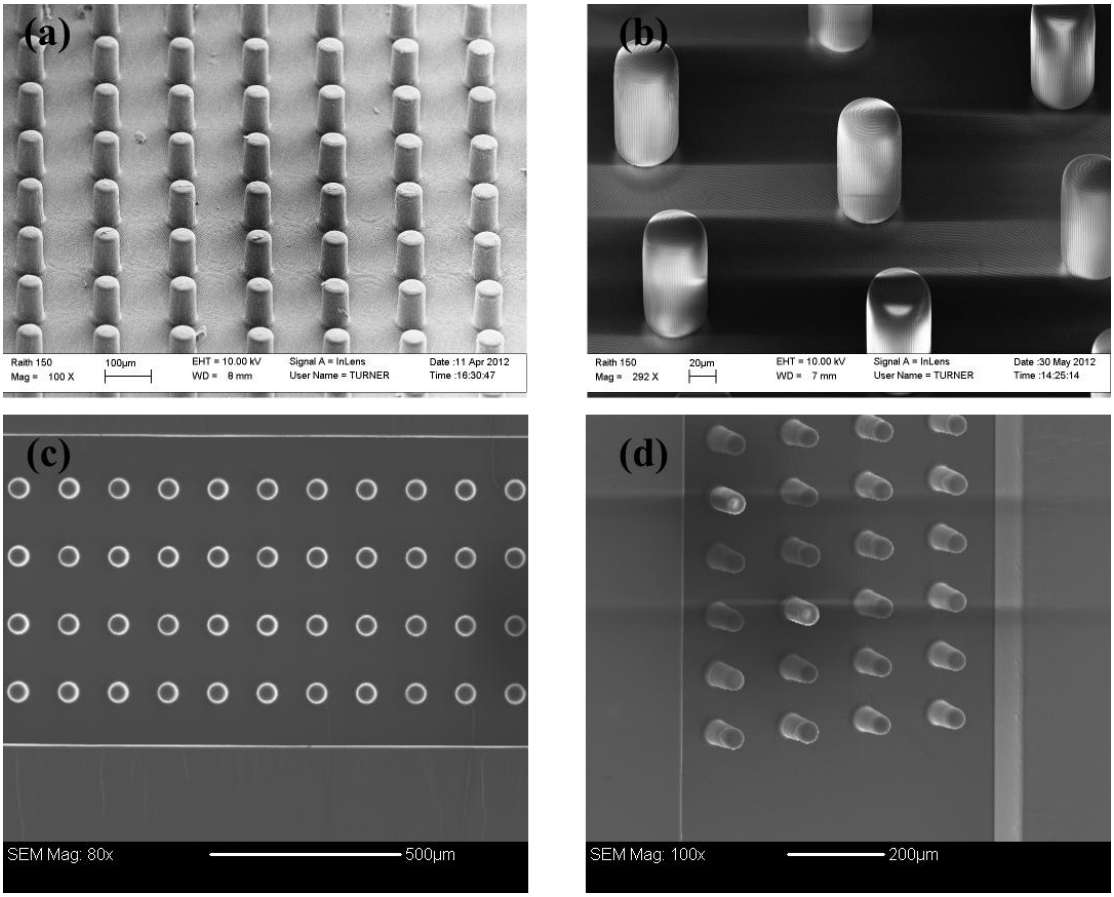

Figure 4.12: *SEM images of PDMS micropillars showing (a) lattice pillar arrangement (b) honeycomb design structure, (c) top view of four pillar array in a channel, and (d) PDMS micropillars initially fabricated in four-arrays inside the channel.*

4.5 Fabrication Challenges and Limitations

Although the final design in this work has been successfully built and established, there were some problems and fabrication limitations encountered, in particular to achieve a fully optimized micropillar. This section discusses the problems and challenges faced while conducting device fabrication.

4.5.1 Exposure dose optimization

The pillars were made using PDMS replica molding from the hole structures created in SU-8 photoresist. To achieve a perfect pillar, all the resist in the hole has to be completely dissolved during the development using PGMEA. The efficacy of this process depends on the parameters used during exposure of pillars mask on the SU-8 layer. For the case of SU-8 negative photoresist, the exposed image pattern is insoluble in the developer and the unexposed region is etched away. If the energy from the UV light of the mask aligner is insufficient, the chemical reaction is incomplete, resulting in an image pattern that is over etched during development. If the energy from the UV light causes over-exposure, the image pattern will not or only partially develop. In the case of high-aspect-ratio holes, the creation process is more challenging primarily because of the difficulty to completely develop the SU-8 photoresist all the way to the bottom of the holes. If the pillar structure requires tall and narrow holes, it is sometimes difficult for the PGMEA developer to reach the bottom of the holes structure.

The fabrication processes have been repeated many times with variations in the exposure time. Even though the exposure dose recommended by the manufacturer is in the range of 150 to 160 mJ/cm^2, the exposure dose was varied to the maximum of 550 mJ/cm^2 and the minimum of 110 mJ/cm^2. When a higher exposure time was applied, the holes could not be developed at all, leaving no pillars visible in the PDMS device.

The development technique was also modified where medium to strong agitation was used during development, as it has been reported necessary to ensure that the unexposed resist in very deep trenches is dissolved [75]. A different approach has also been tested in which, instead of using PGMEA as the developer, the wafer is immersed in stronger chemical called cyclopentanone followed by IPA rinse and after that, PGMEA is used. However this was ineffective and both techniques did not manage to fully develop the hole structures in the SU-8 resist. In contrast, while the lower exposure dose did result in all holes being developed, the methods were ineffective as there were a lot of cracks visible. In addition, the aggressive methods also resulted in collapsed channel wall structures. Figure 4.13 and 4.14 shows the effect of both maximum and minimum exposure on the SU-8 mold pattern structure.

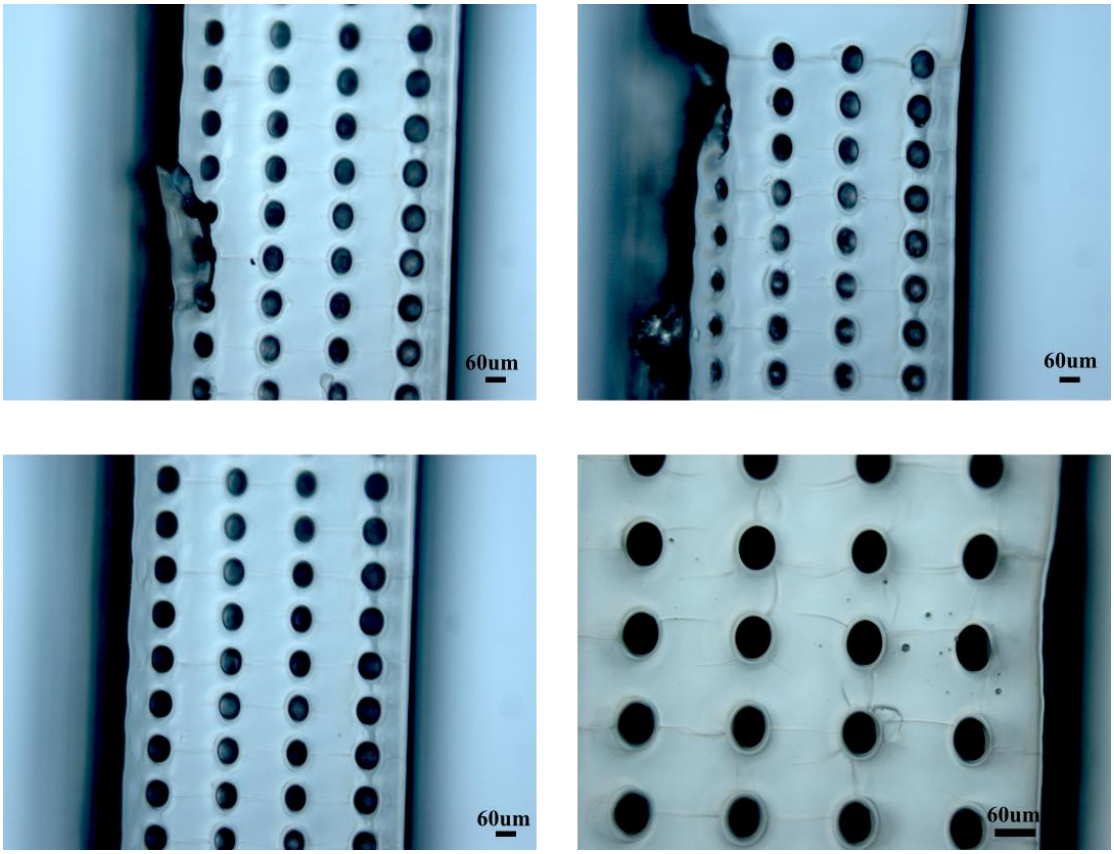

Figure 4.13: *Optical micrographs showing underexposure effects in fully developed SU-8 holes structure (bottom) which led to imperfect channel structure (top).*

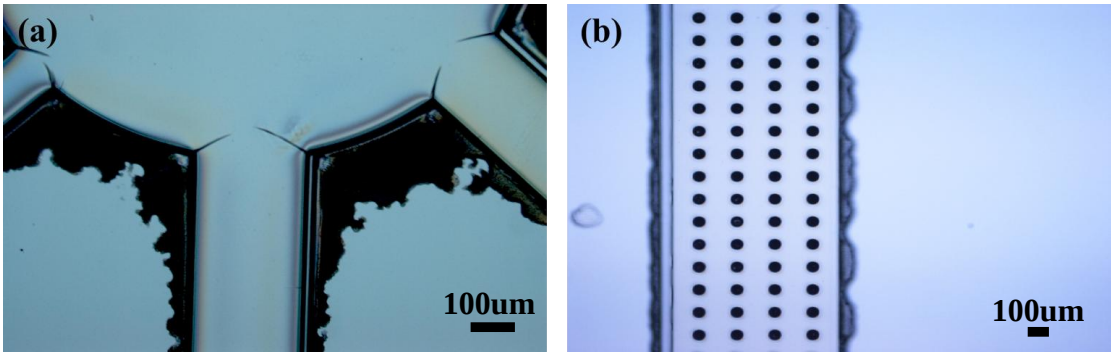

Figure 4.14: *Optical micrographs of undeveloped SU-8 layer pattern definition as shown at (a) the edge of the inlet and (b) the channel due to overexposure effects.*

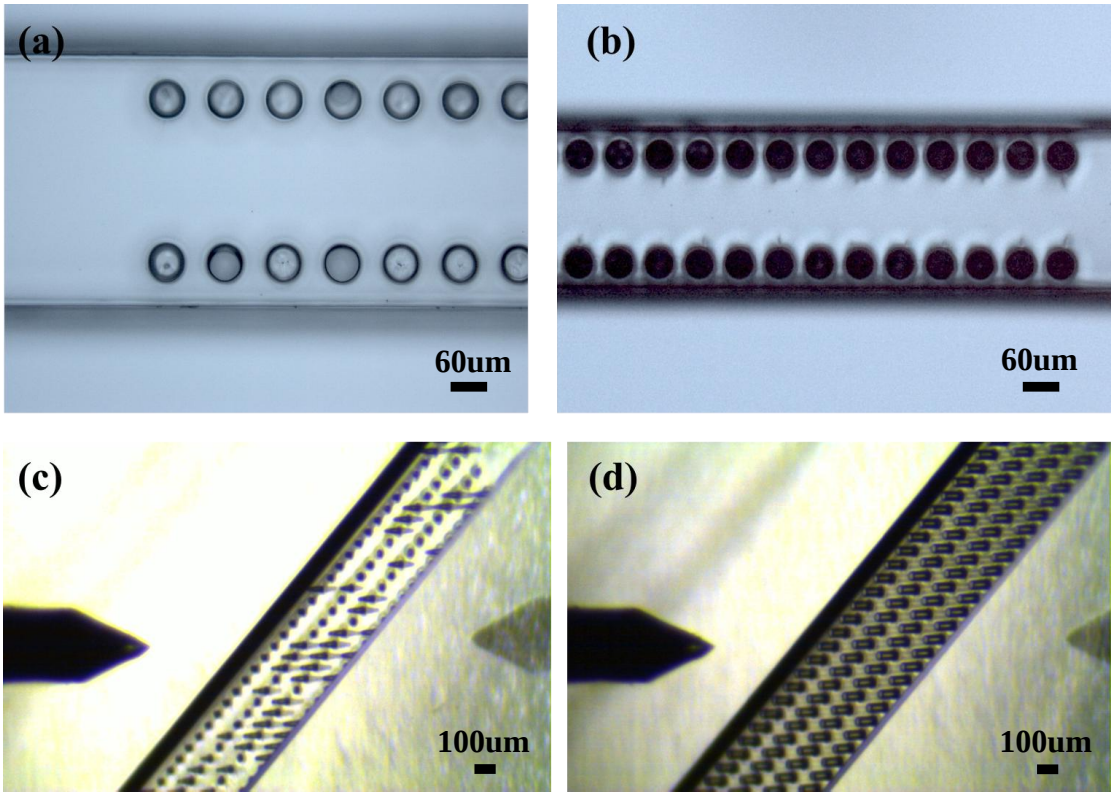

Figure 4.15: *An example of (a) fully developed versus (b) partially developed holes in SU-8 photoresist. (c) Pillars with 40 μm diameter are hardly produced after PDMS replica de-molding compared to (d) 60 μm diameter pillars perfectly filling the whole channel.*

4.5.2 Producing high aspect-ratio micropillars

As described earlier in this chapter, the pillar must have sufficient height to match the worm body, while the pillar diameter must allow for deflection in order to conduct very sensitive force measurement. The pillar diameter needs to be sufficiently small as to allow deflection. Initially, the pillar diameter was set to 40 μm. This however led to a very low success rate of pillars replicated in the PDMS cast, even though the exposure dose has been optimized (see Fig. 4.15). This is because during contact printing, the edges of the mask patterns commonly caused diffraction effects. When the photoresist thickness and the gap between the chrome mask and the photoresist increase, larger diffraction errors can occur [80]. Therefore, the sidewalls of the exposed photoresist structures were at risk of becoming non-straight after exposure. This effects provides a constraint on the capability of producing microstructures with very high aspect ratios. Furthermore, the optics system of the mask aligner in the

Nanofabrication laboratory is optimized for AZ1518 photoresist for the thickness of around 1 to 2 μm instead of 100 μm for SU-8 photoresist.

There are two possible options available in order to resolve this issue: (1) using deep reactive-ion etching (DRIE), an anisotropic etching process that enables the creation of deep holes structure in silicon substrates. Unfortunately, this facility is not available in the Nanofabrication laboratory. (2) To create the PDMS micropillars from SU-8 micropillars. Three sets of SU-8 micropillars were fabricated with smaller diameters of 10 μm, 20 μm and 30 μm. The pillar height was 90 μm (see Fig. 4.16).

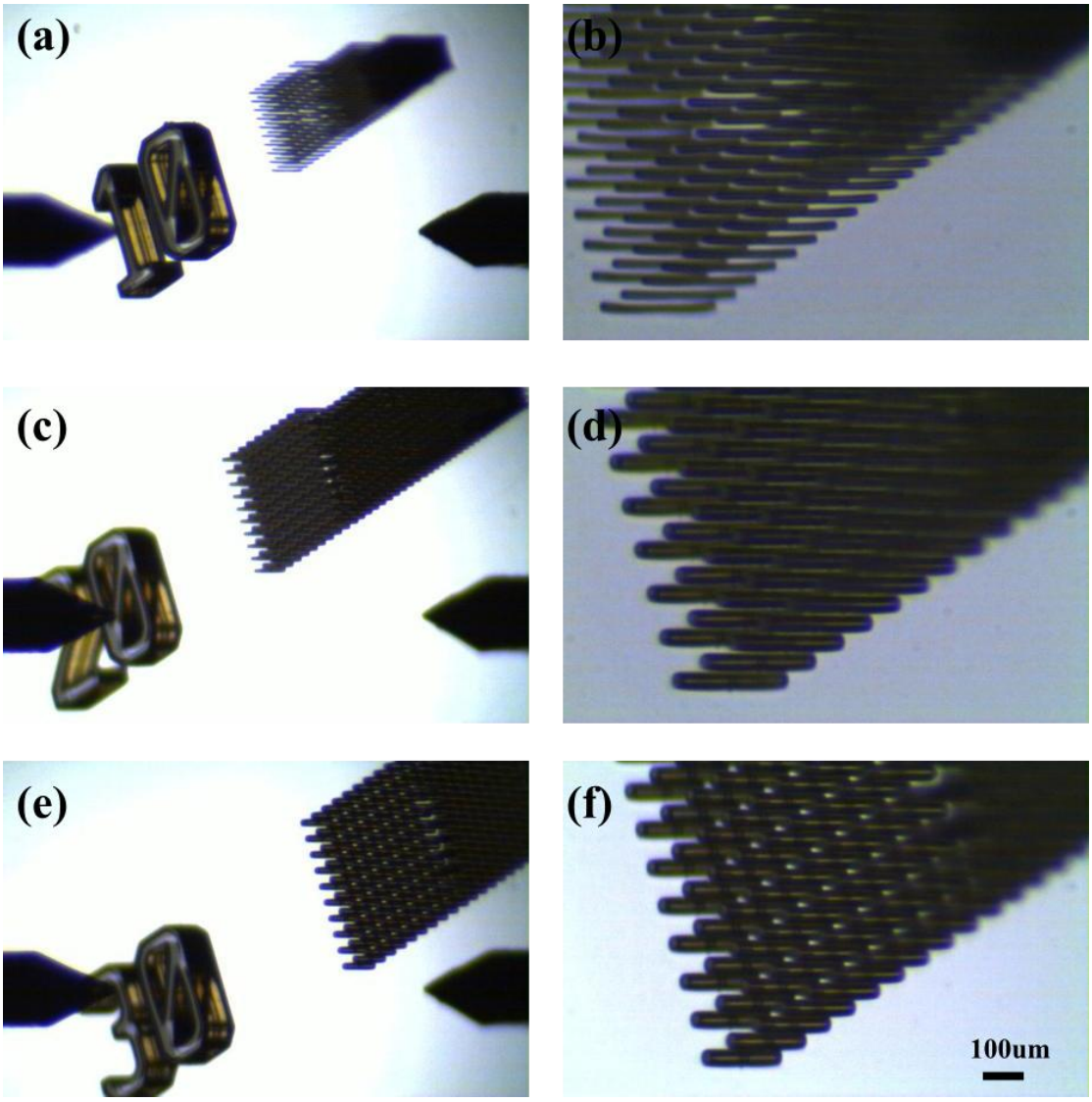

Figure 4.16: *Optical micrographs of SU-8 micropillars with diameters of (a) 10 μm, (b) 20 μm and (c) 30 μm.(d)-(e) Close up of the respective pillars. Images courtesy of Dr. Volker Nock. Scale bar applies to all images.*

The idea is to replicate the micropillars made of SU-8 into PDMS holes structure. The PDMS structure will then be replicated again in order to produce the PDMS micropillars. Casting PDMS over PDMS is very challenging however, particularly when peeling one layer off the other as the adhesion between both layers is very strong. The double casting technique of PDMS was implemented by following the protocol provided by Gitlin et al. [81]. Though it was possible to peel the two PDMS layers off each other, the experiment was not a success because no micropillars were observed on the replicated PDMS structure. Peeling PDMS from the SU-8 micropillar mold was very tricky indeed, as one has to be very careful in order to prevent the micropillars from breaking. Likewise, peeling a PDMS layer of another PDMS layer will be even more delicate. In this work, this has not been successful.

4.5.3 Cracks in SU-8 structure and misalignment

Another problem which arose during fabrication was the formation of cracks at the edge of structures (see Fig. 4.17 (a)&(b)). While cracked master structures do not significantly affect the device function as a whole, the cracks will eventually affect the cast of the PDMS layer as the mold will be used repeatedly to produce the PDMS cast. The reason behind crack formation in SU-8 structures is mainly due to low exposure dose and inner stress of the resist during post-exposure bake. Therefore it is important to keep a low ramp-down temperature during post-exposure bake.

The addition of the channel layer prior to the deposition of the SU-8 2100 layer for the micropillar structure requires precise alignment during exposure. One of the problems was the misalignment between those two layers. Figure 4.17(c) shows the resulting misalignment which can appear either during exposure or due to delaminating of the top layer. In order to resolve this issue, alignment marks are necessary on both channel and micropillar masks to ensure that the pillars fit perfectly into the channel layer.

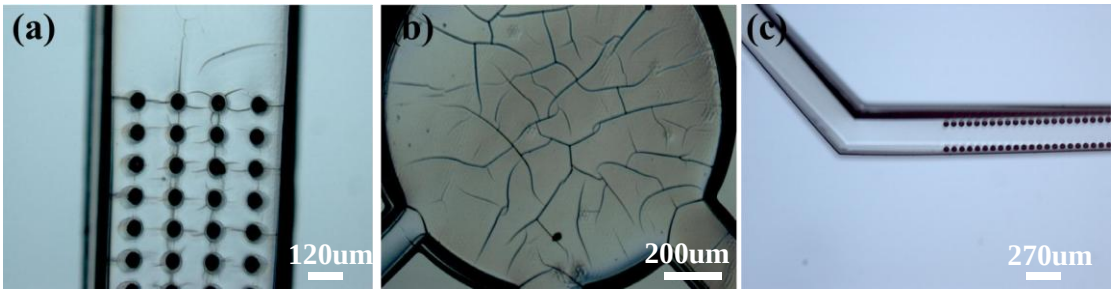

Figure 4.17: *Cracks formed after development due to underexposure (a) between the hole structures and (b) at the device inlet. (c) Misalignment and adhesion failure between the channel and the pillars.*

4.6 Summary

The design and fabrication of a microfluidic devices for force measurements using arrays of PDMS micropillars was demonstrated. The design of the PDMS device underwent several iterations before a final solution has been reached. The primary issue was the pillar arrangement, wherein careful consideration has to be made in order to provide the best environment for force measurement experiments to succeed. Two initial designs have been reviewed and the design challenges that appeared during the process have been discussed. These include the squeezing into the channel wall that mimic the worms' burrowing behaviour, along with the negligible deflection of the pillars due to insufficient pillar spacing and arrangement. Solutions to the aforementioned problem have been proposed and implemented in the final design. Following this, the SU-8 mold fabrication procedures and the replication of the PDMS device using soft lithography have also been explained in detail. Though the existing SU-8 mold fabrication methods proposed in the literature were found to be reliable, additional steps were included, in particular the deposition of the adhesion layer at the beginning of the SU-8 mold preparation. This was done to avoid the material incompatibility between the silicon wafer substrate and the SU-8 resist pattern. The production of high aspect ratio features of reproducible quality is still a challenge. Particularly related to this research, the use of DRIE and changing the optical systems of the MA6 mask aligner to match SU-8 photoresist compatibility could be the potential solutions.

CHAPTER 5

Vision-based Force Measurement and Case Study

In the previous chapter, the development of the PDMS device has been outlined in detail including the progression of the prototype design and the fabrication protocols. The properties of the PDMS elasticity have also been characterized in Chapter 3 by the experimental measurement and determination of its Young's modulus value. The first section of this chapter will discuss specifically the actual finalized experimental setup that utilized the PDMS device developed in Chapter 4. This includes the worm and device preparation, data collection and the post-processing using a vision-based algorithm in order to resolve the deflection of the micropillars by the worms' movements. Subsequently, the results obtained from two experiments using device Design 2 are analyzed and summarized. The generated force pattern coupled with the locomotion patterns of interest is discussed. To further validate the findings from these results, comparisons will be made with the existing published work. The presented work in this chapter demonstrates the potential and applicability of the device which will be discussed in the next two chapters.

5.1. Experimental Setup

This section describes the handling of the PDMS device and the nematode *C. elegans* for data collection. In general, the PDMS device is prepared for the insertion of the worms, which are required for the experiment. A worm's movement is then captured via video filming before being post-processed in order to measure the deflection of specific individual pillars. Figure 5.1 shows the complete experimental setup of the *C. elegans* force measurement device system.

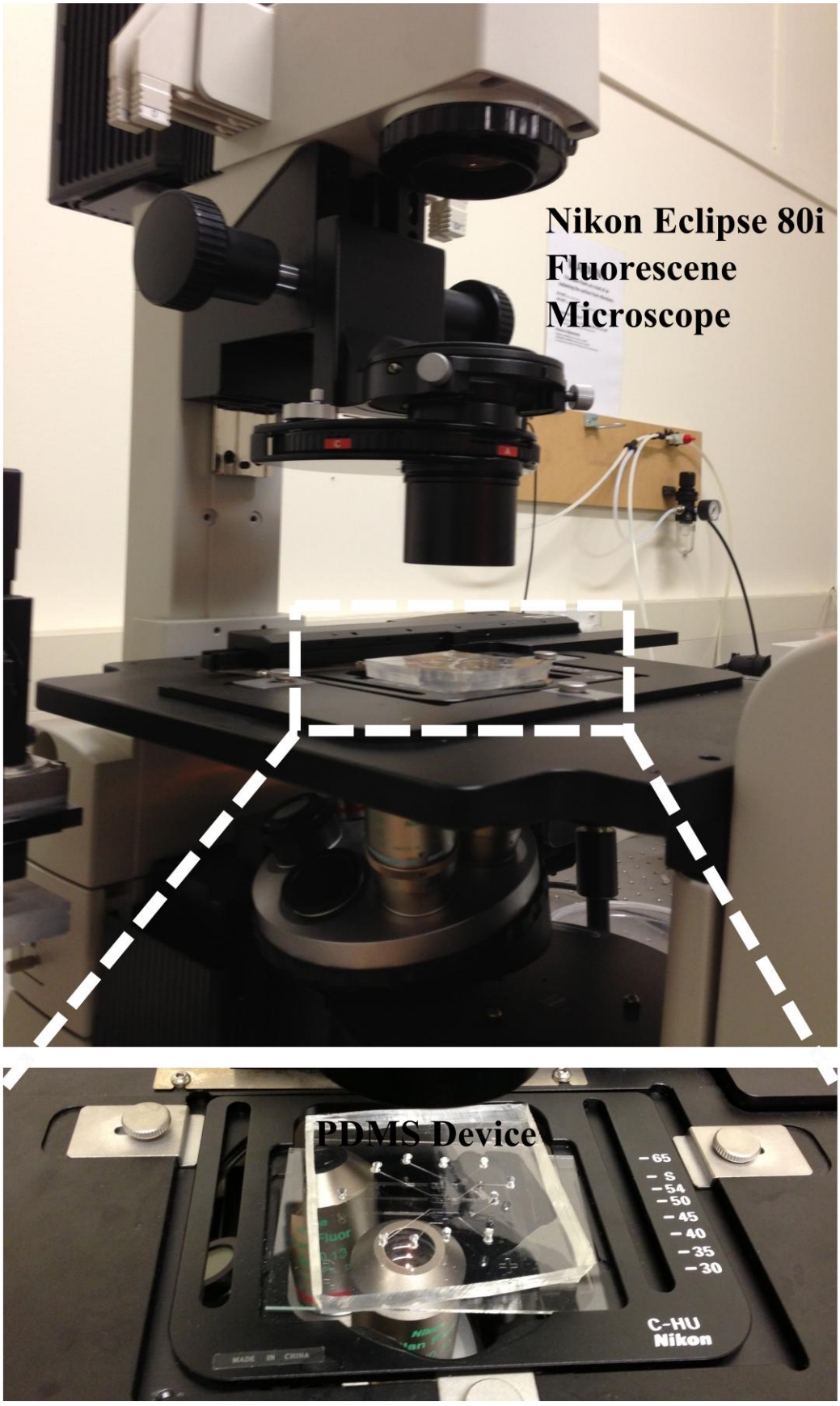

Figure 5.1: *Experimental setup comprising the PDMS device on the microscope stage.*

5.1.1 PDMS device preparation

The preparation of the PDMS device and the introduction of the worm into the device will be discussed here in detail. Following the casting of the PDMS which has been described in Chapter 4, the cured polymer was cut using a scalpel and placed on a glass slide for easier handling during the experiments. Prior to nematode loading, the PDMS device surface was treated using a corona wand (Electro-Technic Products) to ensure the device is hydrophilic. Then, to mimic the nematode natural habitat, the device was filled with DI water to provide a moisturized environment for worm locomotion. The amount of water was carefully controlled in order to produce a very thin layer of liquid throughout the device chamber.

5.1.2 Worm culture, maintenance and preparation

Wild-type *C. elegans* strains (N2) were used for this study where a plate containing the nematodes was originally obtained from Hopkirk Research Institute, New Zealand. Several procedures have to be conducted in order to maintain the availability of the worms throughout the entire research period. The procedures are called subculture, where a certain area of the original plate was cut and transferred to the Nematode Growth Medium (NGM). NGM agar was prepared according to Brenner [6]. The following describes the general procedures required for the subculturing process of *C. elegans*. Detailed media recipe preparation protocols can be obtained from [82].

Day 1: Preparing NGM agar and *E. coli*

Approximately one liter of NGM was prepared and this was poured into 20 to 25 medium-sized Petri dish plates until the dishes were about half full. The plates were allowed to cool to room temperature and solidified overnight before being stored in a refrigerator at 4 °C. For better work organization, it is advisable to prepare the plates in advance of the experiment time. In the meantime, *E. coli*, which is the bacteria used as the worms' food is prepared. Primarily, a single *E. coli* (OP50) colony is isolated

into a 100ml Lysogeny broth (LB) medium, which is a nutrition rich medium used for bacteria growth. The bottle is then set overnight at 37 °C for the bacteria to grow and should be cloudy during the next day due to the growth. The broth medium can be used for up to 3 months if kept in a 4 °C refrigerator.

Day 2: Seeding NGM plates with *E.coli*

The NGM plate is taken out of the refrigerator and cooled down to room temperature. Once ready, about 300 µl of E. coli is dropped to the center of the plate using a micropipette. A sterile glass rod is used to spread the bacteria pool evenly in the center and the plate is left overnight at 37 °C to allow a bacterial lawn to be formed. Seeded plates can be used for approximately one week prior to worm transfer. The remaining unused plate can be kept in the refrigerator where it can be used at later times for the next seeding.

Day 3: Transferring worms

Worms are transferred onto a seeding plate using a method called "chunking", where a small dice (~1 x 1 cm) of the original culture medium is cut out using a scalpel. Typically, the worms reside on the top surface of the agar plate where the food source is available. The cube is removed from a region of the medium with a high density of worms and flipped before placing it onto the previously prepared seeding plate. This is to ensure that the majority of the worms which are on the surface of the agar have immediate access to the food. Worms are normally cultured at 20°C room temperature, with the plates placed upside down in order to prevent water condensation from mounting up and disturbing the worm culture. The plates are left for 3 to 4 days for the worms to multiply. It is necessary to check the culture plates daily in order to make sure that the worms are not starving out. Once the bacterial lawn had started to dry out, and only a small amount of worms remained visible on the culture plate, the whole culture process is repeated again so that the *C. elegans* culture can be maintained.

In order to ensure that only young adult *C. elegans* were used during the experiment, worms were only used 47 hours after the seeding in the culture to allow time for the development of the nematode into the young adult size [83]. The Petri dish was placed under a stereo microscope (Olympus SZX12) for better visualization of the worm. A platinum wire was used to pick the worm, where the tip of the wire was lowered carefully and slowly before gently swiping the tip at the side of the worm's body. One has to be very careful when picking the worm as to avoid injuring the worm using the wire tip. One way to avoid this is by swiping a blob of *E. coli* at the wire tip and gently touching the worm, which caused the worm to stick to the bacteria at the wire tip. Then, the worm was individually placed very carefully inside the device. Once inside, the worm was given at least 5 min to physically adjust to the PDMS environment. The device with the worm was then placed on the microscope stage (Nikon Eclipse 80i) where information of the worm movement through the pillar arrays could be collected.

5.2 Data Collection

When both the PDMS device and the worms are ready, the experiment is continued by performing the data collection. This step results in a video clip that records the worm's movement inside the PDMS device. In this study, a digital camera (DS-5Mc, Nikon) was connected with a Nikon Eclipse 80i fluorescence microscope for video recording.

Initially, the PDMS device containing the worm was placed on the microscope stage. Following that, the light source of the microscope was adjusted so that a sufficient amount of light was applied to have the optimum view the PDMS device. In practice, the specimen viewing is always begun at the lowest magnification. The desired objective was then selected from the rotating module of optics that is available within the microscope [84]. For data collection in this work, 10x objective magnification in bright-field mode was used for imaging.

A digital camera (DS-5Mc, Nikon) was used to record the video with a field of view that encompassed both the worm and surrounding pillars. Each video was recorded at a frame rate of 5 Hz for subsequent force analysis. The frame rate depends on the type of digital camera used. For higher frame rate, high-speed digital camera could be used. The image segments were recorded while the stage was kept stationary. The only exception to this was that during the recording, the microscopy stage was manually moved in a discrete manner only when the worm was about to move beyond the field of view of the camera. This is necessary for reducing any potential disturbances caused by the stage movement on the worm's locomotive behaviour.

5.3 Post-processing

Once the video has been taken, the post-processing involves two steps:

(i) Choosing specific pillars that were involved with the worm during motion
(ii) Post-processing of the video of these specific pillars in order to resolve the deflection

5.3.1 Choosing pillars for force measurement

During post-processing, it is necessary to choose the pillars that will be used for *C. elegans* force measurement as only the pillars that were influenced by the worm's movement are of interest. Since the captured video contains all the pillars (both in contact and not in contact with the worm), it is beneficial to focus only on the deflected pillars. In addition, separating the non-contact pillars from contact pillars can improve the efficiency in terms of the image processing time.

Through visual observation, it was found that the worms quickly adapt to the new environment as they continuously generated smooth crawling motion without major difficulty. During the observed course of motion, different sections of the worm, from head to tail, were in contact with a certain number of micropillars, depending on the worm size and pillar spacing. Each pillar can be regarded as an individual cantilever beam which functions as a force-measuring unit dedicated to one individual *C.*

elegans. Thus only the pillars that were observed to be in contact with the worm's body throughout the entire recorded video were chosen for force measurement.

Figure 5.2 illustrates four different worm's positions inside the PDMS device. As described in Section 4.1.2, three sets of design prototypes were developed, namely Design 1, Design 2 and Design 3. Depending on the pillar layout and arrangement in the associated designs, it can be seen that the number of pillars that are in contact with the worm during motion varies. From four to five in a four pillar array device (Design 2) up to eight to ten pillars a 9x9cm chamber full of pillar arrays (Design 3) were observed to be in simultaneous contact with the worms.

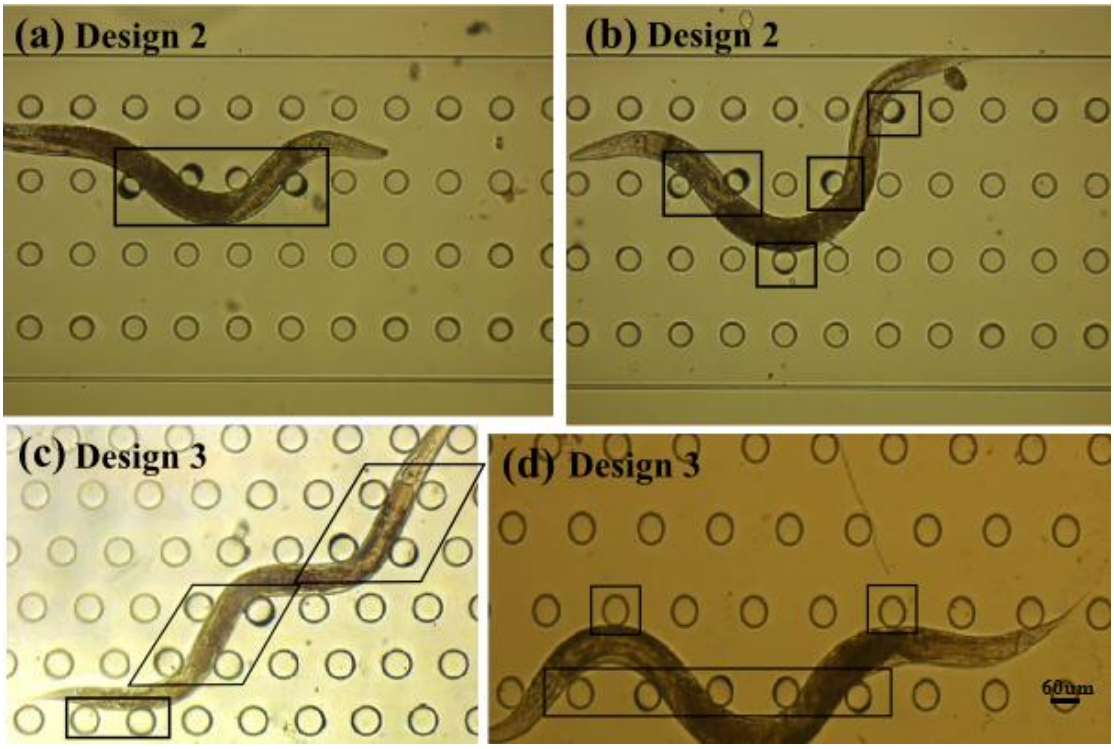

Figure 5.2: *Optical images of* C. elegans *body in contact with (a) four, (b) five, (c) ten and (d) eight pillars depending on the pillar spacing and arrangement.*

The feasibility of the post-processing method is demonstrated using the prototype device Design 2, consisting of four pillar arrays set within a channel (see Fig 5.2(b)). When the worm was placed into the device during the conducted experiment, it started to make contact with only two pillars, and throughout the motion, the worm was in contact with five different pillars. Therefore, these five pillars were then chosen manually so that the deflection measurements of each of the pillars can be calculated. In this instance, as seen in Fig. 5.3, these five pillars were identified and

named as P1, P2, P3, P4 and P5. The subsequent steps described in the post-processing section will examine only the forces and deflections of these five particulars pillars. This is necessary as separating the non-contact pillars from contact pillars can improve accuracy and efficiency in terms of the processing time.

5.3.2 Image processing and deflection measurement

In order to calculate the corresponding forces using the established linear force-deflection model described in Chapter 3, an image processing algorithm was developed to determine pillar deflection vectors. Although the image processing algorithm has been discussed in section 3.8, this section will demonstrate the visual deflection measurement of a video obtained from actual experiment.

As previously mentioned, the experiment was conducted using the second prototype device Design 2, where the device consists of four pillar arrays set within a channel (see Fig. 5.2(a)). A video with a duration of 12 s was captured and converted into 60 frames of image sequences.

Using Matlab, the algorithm starts by reading the original image frame (see Fig. 5.3(a)) which normally contains a full view of *C. elegans* and the surrounding pillars. The image is then cropped (see Fig. 5.3(b)) so that only the desired section of the worm's body that was in contact with the measurement pillars is visible.

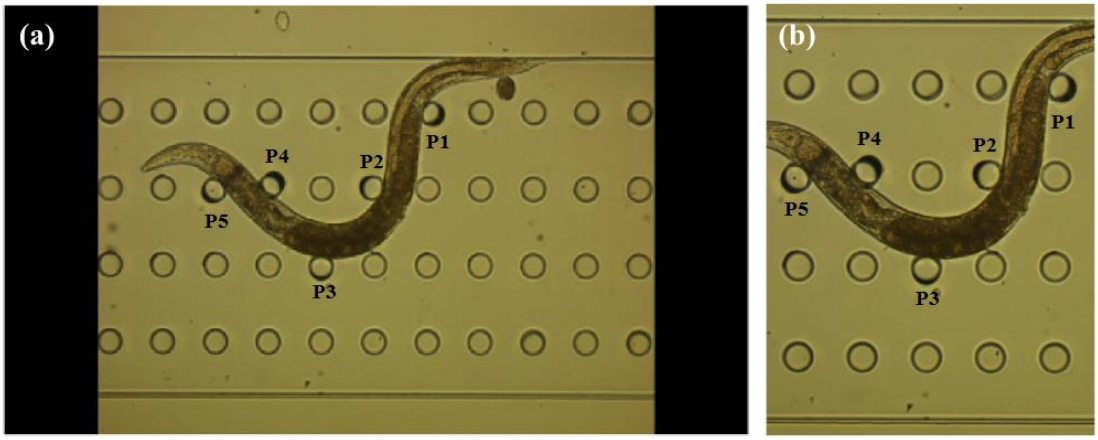

Figure 5.3: *(a) The original image read during image processing from one of the 60 frames of a sequence. (b) Cropped image retaining only the area with the five selected pillars.*

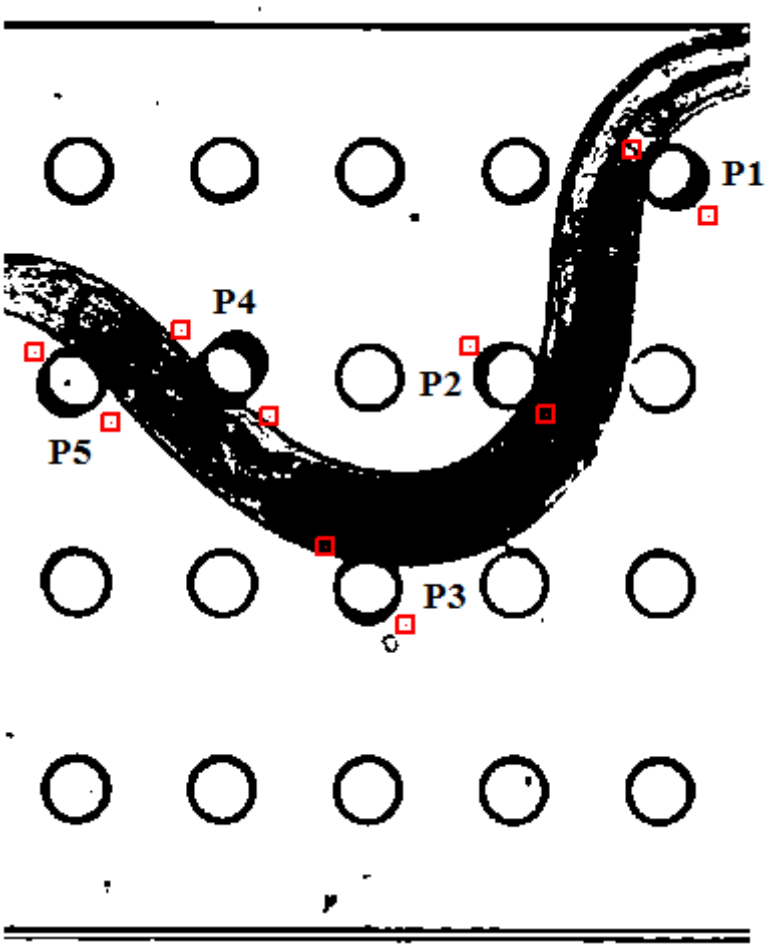

Figure 5.4: *Converted binary image with the area around the five selected pillars defined using red markers.*

The image frames were then converted to black and white for binary images and the edge coordinates of the area windows for the five selected pillars were determined manually. This is shown in Fig. 5.4.

The deflection is equivalent to the displacement of the pillar circle center with respect to its neutral position where the load is zero. In order to track the circumference of each of the five selected pillars, an image function of "bwtraceboundary (BW,P_0, FSTEP,CONN)" [85] was utilized to trace the outline curve of the selected pillar in binary image, BW. For each pillar curve, an initial tracing pixel, P_0 which is a two-element vector specifying the row and column coordinates of the starting point of the pillar curve boundary was manually selected. The search direction was then defined by the FSTEP strings such as north ('N'), east ('E'), south ('S') and west ('W'). One has to be careful when selecting the pixel starting point and its direction as it can affect the final traced outline of the associated figure. The continuation of the tracing function is defined manually by using the command 'connectivity' or CONN, where it can have either 4 or 8 scalar values. Figure 5.5 illustrates the possible values for FSTEP with the CONN values of 4 and 8.

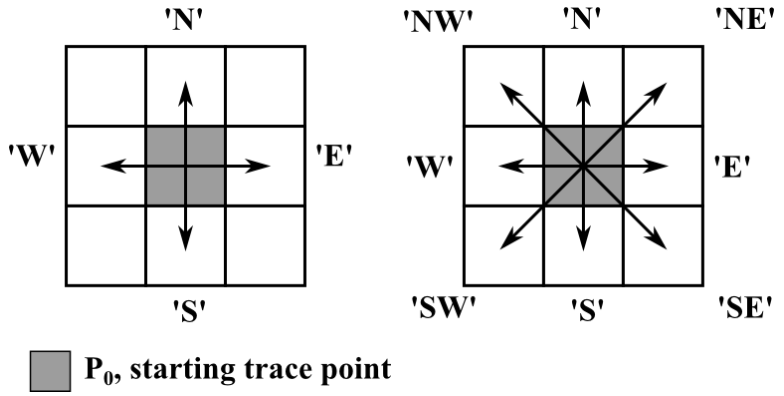

Figure 5.5: *Schematic of a 3x3 pixel neighborhood with tracing direction notation of 4-connectivity (left) and 8-connectivity (right).*

The "bwtraceboundary (BW,P_0, FSTEP,CONN)" function detects the boundary of an image in a specified area window, where, in this work, the image is the top view circle of the specified pillars. Because the defined window regions as depicted in Fig 5.4 consist of both the pillar and some part of the worm's body (i.e. the circle is partially overlapping with the worm body), the number of the tracing points has to be manually defined in order to avoid the tracking of the worm's body (as indicated in Fig. 5.6), as this can lead to inaccuracy in the pillar tracking. Ideally this value should be chosen in a way not to track over the overlapped area of the worm's body, as well as detecting as many points on the circle as possible.

To find the optimum number of tracing points, a pre-processing was conducted to detect the number of points that need to be considered so that the circle outline fits the pillar tracking accurately. The image shown in each frame consists of thousands of pixels, arranged in rows and columns. Basically, the tracing points are acquired by counting the number of pixels of the tracked pillar area. Following the procedure similar to that introduced in [62], the number of tracing points is initially chosen and the algorithm is run to track the specified pillar area perimeter over each frame.

Then, the tracking on each frame is examined to compare the accuracy of the circular fitting on top of the deflected pillar. This procedure is repeated in an iterative fashion using a different number of tracing points until the outline of the circle fits the pillar top perfectly (or most closely as quantified by the pixel counts). From the conducted research, it has been observed that the number of tracing points that optimizes accuracy typically lies between 60 and 80. It is also important to note that this method must be repeated to evaluate the number of tracing points specifically for each new video that is post processed, and that the number of tracing points used for one video will not necessarily be the number that should be used for a different video.

In order to show the effect that the pixel count has on the estimation of deflection in a single frame, an illustrative example is provided in the following. A single image frame # 34 is considered and the pixel count of the pillar area perimeter which is not occluded by the worm's body in this frame is recorded as 66. Figure 5.7 shows an

outline of the pillar edge traced by 66 green points while Fig. 5.8 depicts an example of using 100 tracing points to track the pillar edge.

Having said that, it is also interesting to note the variation in pillar tracking based on the number of tracing points. It was found that this procedure is relatively insensitive to the number of tracing points used within the range of 55 to 75. To quantify the associated difference from the variation of the boundary tracing points, the center coordinates of the circular fitting when using the tracing points of 66 is determined. When the number of tracing points is varied from 30 to 100, there is a slight deviation of approximately 1.5% in the location of the circular fitting center coordinate. The percentage difference *(% diff)* is calculated using the equation below

$$\%diff = \frac{x - x_c}{x_c} \times 100\% \tag{5.3.2}$$

where x equals the calculated center coordinate from the variation of the number of tracing point, and x_c is the center coordinate of the pillar circle with the tracing points value of 66. The plot in Fig. 5.9 shows the divergence obtained from the center coordinate of the fitted circle of the deflected pillar with respect to the optimum number of boundary tracing points applied in the tracking algorithm. It can be concluded that an insufficient number of tracking points will lead to inaccuracy of the final fitted circle on the tracked deflected pillar. Likewise, choosing to use too many tracking points will track an area that includes portions of the worm's body, hence resulting in incorrect pillar circle fitting (see Fig. 5.8).

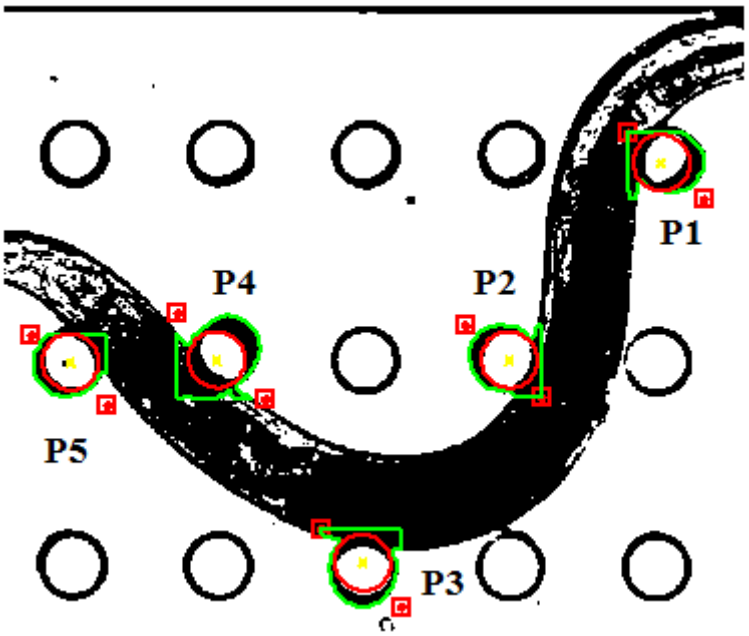

Figure 5.6: *Tracking of an image in a specified window (red markers) without defining tracing points (green trace) can lead to inaccurate fitting of the red circle on top of the pillar.*

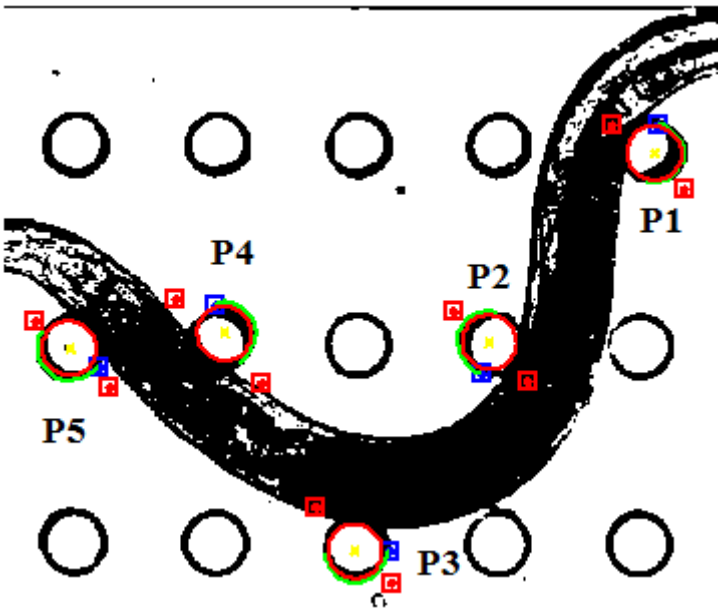

Figure 5.7: *Tracking of the pillar curve boundary using specified tracing points i.e. 66 results in the best (or most closely) circle fitting the top of the pillar. The starting point of tracing pixel, P_0 is indicated by the blue square marker at the edge the outer pillar circle.*

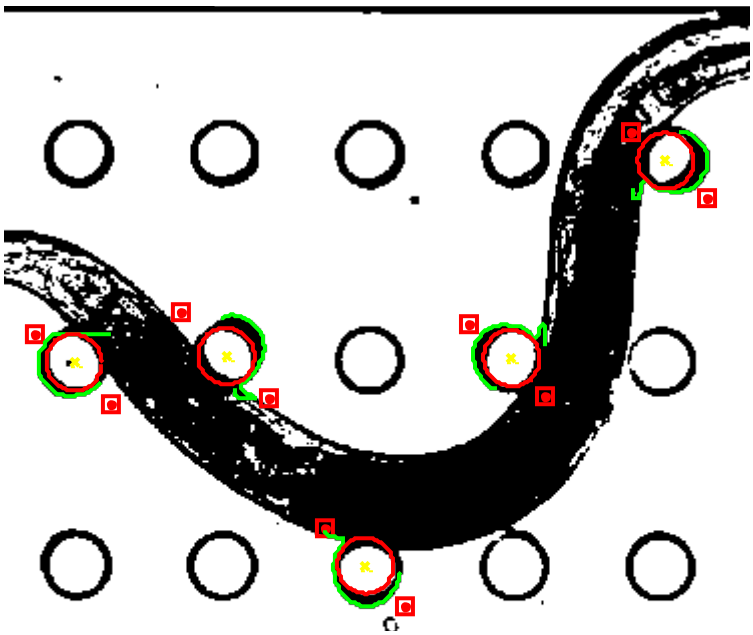

Figure 5.8: *Overly defined tracing points of 100 will track the portions of the worm's body, resulting in inaccurate circular fitting on top of the pillar.*

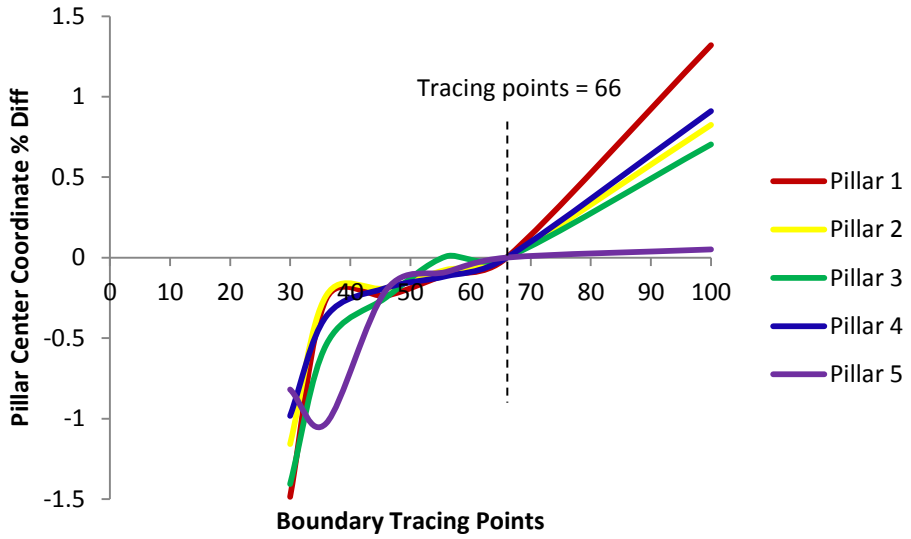

Figure 5.9: *Plot of the quantified percentage difference with respect to the pillar center coordinates of tracing points = 66 for all five pillars for frame # 34 shown in Fig. 5.11.*

Once the outline of a pillar has been completely traced, a least-squares fitting algorithm, as described in Section 3.8, can be employed to fit each of the pillar circles. Consequently, the center coordinates of each pillar and its radius were also determined, as depicted in Fig 5.10, with the original image to its left. Each pillar was fitted with a different color outlining the circular fittings for easier identification during post-processing, with its coordinate defined at the upper left part of the image.

Throughout the post-processing, each image frame was processed so that the every change from the top view of the deflected pillars was tracked accurately. This includes the center coordinates of each circle, where the values were displayed within the same window frame. Table 5.1 summarizes the algorithm used during post-processing of the micropillars for *C. elegans* locomotion force measurement.

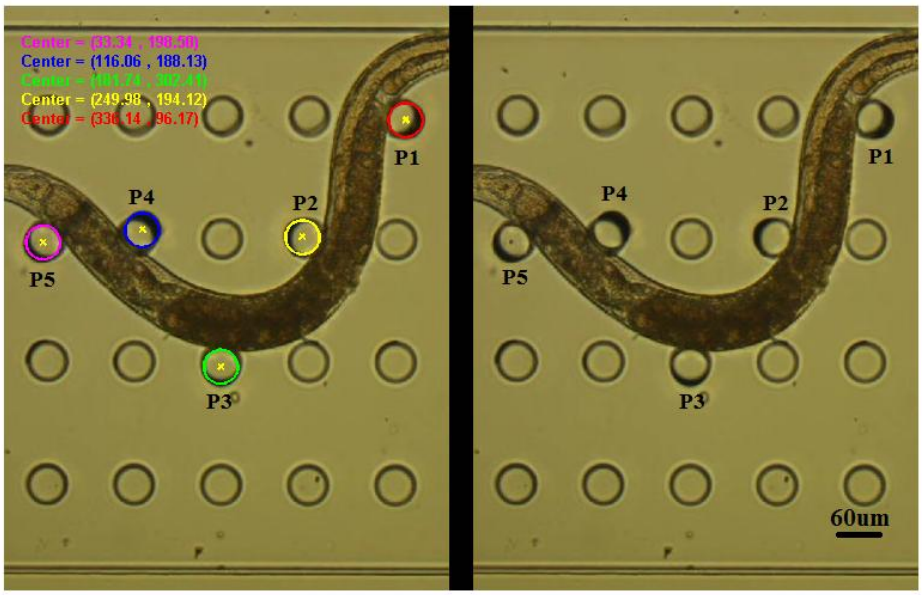

Figure 5.10: *Five selected pillars fitted with the circular fitting on the pillar surface (left) and the original image (right).*

Table 5.1: *Summary of image processing algorithm.*

Step	Description
Read image	Read original image, crop image for specific window containing selected pillars
Threshold the image	Convert image to binary (black and white) Determine coordinates of the area windows for the selected pillars
bwtraceboundary	Specify the starting point for the boundary tracing process
Trace the boundaries	Trace the pillar boundaries based on defined tracing points number
Circular fitting on the boundary	Using least-square fitting algorithm in Section 3.8 to fit each of the pillar circle
Deflection measurement	Based on the displacement of the pillar circle center with respect to its neutral position where the load is zero
Force calculation	Equation (3.2.7) is used to calculate the force

5.4 Analysis and Interpretation of Force Magnitudes

This section describes the interpretation of the post-processed data from the perspective of force analysis. In essence, the deflection of each of the five pillars measured during post-processing is translated into a force magnitude. In order to accomplish this, when the tracking of the pillar deflection using image processing was completed, the calculated displacement of each pillar was substituted into the pillar mechanics model (see Equation (3.2.7)). Consequently, the imposed force corresponding to each image frame exerted by the worm during the motion recorded was calculated and displayed. The calculated displacement using Equation (3.2.6) and the force magnitude for each pillar during 60 frames is illustrated in Fig. 5.11. Following that, Fig. 5.12 shows all 60 frames of image sequences from the recorded video with the visual tracking of five selected pillars.

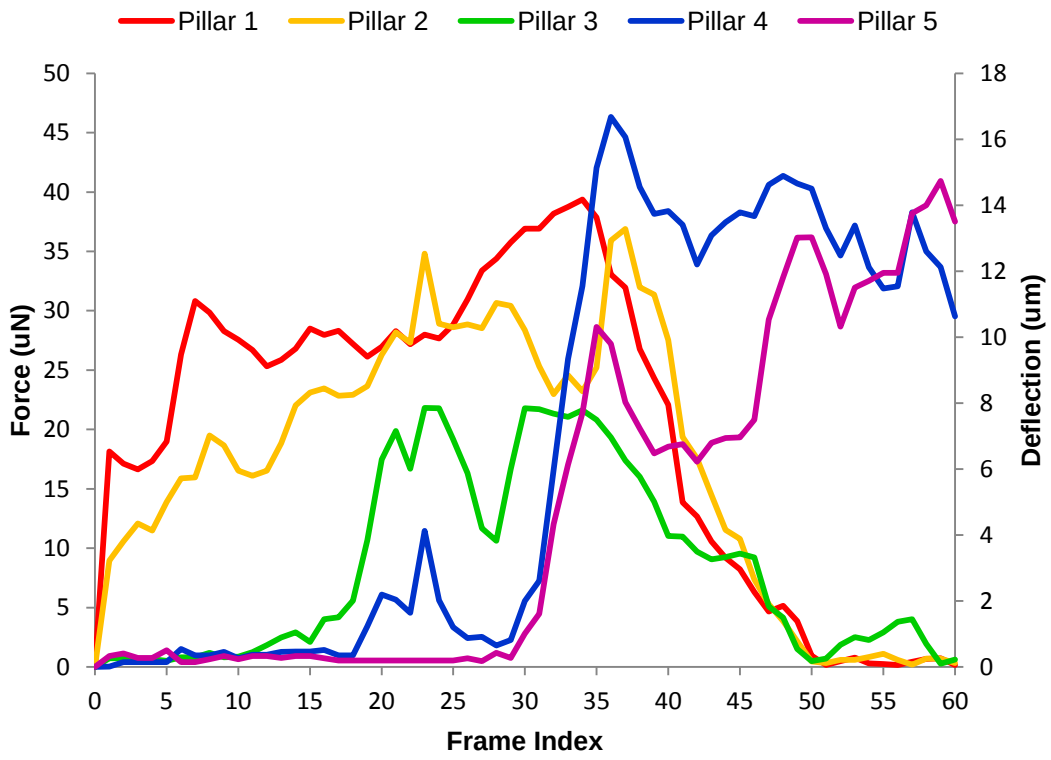

Figure 5.11: *The calculated equivalent force magnitude and visually measured pillar deflection exerted by* C. elegans *forward locomotion on five pillars of interest (P1 to P5) in all 60 successive image frames.*

Figure 5.12: *Total 60 image frames (F1 to F60) extracted from the captured video with the deflection of the selected five pillars being visually tracked in each frame. (Chronological order, starting left row top to bottom).*

During the course of motion, different body segments of the worm from head to tail are in contact with the five different pillars. It is anticipated that these segments do not exert equal magnitudes of force on the pillars over time. The results presented here should help in understanding the relative differences in the forces exerted by these different muscles. In order to interpret and justify the findings from the collected data, the basic anatomy of the nematode *C. elegans* is explained subsequently.

Figure 5.13 illustrates the basic features of the nematode *C. elegans*, where it consists of a cylindrical body shape with tapered head and tail. The worm's body is divided into four planes which are the anterior, posterior, dorsal and ventral. The simple anatomy of *C. elegans* contains a small number of tissues and internal organs which include the pharynx, intestine, and vulva to name just a few [86]. The outer shell of the worm cuticle contains the body wall muscles, which consist of 95 muscle cells arranged in four quadrants along the length of the worm body.

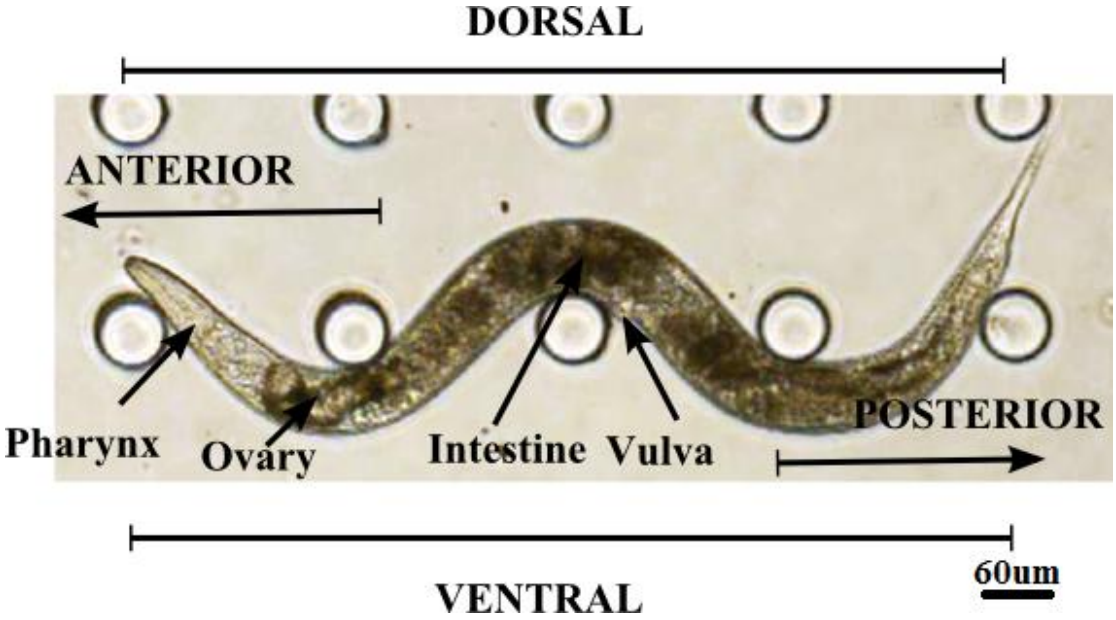

Figure 5.13: *Micrograph indicating the basic anatomy of an adult wild type* C. elegans. *Adapted from Tavernarakis and Driscoll [87].*

Each muscle typically has three to five muscle arms, which act as pathways for the muscles to receive stimulation from the nerve [9]. The coupling between the muscles and the outer cuticle of the worm's body will induce the contraction of the dorsal-ventral part that leads to the generation of sinusoidal waves which propagate along the

body length [88]. These dorsal-ventral muscles push the worm against its surrounding thus generating force thrust and enabling locomotion.

During the experiments, these different muscle groups exert forces on the five individual pillars that were in contact with the worm throughout the movement. The distribution of the selected pillars depends highly on the worm adaptability to its environment which is indicated by its sinusoidal body amplitude and wavelength during motion. The five individual pillars are positioned in the matrix composed of the three rows and five column pillar arrays. Pillar 1 and 3 were located in the first and third row accordingly while the remaining three pillars, namely pillar 2, 4 and 5 are located in the second row (see Fig. 5.14).

Initially, the worm made contact with pillars 1 and 2 using the anterior part of its body (above its pharynx), with forces of 18.14 and 8.94 μN respectively (see Fig. 5.11 and Fig. 5.14). The force was calculated based on Equation (3.2.7) described in Section 3.3. Because of the shape of the worm body above its pharynx is tapered (not fully cylindrical), it is anticipated that the worm-pillar contact at this position is not at the pillar half height, as discussed in Section 3.3 (see Fig. 3.5). Thus, the calculated equivalent force can be subjected to 20% to -40% variations in its value. As the nematode continues to move, the force on pillar 1 decreases by 1 μN in each frame until it changes its head movement during frame # 3, causing the force to continue rising to 30.8 μN at frame # 7. At this stage, pillar 1 was in contact with the intestine area of the worm body, which is slightly bigger in dimension than its tapered head in the anterior part of its body. The exerted force decreases again from frame # 8 up to frame # 12. It is suspected that the longer distance that the worm's body travels between successive frames caused this reduction in locally exerted force.

From frame # 13 to #18 (see Fig. 5.14), the exploratory behaviour of the worm was obvious through its head movement, where it examined its surrounding path before deciding on the next course of motion. During this period, the force exerted is in the range of 25 μN to 28 μN and it dropped to 26 μN when the worm changed its direction at frame # 19. Up to this point, the generated force pattern on pillar 2 is similar to pillar 1; the force on pillar 2 is 37 to 56% lower than the force applied on

pillar 1. It can be hypothesized that the anterior part of the worm body which includes its slightly smaller tapered head generates lower force during motion compared to the middle part of the nematode. This can be further reinforced by the lower force (1 to 6 μN) generated on pillar 3 by the worm's pharynx located at the anterior region starting from frame # 12 to # 18.

When the worm changed its direction at frame # 19, it pushed against pillar 3 using its ventral body part near the intestines area. This caused the force applied on pillar 3 to rise up to 21.8 μN. From here, the force patterns generated on pillar 2, 3 and 4 are similar in the way that they increased gradually until they dropped at frame # 22 before increasing again during the next frame. This particular force pattern was due to the worm tilting its head back at frame # 23, which caused the squeezing of its body against all three pillars and concurrently generated bigger force.

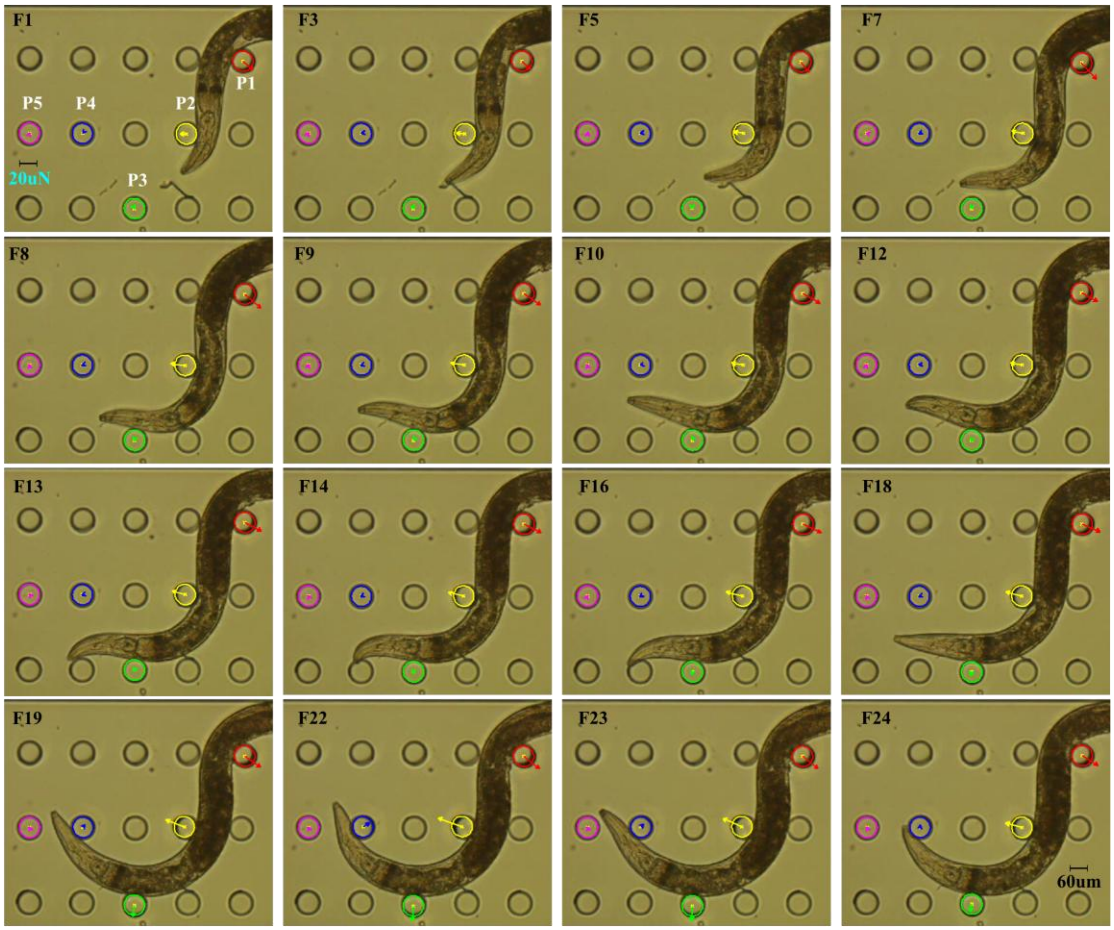

Figure 5.14: *The first half of the worm movement. Image sequences of the recorded worm motion depicted by selected frame from 1 to 24.*

The worm body position during this period of motion shows the anterior part of its body (pharynx) in contact with pillar 4 (11.50 μN) followed by pillar 3 (21.81 μN), while the posterior part is in contact with pillar 2 (34.81 μN). The differences in the force values exerted at different regions of the worm's anatomy strengthens the findings that the body wall muscle in the posterior part generates relatively high forces compared to the anterior part of the worm body. This, to the author's knowledge, has never been reported before.

The worm then changes its head direction again during the next frame (# 24), causing the exerted force on all three pillars to drop. From this frame onwards (see Fig. 5.15), the worm exhibited force in the range of 28.9 μN to 30.7 μN on pillar 2 until it dropped by 3 μN when reaching frame # 31. For pillar 3 and 4, the generated force dropped further by approximately 10 μN when it reached frame # 28.

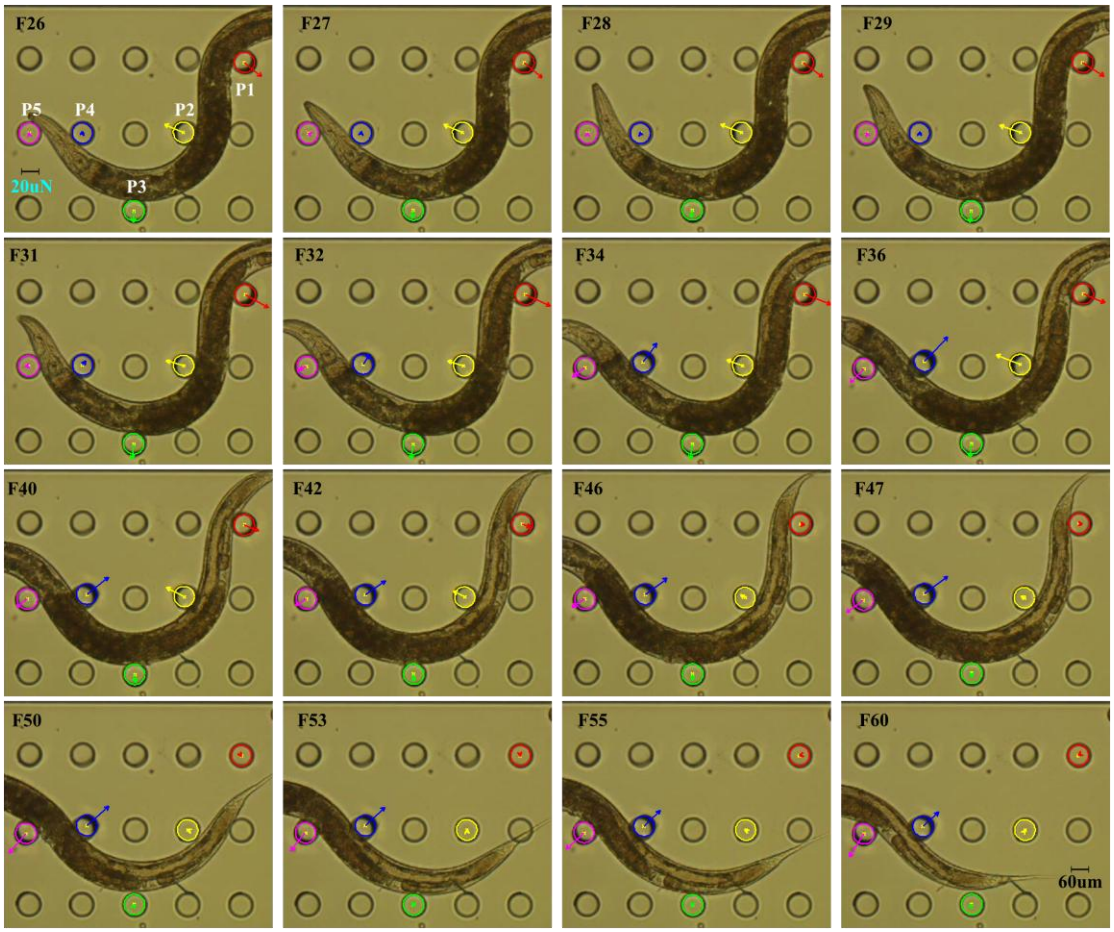

Figure 5.15: *The final half of the worm movement showcasing selected image frames from frame 26 to the final frame number 60.*

As the nematode changed its head direction again at frame # 29, it started to move its body in between pillars 4 and 5 and this caused the exerted force on pillars 3, 4 and 5 to increase rapidly until it reached frame # 36, while the force exerted on pillar 2 decreases from 30.4 μN to 23 μN at frame # 32. At the same time, the force applied by the worm on pillar 1 during this period fluctuates between 26 μN to 28 μN.

While the worm continued moving forward, pillar 1 is now in contact with the posterior part of the worm body, and the force exerted on pillar 1 continues to rise steadily to 38 μN when it reached frame # 33. When the worm moves toward pillars 4 and 5, the force exerted on pillars 1 and 2 starts to decrease until they no longer make contact with worm body. This is evident in the force plot (see Fig. 5.11) where between frame # 30 to 50, pillar 4 and 5 show an increasing force pattern while the force on pillar 1 and 2 starts to decline.

As the worm glides along, its body movement forms a half-wave change in the shape of its body, hence contributing towards the propulsive thrust in between pillar 5 and 4. This results in the generated force increasing to 28 μN on pillar 5 and the maximum force of 46 μN applied on pillar 4 when the worm hits frame # 36. The worm continues to move in-between pillars 4 and 5 and simultaneously generates similar force patterns on both pillars until it adjusts its head again at frame # 42, causing a similar pattern of lower exerted force on both pillars. The similarity of the force exerted on these two pillars during the worm's motion until the end can be seen in the force plot, with force on pillar 4 being approximately 40% higher than the force exerted on pillar 5.

Throughout the entire recorded locomotion, the worm moved its body in between pillars 1 and 2 and also pillars 4 and 5. At the same time, the ventral part of the worm body is in contact with pillar 3. The force exerted when moving in the narrow spacing between two adjacent pillars in horizontal axis is higher compared to wider spacing in the vertical axis where pillar 3 is located and is apparent in the plotted force generated on pillar 3. The variation of the generated force with respect to the pillar spacing and arrangement will be explained in the next chapter.

As discussed previously, the generated force on all five pillars at every image frame can be observed in Fig. 5.11. The x- axis in Fig. 5.11 indicates the frame index while the y- axis demonstrates the applied force magnitude on five selected individual pillars. The maximum force generated was on pillar 4 during frame # 36, with the

value of 46.3 μN. Since the locations of the five pillars are distributed along the nematode body length, the similarity of the force pattern generated on pillars 1 and 2, and also on pillars 3 and 4 can be associated with the sinusoidal body shape of the nematode. For instance, the force pattern applied on pillars 1 and 2 during frame # 5 to # 35 is accumulated around the middle section of the worm body, and this is followed by a similar pattern of the force exerted on pillar 4 and 5 during the second half of the recorded locomotion from frame # 35 to # 60 as indicated in Fig. 5.11.

The location of the cylindrical shape of the worm's body in between two adjacent pillars, pillars 4 and 5 also provides information on the force exerted from the body wall muscles located in the dorsal and ventral plane of the worm. The force vector can be visualized from the tracked pillar deflection during image processing (see Fig. 5.16). Aside from that, Fig. 5.17 shows the force measurements with both magnitude and direction information, which renders the system suitable for constantly tracking the continuous force trends in *C. elegans* continuous motion over any period of time.

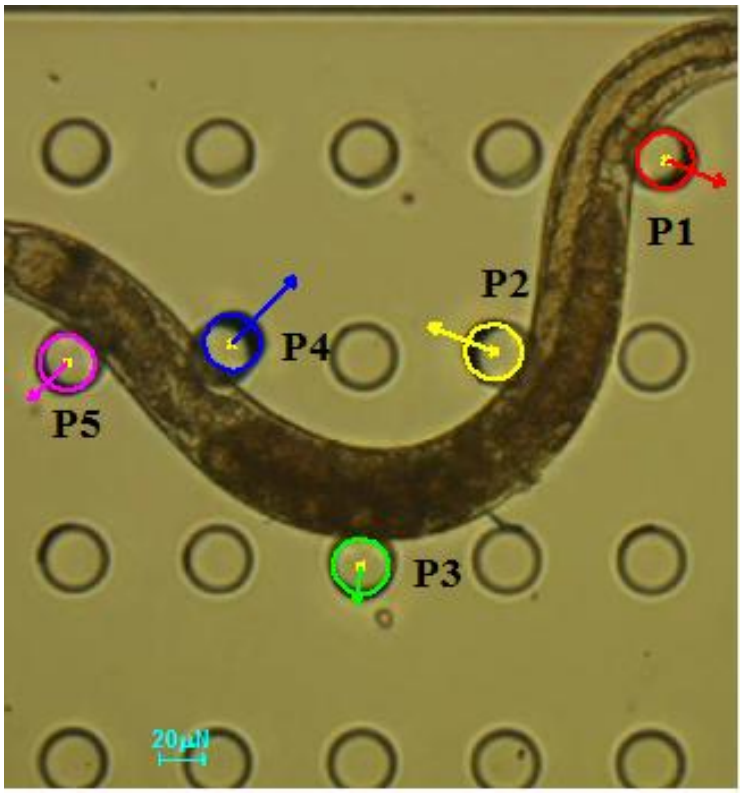

Figure 5.16: *The force vectors of the deflected pillars visualized during image processing.*

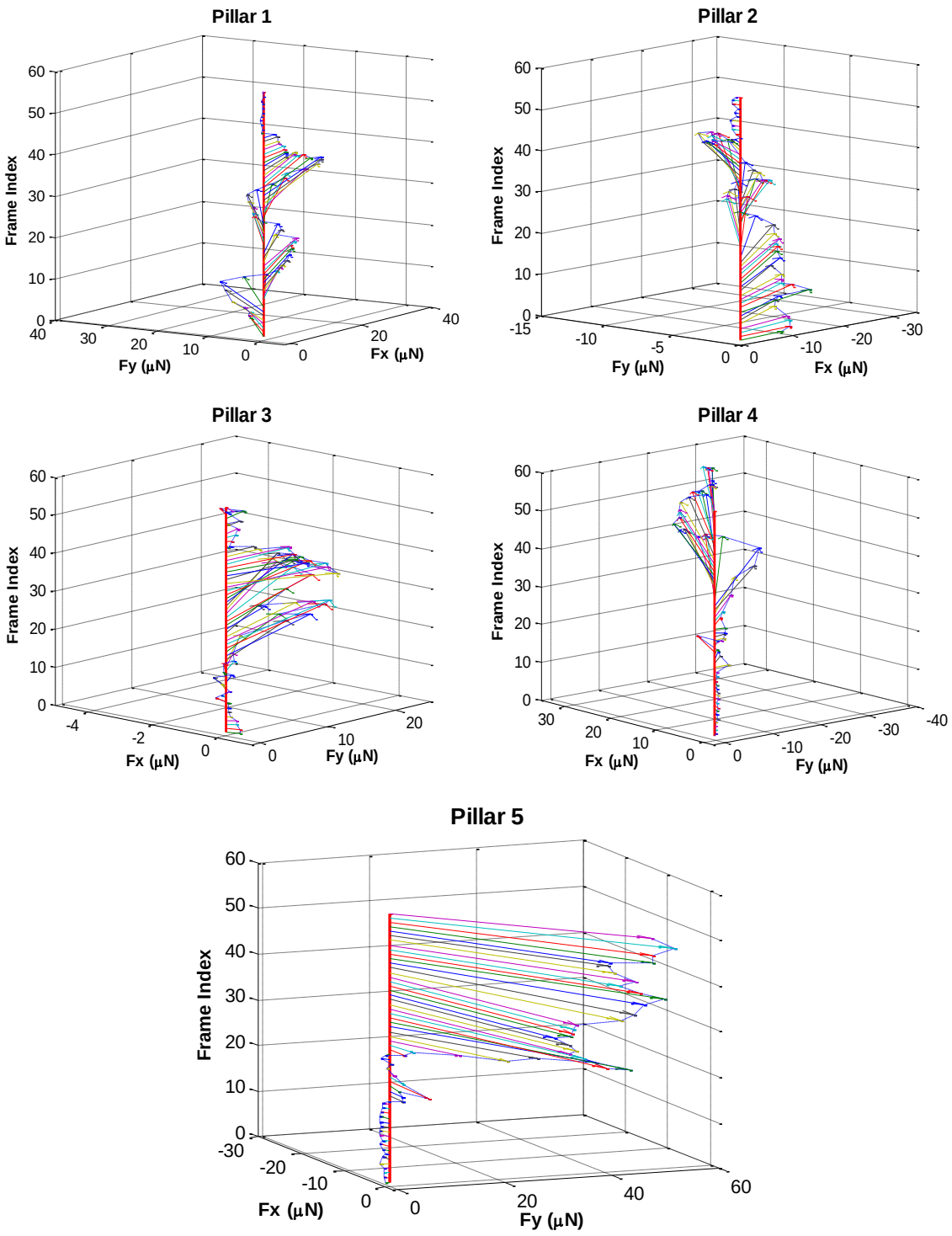

Figure 5.17: *Force measurement results with magnitude and direction for five selected pillars over 60 frames.*

The discussion on the force magnitudes collected during post-processing is supported with an additional set of locomotion recorded in a different video. This section provides details on the physical interpretation of the force data, where the recorded video consists of both forward and reverse motion of a *C. elegans* using device Design 2.

Although the subject of *C. elegans* biology is not the main focus of this study, the experimental force data collected from the worm locomotion does fall into place and is biologically relevant with the justification made in this section later on.

The recorded video contains worm movement for the duration of 11 s and was then converted into 55 frame images. Six pillars were in contact with the worm during this motion, with pillars 1, 2, 3 and 4 located next to each other were chosen because they were in contact with the worm's body during forward motion, and pillars 5 and 6 in contact with the worm's body while the worm is moving backwards.

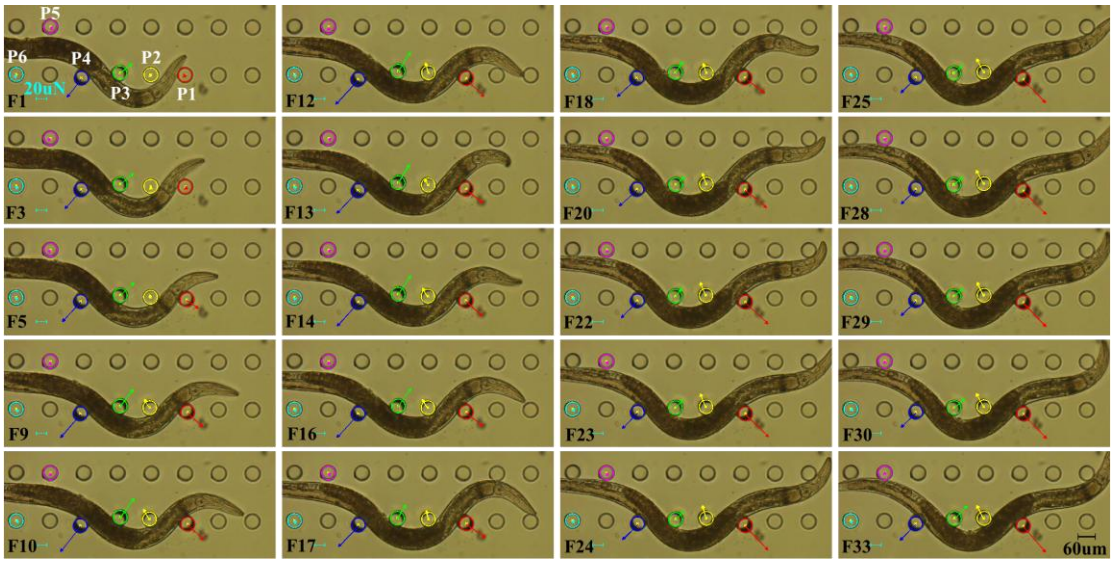

Figure 5.18: *Image sequences selected from frame 1 to 33 of worm movement in between 6 measurement pillars. The force vector can be visualized on top of the tracked pillar surface.*

The locomotion started with the front half-wave of the worm body gliding between pillars 3 and 4 producing the force of 34 μN and 49 μN respectively at the beginning

in the ovary area (see Fig. 5.18). This is followed by contact made on pillars 1 and 2 using its head, which produced a force of 7 μN during the fourth frame. The exerted forces on all four pillars increase rapidly by approximately 20 μN, aside from pillar 1 which experienced an increase in force of up to 50 μN.

The undulation of the worm body exhibits a train of waves which moves relative to its head. The rapid changes of the worm's head caused the force exerted on pillars 3 and 4 to decline by 28 μN and 21 μN in that order until the posterior part of the worm reaches frame # 30. In contrast, the force on pillar 1 and 2 decreased just by 5 μN with respect to the worm's head movement during frame # 11 until frame # 16. The large displacement of the worm's body part when moving between successive frames was obvious at frame # 17. From here, the applied force on pillar 1 (48 μN) and pillar 2 (25 μN) keeps increasing to 69 μN and 41 μN, respectively when reaching frame # 24. The motion from frame 25 onwards generated almost constant forces on these two pillars until the sequence reaches frame # 39.

The worm started to reverse its motion very slowly from frame #36 to # 39 (see Fig. 5.19). During frame # 40, the reverse motion combined with the change of its head movement started to make contact and exhibited forces on pillar 5, and at the same time increased the exerted force on pillars 1, 4 and 5 upon arriving at frame # 42. The maximum force exerted was during this particular frame on pillar 1, at the value of 78.8 μN. The effect of the worm moving its head in reverse is obvious afterwards as all generated forces started to decrease during the next frame. When the worm continues moving backwards, its body started to make contact with pillar 5 and 6 which in return generated forces of 30 μN on both pillars. The force pattern exerted on pillar 5 and 6 are similar until the end of the worm motion at the final frame.

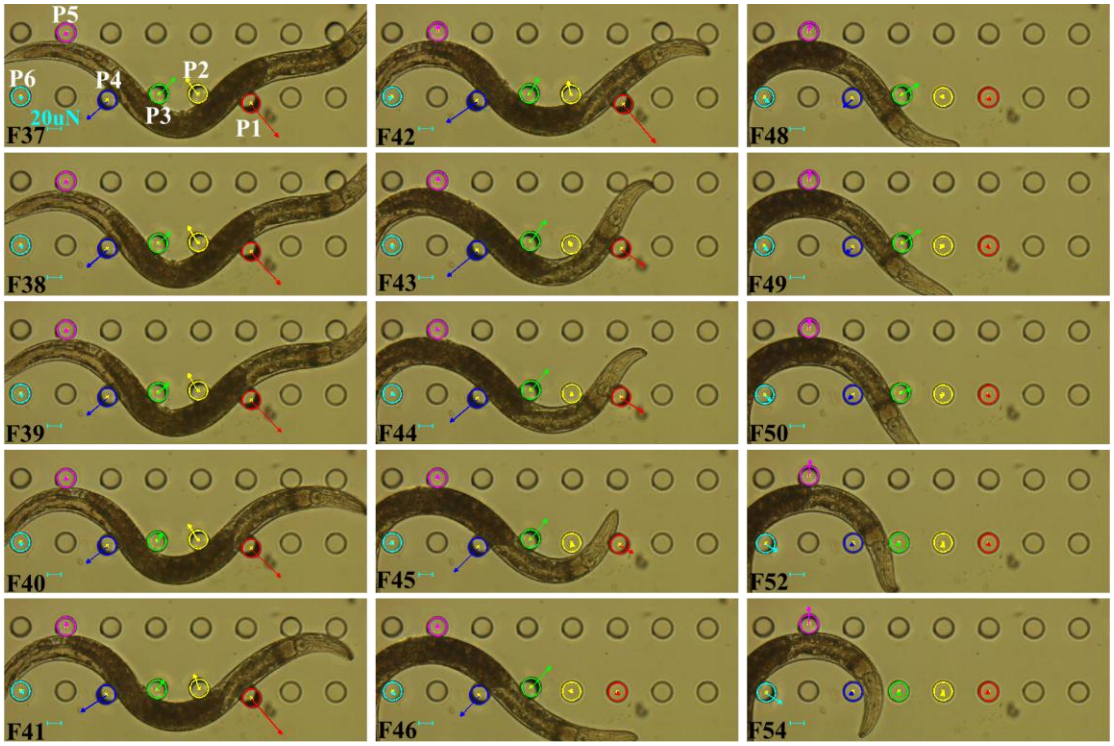

Figure 5.19: *Selected micrograph sequences illustrating nematode body contact with the measurement pillars.*

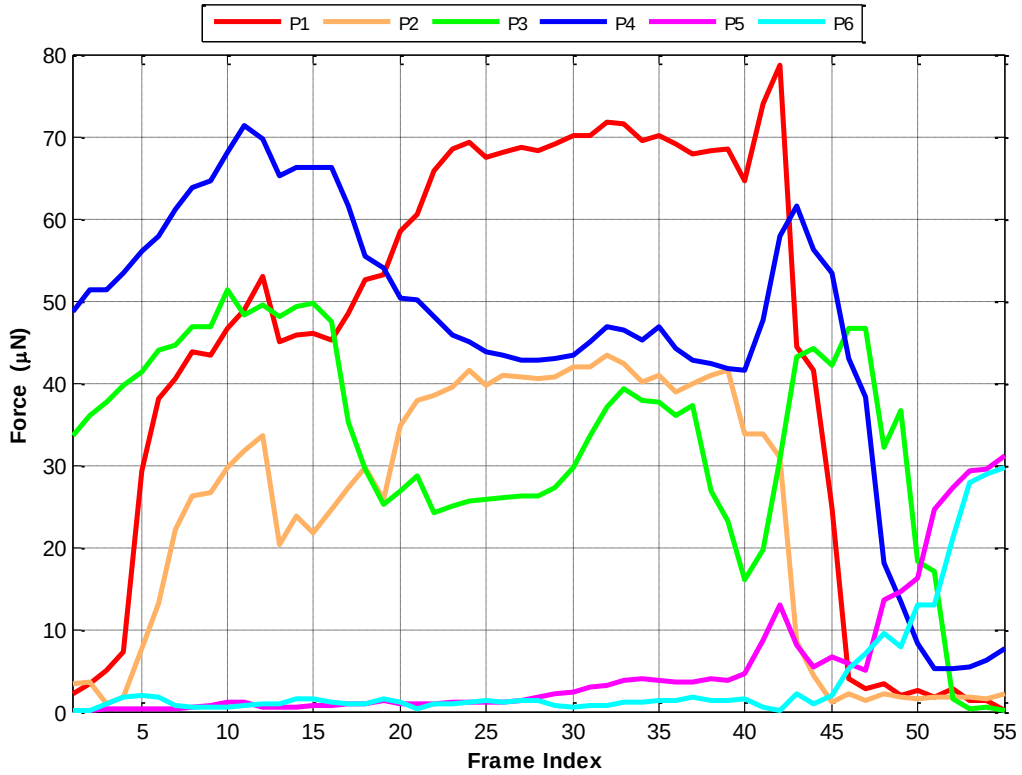

Figure 5.20: *Plot of the force magnitude measured on six pillars for a sample worm for a period of 5 s. Some representative image frames corresponding to this force plot are shown in Fig. 5.18 and Fig. 5.19.*

The force magnitude of the worm motion on six different pillars of interest is depicted in Fig. 5.20. The reverse motion of the nematode obviously affected its body movement as the generated force on all pillars show a decreasing pattern during frame # 40. Since the position of the sinusoidal body shape of the worm is between pillar 1, 2, 3 and 4, the internal bending couples that change the curvature of each region of the worm's body when gliding in between all these pillars can also be investigated from the information obtained by the generated force.

For local force variation (i.e. curve not being very smooth) observed in the plot in Fig. 5.20, Doll et al. [54] recorded even stronger oscillating forces. These were accredited to sudden changes in worm locomotion patterns, such as sudden acceleration or change of direction, which were observed their experiment.

Initial experiments have also been performed to collect a maximum force level for *C. elegans* in motion. Thirteen worm samples were used with each recorded for 30 frames during which the worm moved actively (e.g. forward, or reverse). For each sample, three to five pillars that had most deflections over the imaging time were processed to retrieve the force levels. Figure 5.21 plots the maximum force levels on these pillars for each worm. The maximum force level observed in any experiment was 61.94 μN (based on 1571 data points in total) and the average maximum force level was 32.61 μN. This was different from the reported force value in [54] which was less than10 μN.

However Doll et al. [54] measured the force for a series of brief worm nose touches and body wrapping around the SU-8 pillar free end, with each contact event less than 500 ms. By contrast, the force measurement provided here was when the worm body was actively moving and thus continuously contacting pillars for 5 s and more. This suggests the different worm activities and worm body parts in contact with sensing elements are reasons for the measurement difference. It was also observed from Fig. 5.21 that the maximum force levels varied across multiple contact pillars for an individual worm sample. The reason is currently unknown but probably related to the mechanism of how the worm adjusts its body to interact with the structure of its environment.

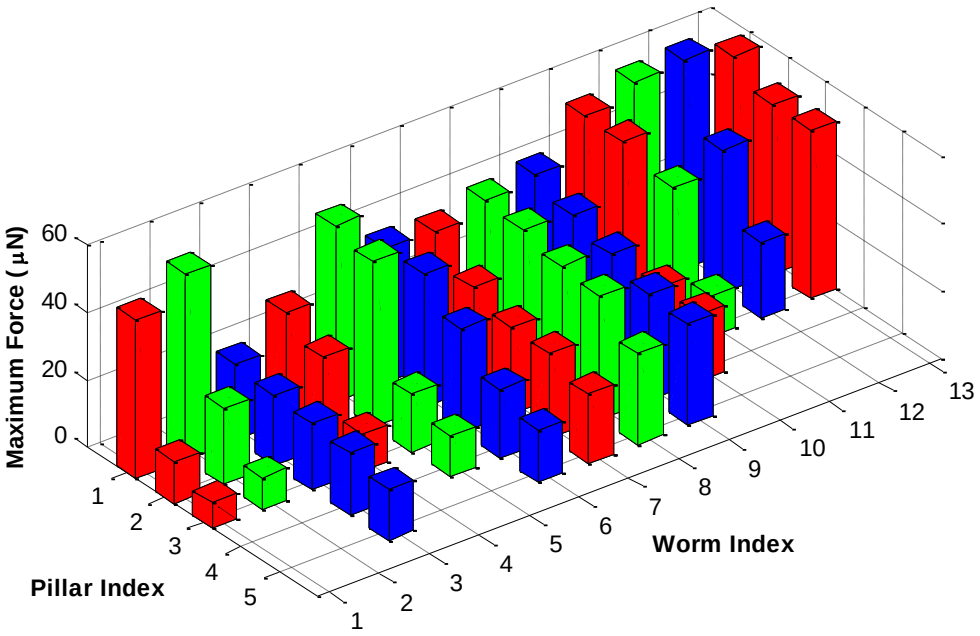

***Figure 5.21**: Maximum forces measured for thirteen* C. elegans *samples. Average maximum force was 32.61 μN. Note the force magnitudes for each sample were sorted then plotted for better visualization.*

5.5 Remarks on Force Data

In general, several important points can be made from the force pattern obtained using the proposed PDMS device. The first interesting observation was regarding the maximum generated force on the measurement pillar. It was found that, on both occasions of forward and reverse locomotion, the maximum force is typically associated to the pillar being in contact with the intestine area of the worm's body. This finding agrees with theoretical analysis [5], which states that when crawling *C. elegans* concentrates most of its bending force around the middle part of its body.

During locomotion, the *C. elegans* body exhibits a train of waves which move relative to its head, which means that the generated waves along the body length depend on the movement of the worm's head. This can be observed by the variation of the generated force pattern that occurs whenever the worm moves its head to change its movement direction. In addition, there were also a few occasions when the worm only

moves its head instead of its whole body. This can be referred as the exploratory behaviour where the worm surveys its surrounding environment before deciding on the next course of action. During this period, the generated force is generally constant, with minor fluctuations of 1 to 2 μN.

Although the primary focus of this research is not intended to provide a detailed analysis of *C. elegans* locomotion from a biological perspective, the findings observed from these two particular locomotion types strongly indicate that the device Design 2 can be used as a platform on which to study the detailed underlying physics of *C. elegans* locomotion. The average generated force during the forward motion was 15.7 μN while the combination of the forward and reverse motion contributed to an average force of 25.9 μN. Apart from the dissimilarity of the motion behaviour, the changes in the *C. elegans* body amplitude and wavelength during the first and second recorded motion obviously were the contributing factors. This can be supported by Gray [89], which indicates that the magnitude of *C. elegans* propulsive thrust relies upon the magnitude of the bending couples induced within the worm's body and the shape of the sinusoidal wave of the worm. Two important indicators of the worm's body form are its sinusoidal body amplitude and wavelength during motion. Detailed analysis regarding the relationship of the force generated during propulsive thrust and the shape of the sinusoidal body waveform will be discussed in the next chapter.

The force measurement results discussed in this chapter are subjected to a few potential sources of error obtained from the proposed method of the PDMS device. The assumption that the PDMS pillars are perfectly uniform along the post height can be resolved during the visual inspection of the measurement pillars using SEM. The assumptions that the worm-pillar contact forces are purely in-plane and concentrated at half of the pillar height have been discussed in Chapter 3. This also includes the drag forces applied by the moisturized environment that were determined to be at a force magnitude of 10^{-13} N using the fluidic drag model.

Since *C. elegans* is a genetically amendable organism, mutated worms with different numbers of muscles arms can be obtained. According to Wang et al. [90], a positive relationship exists between the number of muscle arms and the amplitude of the

waves that *C. elegans* exhibit during locomotion. The collected force pattern information from the proposed device could help establish the relationship between muscle arms and force patterns of *C. elegans* in motion, and thus give a better understanding of the genetics controlling muscle arm development.

5.6 Summary

The complete experimental setup of the PDMS force measurement device has been discussed in section 5.1 of this chapter. The simplicity of the setup, which only requires an off the shelf regular digital camera and the PDMS device, could be readily accessible to most worm laboratories. The criteria for choosing the appropriate measurement pillars have also been reviewed. Following that, the detailed method of how to measure the pillar displacement during post-processing using a custom image processing algorithm was discussed extensively. In order to investigate the typical locomotion behaviour of *C. elegans*, two sets of recorded video of worm locomotion inside device Design 2 were analyzed. For both sets of locomotion, the force magnitude and direction were obtained and the distinctive force pattern generated during the reverse motion in the second recorded video was easily noticeable from the resulted plot. The information from the force pattern exhibited by the worm during motion can also be used to identify the related worm body segments that were responsible for producing that certain amount of force. The experimental results demonstrate the efficacy of force measurement, leading to three preliminary but interesting findings on force patterns related to locomotion. These are:

(i) The generated force depends on the worm's head motion in particular when changing its movement direction

(ii) The worm sinusoidal body shape affects the exhibited force pattern

(iii) The mid-body of the worm generates the maximum force level as predicted by theoretical analysis.

These results agree with the findings of other studies [5, 89] and the provided features will hopefully enable further investigation of the theory behind the worm locomotion forces.

CHAPTER 6

Locomotion Forces for Different Microstructure Patterns

In Chapter 4, the design optimization of the PDMS device has been carefully considered with regards to the pillar arrangement and spacing in order to provide the best environment for force measurement experiment to succeed. In this chapter, the correlation between *C. elegans* locomotion forces and their environment is investigated by introducing variation into the microstructured pillar arrangement and spacing. Two different micropillar layouts were investigated, namely the *'Honeycomb'* and *'Lattice'* design structure with the spacing between micropillars for each design also varied. Prior to the introduction of the force measurement device presented here, relatively little work had been done to address the detailed analysis on *C. elegans* locomotion behaviour with regards to forces generated during motion and the measurement of other locomotion metrics. The transparency of the device introduced in this thesis can be used to determine the locomotion forces, amplitude, wavelength and velocity associated with *C. elegans* in the microstructured environment. In addition to the force measurement capability provided as described in Chapter 5, this chapter highlights the benefits of this device which allow one to take simultaneous measurements from multiple locations along the worm's body: a new development previously unavailable to the research community.

6.1 Overview

The main principle of the device is to be able to measure the variations of forces exerted by the worm during its movement. In order to contextualize the relative forces associated with the worm, the worm's general anatomy and its functions are first considered. The core of *C. elegans* mechanosensation and locomotion is centered within the body mechanics of the worm, which are regulated by their body wall muscles. As shown in Fig. 6.1, there are six touch receptors along the *C. elegans* body responsible for mechanosensation which are: ALML: Anterior lateral microtubule cell left; ALMR: Anterior lateral microtubule cell right; PLML: Posterior lateral microtubule cell left; PLMR: Posterior lateral microtubule cell right; AVM: Anterior ventral microtubule cell; PVM: Posterior ventral microtubule cell. These touch receptors are situated next to the body cuticle, which runs along the body wall muscles [91] and they are able to detect external forces applied to the body wall muscles and internal forces generated during locomotion.

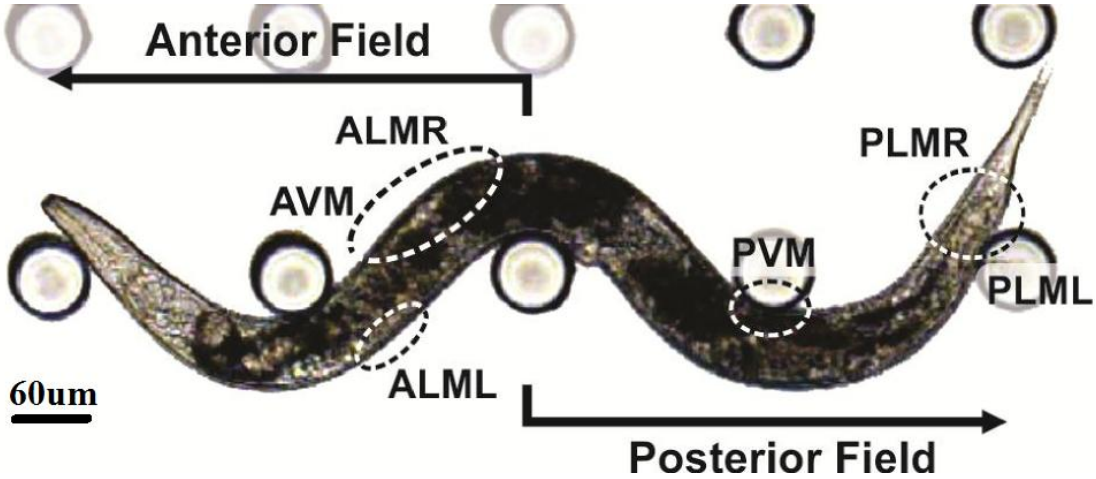

Figure 6.1: *Optical micrograph of* C. elegans *indicating the location of its touch receptor neurons [87].*

Recent advances in microfabrication technology and the adoption of microfluidic devices have made it possible to further investigate *C. elegans* phenotypic locomotive behaviour [26, 71]. Several microfluidics-based *C. elegans* assays have been developed, which include mazes and arrays to study worm learning and mobility

behaviour [28, 30, 32], clamps for *C. elegans* immobilization and imaging [42], an olfactory chip [92], and a droplet-based system for individual movement assays of the nematodes [29, 34]. Microfluidic devices have also been employed as research tools to study *C. elegans* locomotion patterns [25, 26]. The latter in particular are relevant to this work as they focused on studying the locomotion pattern of the nematode using microfabricated PDMS devices. In essence, a series of sinusoidal microchannels with varying amplitudes and wavelengths was used to match the worm sinusoidal movement and observe the worm's adaptability to the microchannel environment [39]. Their suggested methods can be used as a screening system for locomotion phenotypes. In a different work by Park et al.[37], it was found that by using microstructured short agar pillars the worm locomotion can be enhanced, particularly when the nematode wavelength matched the micropillar array periodicity.

Although these existing studies provide insights into *C. elegans* locomotion pattern and behaviour in microstructured environment, they still lack the capability of providing information regarding *C. elegans* force patterns during locomotion. One of the main advantages of the device proposed in this thesis is that it can measure multi-point forces for a worm sample of *C. elegans* in motion very quickly. Expanding upon the above concept, this chapter will investigate the correlation between *C. elegans* locomotion forces and their environment by introducing variation into the microstructured pillar arrangement and spacing.

The *C. elegans* locomotion phenotype can also be characterized using other locomotive metrics such as the locomotion velocity, body amplitude and the bending wavelength. The transparency of the proposed PDMS force measurement device can be used to simultaneously quantify the related locomotion parameters. Further evidence that the natural sinusoidal movement of *C. elegans* remains similar in the device, despite the existence of the PDMS micropillars will also be provided. The findings presented in this chapter provide further insight into the correlation between locomotion and the generated force patterns, thus demonstrating the utility of the device as an emerging technology for research regarding *C. elegans* mechanosensation and locomotion behaviour.

6.2 PDMS Micropillars Layout Structures

Based on Design 3 described in Section 4.1.2.3 (Fig. 4.3), the microfabricated device consists of a 9 x 9 mm square chamber with a matrix of PDMS pillars and a glass coverslip enclosing the top. Each pillar can be regarded as an individual cantilever beam which functions as a force-measuring unit dedicated to one individual *C. elegans*. At any given time a nematode will be in contact with 8 to 10 pillars, depending on worm size and pillar spacing. The pillar dimensions were set to be 100 μm height and 60 μm diameter. The chamber is enclosed by four sidewalls which are 20 μm higher than the pillar tips. This is to ensure that the glass coverslip does not touch the pillar tips when the pillars are deflected. In addition, it protects the worm and pillars from contamination. The front and rear faces of the test section are open and function as the worm loading and extraction zones. Two different pillar configurations were used in this work (see Fig. 6.2). The first arrangement is called the '*Honeycomb*' (HC) design, in which the pillars are arranged in a hexagonal formation (see Figs. 6.2(a) and 6.2(c)). The second arrangement is called the '*Lattice*' (LC) design, where the pillars are arranged in a square lattice grid structure (see Figs. 6.2(b) and 6.2(d)). These configurations were chosen as they mimic the worm's natural environment by providing an array of obstacles and have previously been used to investigate worm locomotion behaviours, as shown in the work published by [37, 38]. For both pillar configurations, there are two different layouts for each arrangement. The first uses a pillar centre-to-centre distance of 110 μm and the second is arranged with a spacing of 140 μm.

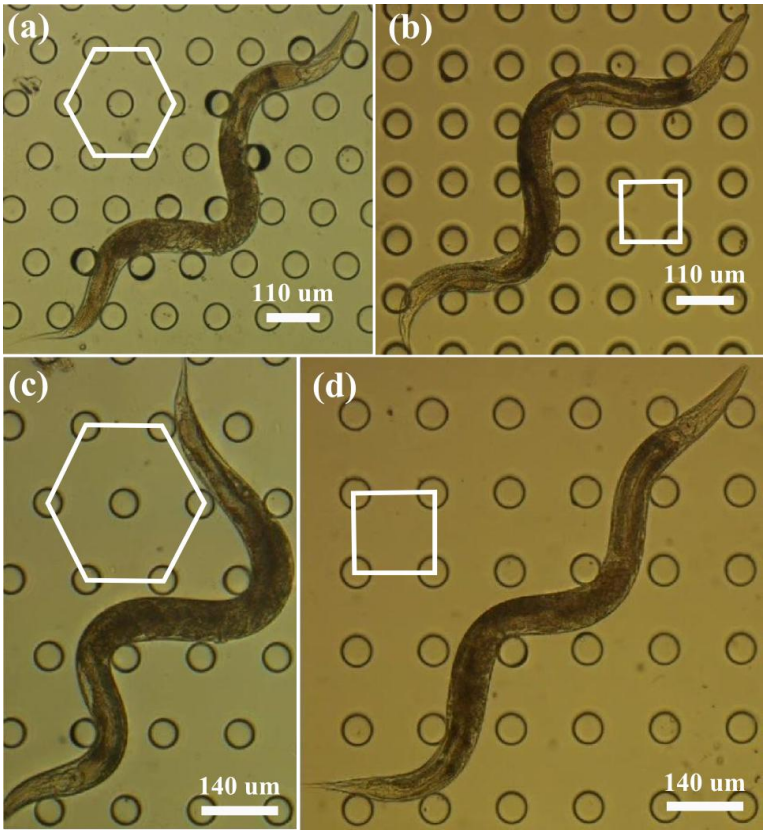

Figure 6.2: *PDMS micropillar configurations. (a) & (c) 'Honeycomb' (HC) design with pillar centre-to-centre distances of 110 μm and 140 μm, respectively. (b) & (d) 'Lattice' (LC) design with pillar centre-to-centre distances of 140 μm.*

The following sections will describe the forces generated by three wild-type *C. elegans* samples from adult stage in each of the designated pillar arrays. A single example is discussed in each case and the force pattern generated by each worm when moving inside the designated device was also analyzed. Through visual observation the worms were found to adapt to the new environment within the first five minutes as they continuously generated smooth crawling motion without major difficulty. During the course of motion observed, different body sections of the worm, from end to end, were in contact with the micropillars. This indicates that different body wall muscles are interacting with the environment. Note that in this work, only the pillars that were observed to experience the most deflection and were in contact with the worm's body throughout the entire recorded video were chosen for force measurement.

6.2.1 *'Honeycomb'* structure: 140 μm

Figure 6.3(a) shows the force pattern generated by a single worm using the *'Honeycomb'* design structure with a pillar centre-to-centre distance of 140 μm. The worm was observed to exhibit a constant sinusoidal movement pattern which was in contact with six different pillars (pillar 1 to pillar 6) during the movement excerpt of 11 s (55 frames) shown here. During the first second of observation, pillars 4 and 5, which were in contact with the worm's middle section, experienced the greatest force (see Fig. 6.3(b)). Similar to the findings reported in Section 5.4, this maximum force acting on the pillars that are in contact with the worm's central region can be observed throughout the worm's range of motion. This implication is in strong agreement with the theoretical analysis reported by Shen et al.[5], which stated that *C. elegans* concentrates most of its bending forces around the middle part of its body, especially when crawling.

The sinusoidal shape generated by the worm body is split into two parts: the anterior field and the posterior field. From the force plot, it can be seen that the distributed force is not equal or symmetrical along the worm body length. The posterior field was observed to exert greater locomotion force compared to the anterior field. It can be verified that continuous force levels were produced by the worms in motion, which is in accordance with the biological anatomy of *C. elegans*.

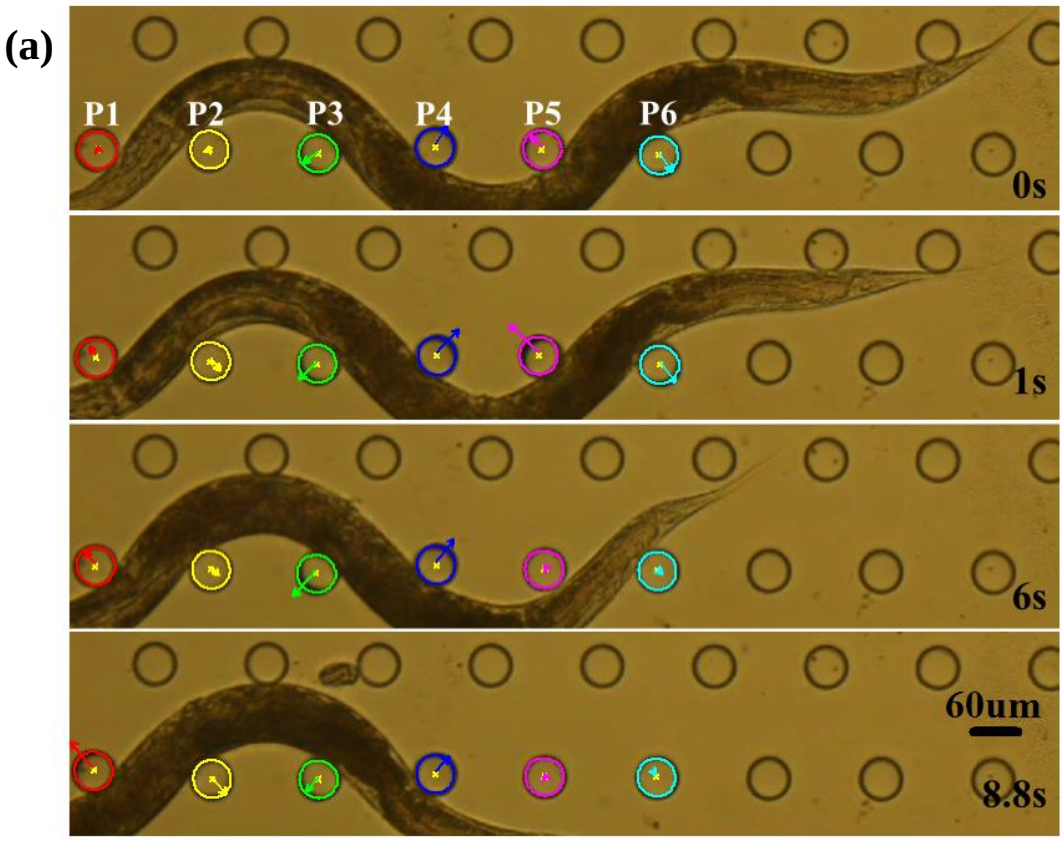

Figure 6.3: *(a) Image sequence of* C. elegans *motion in 'Honeycomb' design with a pillar centre-to-centre distance of 140 µm. Elapsed time (s) is indicated on the lower right of each frame. The worm is in contact with 6 different measurement pillars with the middle part of the body outlined. (b) The associated force magnitude generated on each of the pillars in the anterior and posterior field.*

6.2.2 *'Lattice'* structure: 140 μm

The force pattern generated using the *'Lattice'* design structure with the same pillar centre-to-centre distance of 140 μm was then investigated, as depicted in Fig. 6.4. It was found that the maximum force was also exerted when the pillars were in contact with the middle part of the worm body. The average generated force is 40% lower when moving inside the *'Lattice'* structure with a maximum force of 18.86 μN compared to the *'Honeycomb'* design in which the worm was capable of exerting a maximum force of 31.33 μN. The average decrease in force implies that the complex pillar arrangement of the *'Honeycomb'* design compared to the simple matrix structure from the *'Lattice'* design provided more obstacles to the worm movement and forced the worm to exert larger forces when pushing against the measurement pillars.

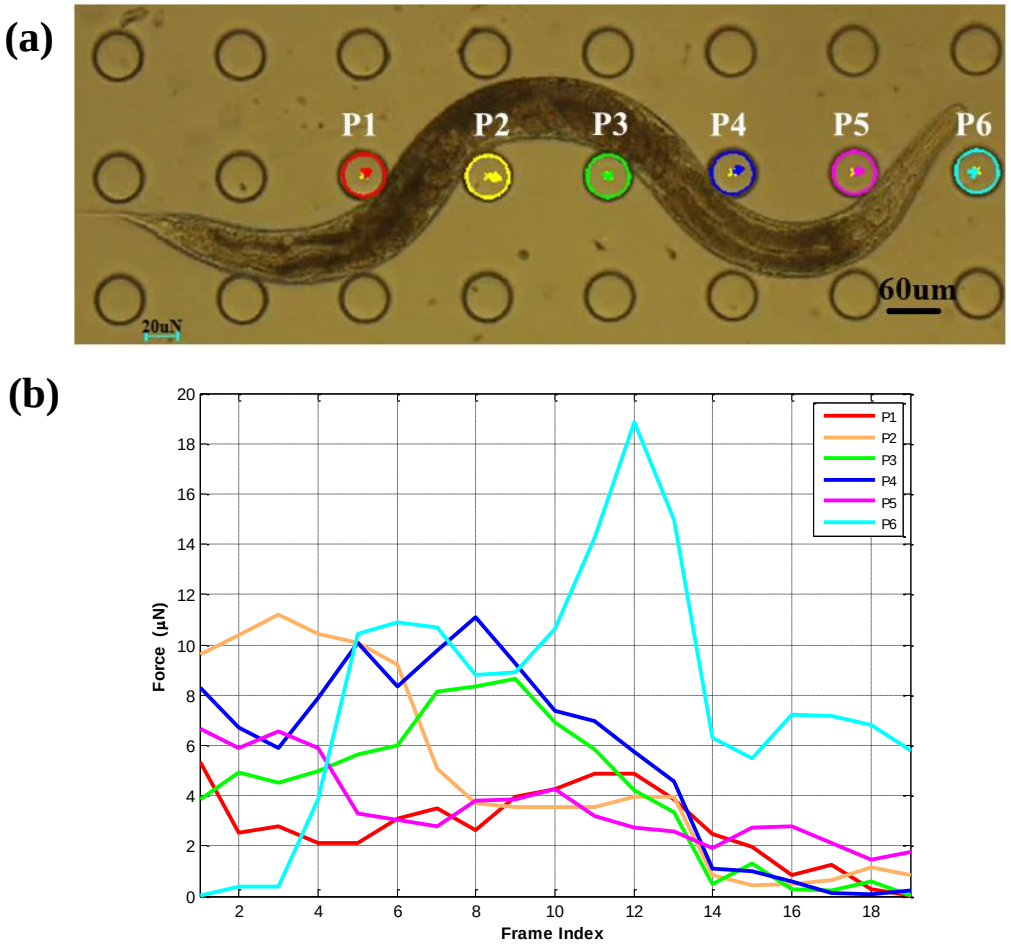

Figure 6.4: C. elegans *motion in 'Lattice' design with the pillar centre-to-centre distance of 140 μm. (a) The worm is in contact with 6 different measurement pillars and (b) force magnitude generated on each of the pillars.*

6.2.3 *'Honeycomb'* structure: 110 μm

In addition to the different pillar configuration in the microstructured environment, the pillar centre-to-centre distance was also decreased by 30 μm. The narrow spacing between the pillars often resulted in more worm-pillar contact during locomotion as shown in Fig. 6.5(a). Figure 6.5(b) shows a force plot for a single *C. elegans* in a *'Honeycomb'* design structure with the pillar centre-to-centre distance of 110 μm. During this 8 s (40 frames) period, the worm made contact with ten different measurement pillars which were distributed along the body length. The maximum force was generated from the posterior field of the worm body at pillar 1. In an attempt to correlate the worm body wall muscles with the generated force, comparison has been made between the position of the pillar and the touch receptor neurons. From this analysis it appears that the location of pillar 1, which is very close to the PVM touch receptor (see Fig. 6.1), might be the main contributing factor.

(a)

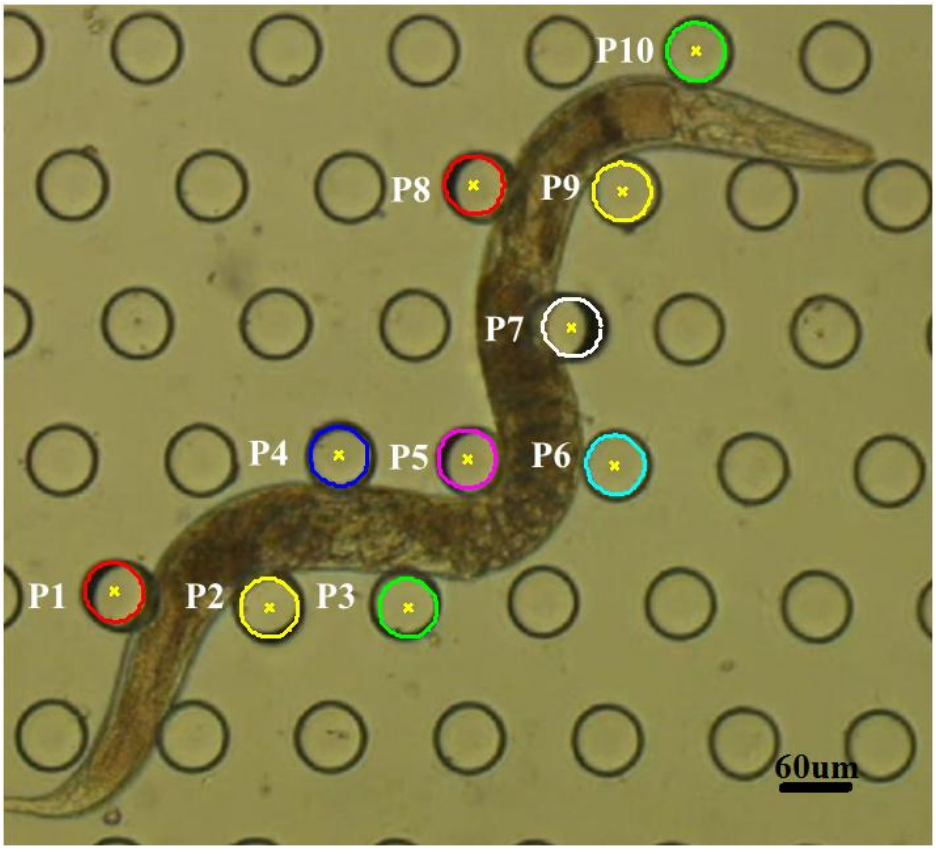

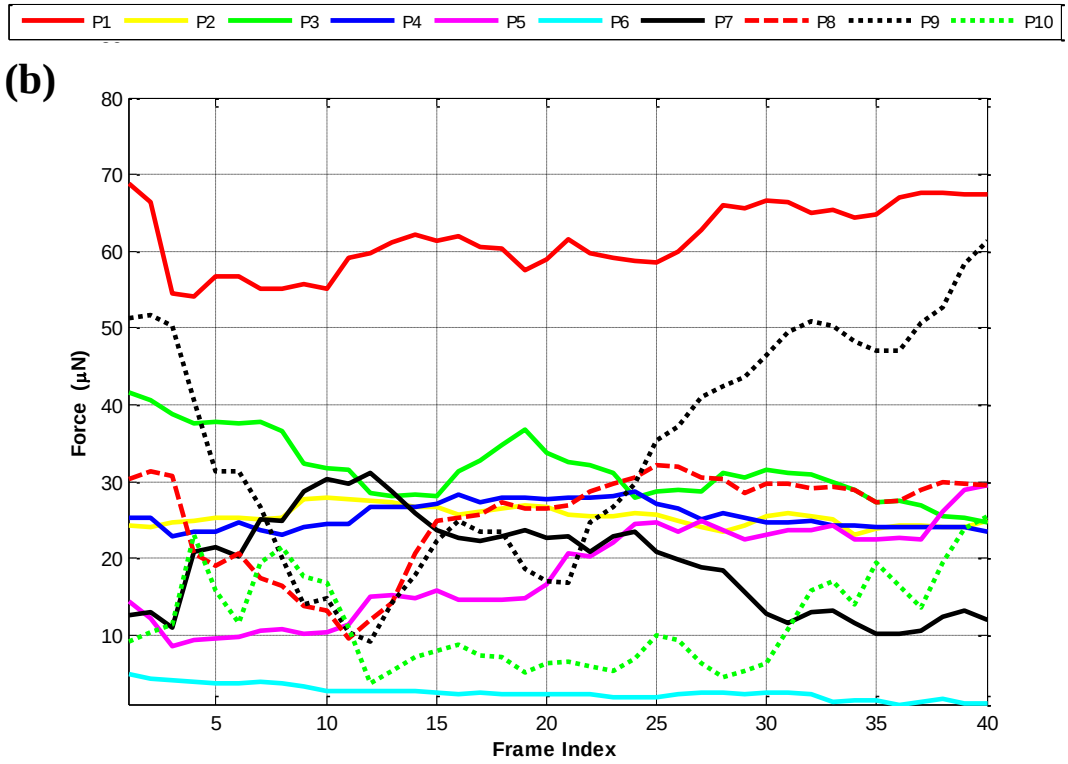

Figure 6.5: *(a) The 'Honeycomb' design using the narrow spacing of 110 μm. The worm is in contact with 10 different measurement pillars. Worm posterior is at pillar 10 while the anterior part is at pillar 1 and 2. (b) The force magnitude generated on each of the pillar using the 'Honeycomb' design is plotted in the graph.*

6.2.4 *'Lattice'* structure: 110 μm

The same narrow spacing was implemented on the lattice pillar structure. An 8 s (40 frames) video segment was processed for an individual *C. elegans*, which generated an average force of 4.7 μN (see Fig. 6.6). During this movement period, the worm started with forward movement and changed its direction by reversing backward at 1.6 s. This motion increased the generated force, especially around pillar 1 and 4 where a maximum force of 13 μN was exerted. It might be hypothesized that since this particular part of the worm's body is close to the AVM and PVM touch receptor neurons, the associated body wall muscles around it are highly sensitive to changes around its body especially during the reversing motion. The exerted forces (around pillar 1 and 4) then dropped to 9 μN and were observed to be constant throughout the entire remaining motion sequence.

(a)

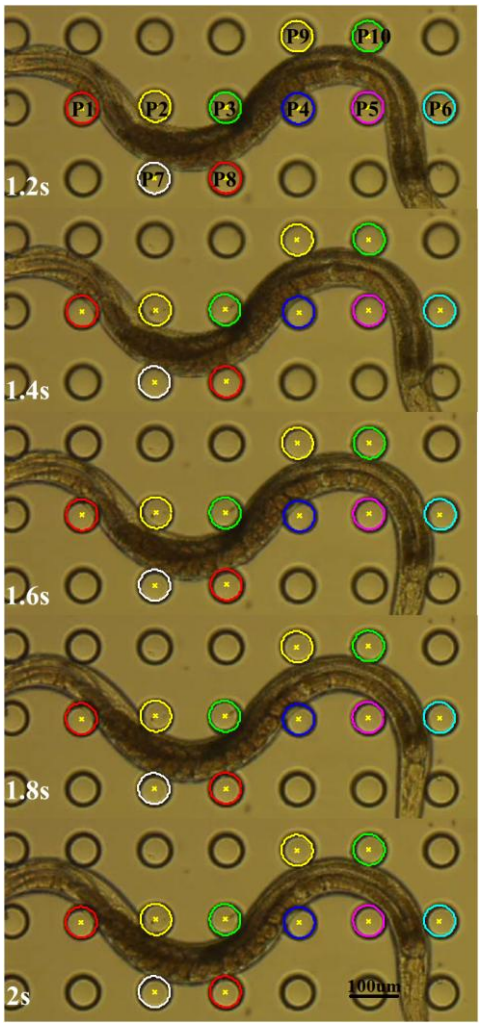

(b)

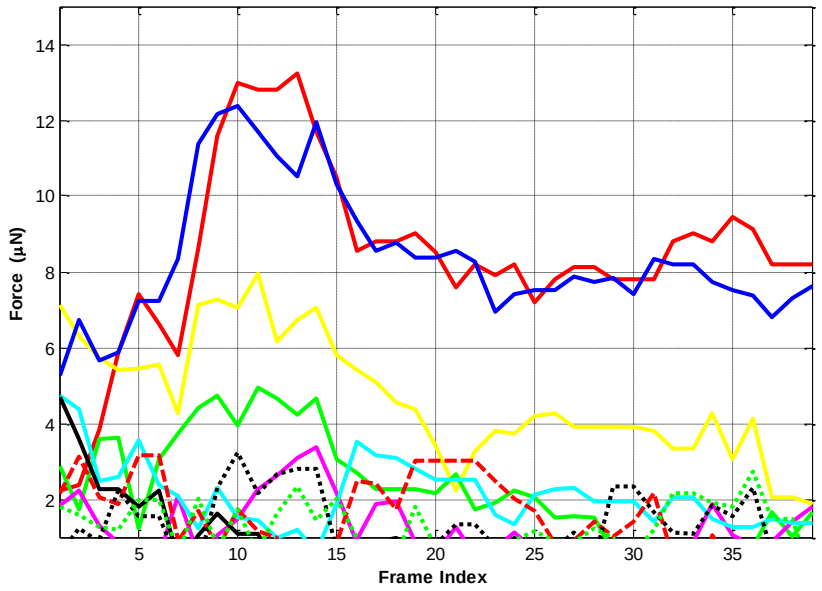

Figure 6.6: *The force from the narrow spacing of 110 µm in the 'Lattice' design. The worm is also in contact with 10 different measurement pillars and the exerted force magnitude on each of the pillar is plotted in the graph.*

6.3 Force Comparison for Different Pillar Structures

During the experiments, three worm samples were used for each device, with each worm's locomotion recorded for the duration of 4 to 8 s. The average force f_{ave}, is calculated from the forces data generated during motion from different part of the worm's body on all pillars during the recorded motion. It should be noted that the number of pillars vary for different design structure. The force average from all pillars, f_p can be defined as

$$f_p = \frac{f_1 + f_2 + f_3 + \ldots\ldots\ldots\ldots + f_n}{n} \tag{6.1.1}$$

where n is the number of pillars involved during motion. For the duration of a recorded video with frame index x, the average force is

$$f_{ave} = \frac{f_p}{x} \tag{6.1.2}$$

For the *'Honeycomb'* design, at least six pillars were observed to make contact with the worm's body and the number of pillars increases when the pillar centre-to-centre distance decreases. The same applies to the *'Lattice'* pillar design arrangement. Worms generated higher forces when they were in the *'Honeycomb'* structure, and the narrow grid spacing in this particular layout resulted in a 64% increased average force compared to the bigger pillar spacing of 140 μm. It was also found that when inside the *'Lattice'* pillar arrangement, the worms' locomotion forces were smaller compared to when moving inside the *'Honeycomb'* structure. Although the main reason behind this is currently still unclear, it was believed that the simplicity of the pillar arrangement in the lattice design might be a major contributing factor. In addition, the wider gap between the adjacent pillars (140 μm pillar centre-to-centre distance) provides less restriction to movement of the worms as they exert very low average forces during motion. Similar worm patterns were also observed in both device structures with wider gap as worms exhibit sinusoidal pattern along pillar row with a period of four posts. The worms were also in contact with pillars in the

adjacent row, which could suggest that the reaction forces at the adjacent row are important.

The measured forces of all the worms for these test structures were then examined. Figure 6.7 shows the average force collected from 12 different worms (based on 4665 data points in total). From each locomotion measurement, six to ten pillars were involved during the recorded motion of approximately 4 to 8 s. This means that, for each motion, approximately 360 force data points can be accumulated. It is apparent that there are distinct qualitative differences in the measured locomotion forces. From this it can be verified that *C. elegans* locomotion forces are highly dependent on their environment. The complex arrangement of the *'Honeycomb'* structure and narrow micropillar spacing pose more resistive obstacles during movement, thus requiring the worm to generate greater force thrusts while navigating in between the pillars. As the spacing increases, it was observed that the generated forces decrease. The number of pillars that are in contact with the worm also decreases, and the nematode was observed to readily weave its way through the micropillars. Although forward locomotion is the main movement pattern of the nematode, it was found that on a few occasions the worms exhibited other movement behaviours. For instance, worms were observed to reverse their motion especially when faced with a choice of direction.

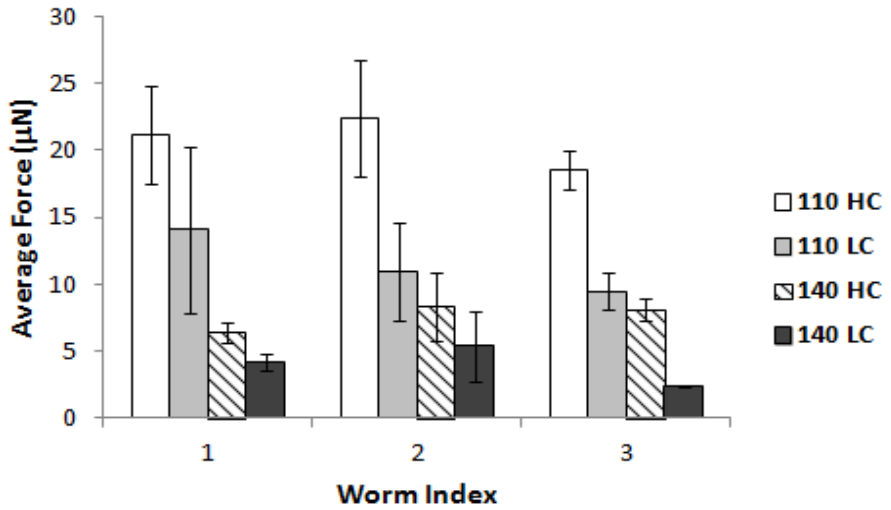

Figure 6.7: *Average force for twelve different* C. elegans *measured in the four different device designs. The error bars represent the standard deviation of the measurements.*

6.4 Measurement of Other *C. elegans* Locomotion Parameters

Worms were also observed to move at different speeds when inserted in a different pillar layout. To study this, the locomotion speed for each individual worm in each of the different arrangements was measured using the ImageJ software package [93]. Figure 6.8 plots the average locomotion speed (average over all image frames in a sequence) of 12 individual *C. elegans* (error bars are standard deviations for n = 3) as a function of the device design structure and its pillar centre-to-centre distance. The average speed is taken over the sum of distances of the worm middle body part between each pair of adjacent frames and the worm direction is not taken into account.

The wide range of locomotion speeds produced by the worms in different test structures is immediately apparent, especially for the case where the pillar centre-to-centre distance was 140 μm. As expected, the worm moved the slowest (57.8 μm/s) in the design with the narrowest pillar centre-to-centre distance of 110 μm. The locomotion speed increases as the spacing increases, with the average recorded speed of 150 μm/s for the pillar centre-to-centre distance of 140 μm. When comparing the pillar layouts, worms were observed to produce higher speeds moving in the *'Lattice'* structure compared to the *'Honeycomb'* test arrangement. It was found that the average speed increased by 39% in the former design compared to the latter. When comparing the measured speed with the worm locomotion on conventional agar plates, it can be concluded that the worms' movement in the wider spacing of 140 μm between the pillar centre-to-centre distances matched the typical movement behaviour observed for natural agar without any microstructured pillars. It thus seems likely that the gap between the pillars, which is equal to the worm's body width, provides easier navigation for the worm compared to the narrow spacing. This suggests that when moving inside the *'Lattice'* structure with the wider spacing, worm motion is enhanced and this is consistent with the observation that the exerted force is 8 μN lower compared to the narrow spacing. In contrast, the nematodes have to exert larger forces when navigating through the obstacles provided by the narrow spacing hence slowing down their motion speed.

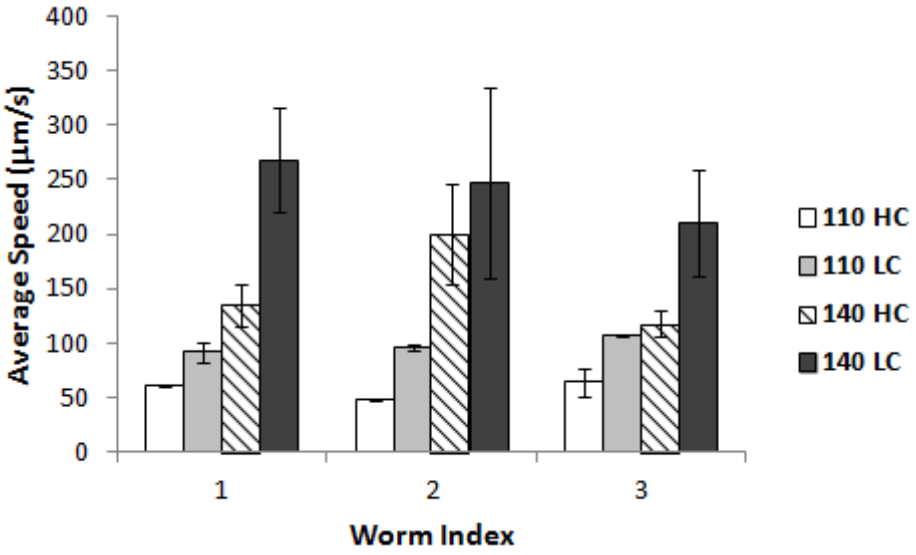

Figure 6.8: *The average worm speed measured during locomotion from each device.*

In *C. elegans* locomotion study, the mechanical features of the the nematode gait are typically characterized by propulsion force, the gait velocity, body amplitude and wavelength and undulation frequency. The understanding of these parameters is crucial as it can provide insight into the different undulatory movement patterns observed in *C. elegans* studies. *C. elegans* moves by propagating undulatory sinusoidal waves from its head to tail. These waves can be quantified by measuring the magnitudes of the amplitude and the wavelength values. The shape and speed of this undulation depends on the physical environments and it often affects the frequency of the nematode movement.

Figure 6.9 shows the measured undulation frequency (F = speed/wavelength) as a function of the device structure. It can be seen that the frequency increases steadily from the narrow spacing of *'Honeycomb'* design to the wider spacing of *'Lattice'* pillar arrangement. This variation in the undulation frequency verifies that the worm responds to different geometric constraints imposed by the pillar arrangement through changes in the period at which it flexes its dorsal-ventral body wall muscles. This also suggests that the worms' undulation frequency depends on the micropillar arrangement. Control tests were conducted on agar plates where worm locomotion parameters were recorded prior to transfer and compared to average values and those

observed inside the device. This was done to ensure that only healthy worms were transferred and the worms had not been affected by the transfer process.

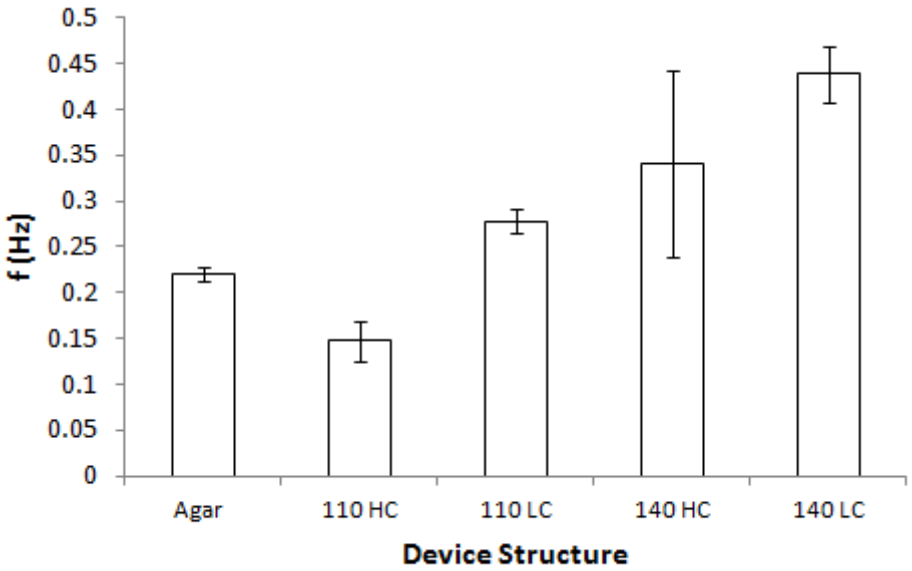

Figure 6.9: *Comparison of* C. elegans *undulation frequency in different devices. Error bars are standard deviations for n = 3.*

Two of the important indicators of worm adaptability to its environment are sinusoidal body amplitude and wavelength during motion. These parameters were measured manually using ImageJ software package for every single worm where each individual worms contribute to 3 data points and the average values (based on 36 data points from all test structures) are plotted in Fig. 6.10. For the narrow pillar spacing, the amplitude ranges from 150 to 180 μm, and increases to 200 to 300 μm when worms move inside the pillar design with wider spacing. It was observed that in the test configurations all worms show sinusoidal movement similar to their natural environment, while variation of the pillar spacing appears to change their body amplitude. The change of the pillar structure however does not change their body shape as they appear to be able to adapt to both the *'Honeycomb'* and *'Lattice'* structure similarly. Despite the changes in the pillar arrangement, measurement of the worm body amplitude in these fits the amplitude ranges reported by Parashar et al.[39], where smooth movement of *C. elegans* was reported in the amplitude range of 91 to 225 μm. This also agrees with findings by Lockery et al.[38] who observed

worms crawling easily when their amplitude waveform matched their designated channel amplitude of 100 to 200 μm.

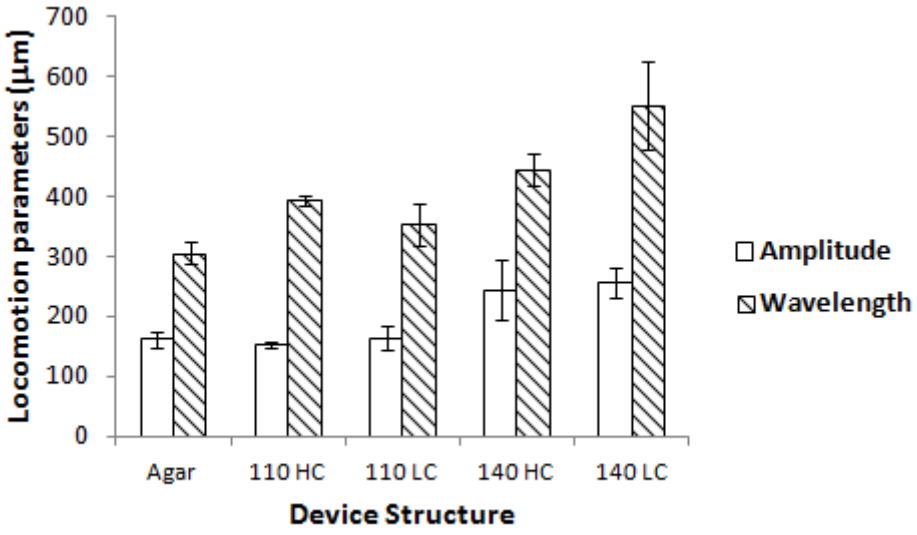

Figure 6.10: *Plot of locomotion amplitude and wavelength for twelve C. elegans samples. Error bars are standard deviations for n = 3.*

Furthermore, the recorded magnitudes of amplitude and velocity are relative: the worms produce larger amplitudes when they move faster. The observed magnitudes of body wavelengths and the pillar spacing are also relative with the worms exhibiting bigger wavelengths when navigating through the wider spacing. These values suggest that, in the reported microstructured environment, the worms showed similar crawling motion to that observed on the agar culture plates.

From the reduced pillar spacing, it was found that the maximum force exerted during motion increased two-fold if compared to the larger pillar distance spacing. The narrow spacing between the pillars provided more resistance for the worm to propel itself during movement, hence producing bigger force thrusts. This provides further evidence regarding force thrust and thus supports the result reported by Berri et al.[94], who found that *C. elegans* modulates its frequency of undulations as a function of the resistivity of the physical environment.

6.5 Summary

The main advantage of the proposed device is its capability to quantify multipoint forces rather than single-point forces of a moving *C. elegans*. To date, prior work in microscale force sensing technology (experimental apparatus) for the nematode *C. elegans* is limited to capturing single points to estimate the worm's forces [52, 54]. On the contrary, the system developed as part of this study allows one to collect force data through up to ten simultaneous measurements from different parts of the worm body. This is a significant step forward as it enables researchers to explicitly quantify the relative difference in forces exerted by the worm's different body segments during the worm movement.

The device capability to determine multipoint forces of the nematode motion can also generate meaningful data to compare forces associated with different worm body muscles, gaining new understanding into how these muscles function. The forces measured during locomotion in the micropillars could also be used to differentiate mutant phenotypes. During movement, *C. elegans* depends on the transduction of their touch receptor neurons in order to navigate its environment. For example, it has been reported that mechanosensory mutants (mec-4, mec-10) fail to navigate in short agar pillar structures [37]. Thus, it will be of interest to quantify the force exerted from such mutants and compare it with the forces exhibited by wild type *C. elegans* reported here. The comparison should provide new insight into the connection of the worm's touch receptors with the locomotion system. Apart from locomotion forces, the proposed device is also capable of conducting concurrent measurement of other locomotion parameters such as speed, amplitude and body wavelength. This additional information can be useful to further quantify phenotypic behaviour of *C. elegans* and deepen the understanding of the theory behind worm locomotion forces measured in this work.

The relationship between *C. elegans* locomotion forces and their environment were analyzed by using two different micropillar layouts, namely the *'Honeycomb'* and *'Lattice'* design structure. Simultaneously, the measurement of *C. elegans* locomotion parameters (amplitude, wavelength and velocity) was also conducted and reviewed in

this chapter. Twelve wild-type *C. elegans* sample worms were tested during experiments to obtain a total of 4665 data points. The experimental results lead to several key findings. These include:

(i) The maximum force is exerted when the pillar is in contact with the middle part of the worm body,

(ii) *C. elegans* locomotion forces are highly dependent on the structure of the surrounding environment,

(iii) the worms' undulation frequency and locomotion speed increases steadily from the narrow spacing of '*Honeycomb*' design to the wider spacing of '*Lattice*' pillar arrangement, and

(iv) *C. elegans* maintain their natural sinusoidal movement in the microstructured device, despite the existence of PDMS micropillars.

The results indicate that the microstructured environment significantly affects the worm's contraction force, locomotion speed and the undulation frequency. All three quantities depend on the micropillar spacing and arrangement. Nematode locomotion forces were greater in the *'Honeycomb'* structure and locomotion was enhanced inside the *'Lattice'* pillar arrangement. In comparison, the average locomotion forces in narrower spaced pillars increased by 50 to 64%, depending on the layout. The nematode navigation in the narrow pillar spacing particularly using the *'Honeycomb'* design was found to be relatively slow compared to the wider pillar spacing in the *'Lattice'* design. Comparison with literature [5, 38, 39, 94] indicates the validity of these findings. Adding to the significance of these findings, the primary contribution of the device is that it allows one to investigate continuous multipoint forces measurement over the entire *C. elegans* body during locomotion, which to the author's knowledge, has never been reported before.

CHAPTER 7

C. elegans Locomotion Forces on Other Substrates

In Chapter 6, the feasibility of a PDMS device to study *C. elegans* locomotion forces in a microstructured environment was established. As part of this, the worm locomotion environment was varied in order to investigate the effect of the different surroundings represented by the geometric positioning of the pillars. This locomotion force was defined based on a point force acting on the pillar half height implying that the bulk of the force acts on the middle of the pillar, as stated in Chapter 3. This chapter will investigate further analysis that the preceding set up failed to accommodate: the worm locomotion on a different material/substance instead of PDMS. To this end, a preliminary investigation on *C. elegans* locomotion forces on different substrates will be conducted. The goal of this chapter is to provide an alternative to the environment parameters used to study *C. elegans* locomotion, as discussed from Chapter 3 to Chapter 6. This is achieved by modifying the measurement technique provided by the proposed PDMS device. By inverting the existing PDMS device, the measurement method is modified in a way that the force is calculated based on a point force acting at the pillar tip and the worm substrate can be varied and is no longer limited to PDMS.

7.1 Overview

Much research has been conducted and published regarding the locomotion of the nematode *C. elegans*. The periodic patterns of the muscle activity that actuate *C. elegans* movement are produced and regulated by the worm's neural circuits. The muscle activity also produces a certain type of movement within a particular physical environment. The basic mechanics of how the neural circuits work is currently poorly understood. *C. elegans* move through their environments by choosing a certain pattern of movements which is often referred to as gaits. These gaits depend on the nature of their physical surroundings which includes both the material and geometric properties of the neighboring environment [95, 96]. For instance, by using gels of varying stiffness [94], it was found that the worm's body amplitude, wavelength and oscillation frequency constantly decreases as the substrate medium viscoelasticity increases. In a different example, Korta et al.[97] found that the worm body amplitude and wavelength is retained and the undulation frequency drops by 20 % when the fluidic viscosity is increased by a factor of one thousand.

However, one of the main shortcomings of these studies is that they do not include the nematode locomotion force measurement. This chapter provides an alternative to the measurement method of the PDMS force sensing device by modifying its measuring technique in order to quantify *C. elegans* locomotion forces on different substrates. As previously discussed, the device introduced here works by placing the nematode inside the device and the force measurement can be calculated from the bending and deflection of the PDMS micropillars integrated into the PDMS substrate. Though this method has shown its capability to provide information on *C. elegans* force measurement, the measurement obtained from this study is limited to PDMS or other elastic materials amenable to pillar fabrication. Since the mechanical and chemical properties of PDMS devices differ from standard plates traditionally used in nematode studies, a modified, substrate-independent version of the measurement technique is introduced in this chapter.

7.2 Force Measurement Model Revisited

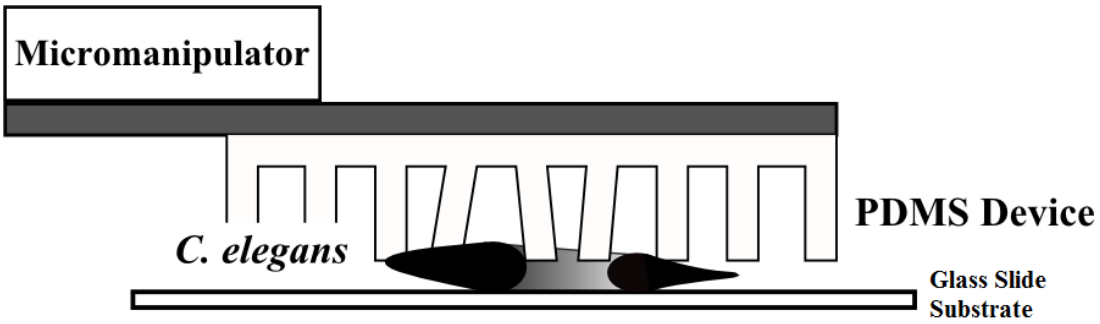

Figure 7.1: *Experimental setup for substrate-independent force measurement in* C. elegans *locomotion.*

As depicted in Fig. 7.1, the PDMS device was plasma-bonded to a glass slide and inverted, so that the pillar tips face towards a surface of interest. A micromanipulator (Sutter Instruments MP-285) was used to control the device movement, ensuring that the pillar tips will not collide with the substrate. The positioning of the pillar tip on top of the substrate requires special attention as the gap in between them is approximately the size of the worm's body width (~ 100 μm). However, this can be resolved using a micromanipulator which provides submicron resolution and continuous display of the axes positions. The specific distance between the substrate and the pillar tip can be inferred from the micromanipulator motions. Although the device configuration of the current study is different to that of the previous chapter, a variation of the force measurement model described in Section 3.2 can still be applied. In the previous development of the force model in Chapter 3, the scenario depicted in Fig. 3.1(a) was considered in which the nematode was set between adjacent pillars. The worm force F_e was chosen to act at the pillar midpoint at *h/2*. The approach in this chapter will differ slightly. Because the worm is now moving on a separate substrate which is placed underneath the inverted device, it is anticipated that the worm will contact the pillar at the pillar tips rather than at the pillar half height. Thus the force is calculated from the deflection caused by the worm's contact approximated as a point force at the pillar tip (see Fig. 7.2).

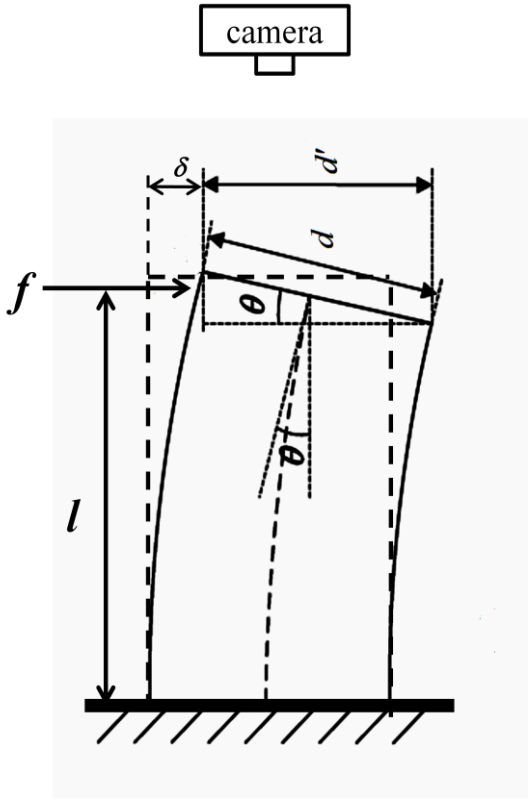

Figure 7.2: *Schematic of the bending pillar for force calculation.*

The PDMS micropillar is regarded as a cantilever beam, fixed at one end and loaded with a force at the other end, undergoing pure bending and shearing (Fig. 7.2). As the worm glides on top of a particular substrate, the force is now approximated to be applied as a point load acting near the tip of the free end of the pillar which is held close to the top of the substrate. From the beam bending theory, the relationship between the force, *f* and the pillar tip displacement, δ, for a cylindrical beam is given by

$$\delta = \left(\frac{l^3}{3EI} + \frac{d^2(1+\gamma)l}{4EI} \right).f \qquad (7.2.1)$$

where *f* is the force, *l* is the pillar height which is equal to *h* in Equation (3.2.7), *I* is the area moment of inertia, and *E* and γ are Young's modulus and Poisson's ratio for PDMS, respectively. The first term in Equation (7.2.1) corresponds to pure bending and the second term refers to shearing which has to be considered because of the low aspect ratio of the pillar (see Section 3.2).

The pillar diameters are considered uniform along the height, which was verified by high-magnification SEM imaging (see Fig. 3.1(*b*)), thus *I* can be defined as

$$I = \frac{\pi d^4}{64} \tag{7.2.2}$$

The force can thus be calculated by using this equation

$$f = \frac{\delta}{\left(\frac{l^3}{3EI} + \frac{d^2(1+\gamma)l}{4EI} \right)} \tag{7.2.3}$$

The stiffness of the pillar can be determined using the following equation

$$k = \left\{ \left(\frac{l^3}{3EI} + \frac{d^2(1+\gamma)l}{4EI} \right) \right\}^{-1} \tag{7.2.4}$$

7.3 *C. elegans* Locomotion Forces on Agar Substrates

C. elegans behavioural studies are traditionally conducted on the smooth agar substrates prepared in the laboratory. The following sections first present details of experimental preparation and setup, and then the experimental observations will be discussed. Initially, the PDMS device is bonded on a glass slide using a technique known as plasma bonding. When the device is securely bonded on to the glass slide, both the glass slide and the device are inverted and affixed to a three-axis micromanipulator (Sutter Instruments MP-285). The micromanipulator is used to adjust the distance between the PDMS pillar tip and the agar substrate. Worms are then transferred to a piece of clean agar cube (~ 1 cm^3) and placed on a separate glass slide which is then positioned on the microscope stage.

When the worm has been visualized under the microscope, the device is brought into the microscope view and the micromanipulator is used to lower the device and simultaneously control the distance between the pillar tip and the worm's body.

While performing this experiment, one major problem was encountered, which is shown in Fig. 7.3. The worm's body is surrounded by a thin film of water and is held to the agar surface by surface tension. Although it was possible to position the device slightly above the agar surface, when the worm's body came in contact with the pillar tip, the moisture transferred from the worm's body regularly contaminated the PDMS tips. Because of this, the quality of the captured images of the pillars' tops was very poor. Since the force calculation is determined directly from the image, the accuracy of the force calculation is strongly dependent on the captured image quality. Consequently, this limits the device capability to measure the worm forces when moving on the agar substrates. In addition, pillar deflection was not observed during the experiment. Thus it might be hypothesized that the liquid film forming between the agar and the tips reduced the total deflection of the pillars due to surface tension effects. Despite several attempts, no conclusive results on the force measurement of *C. elegans* locomotion on conventional agar substrates could be obtained because of these effects.

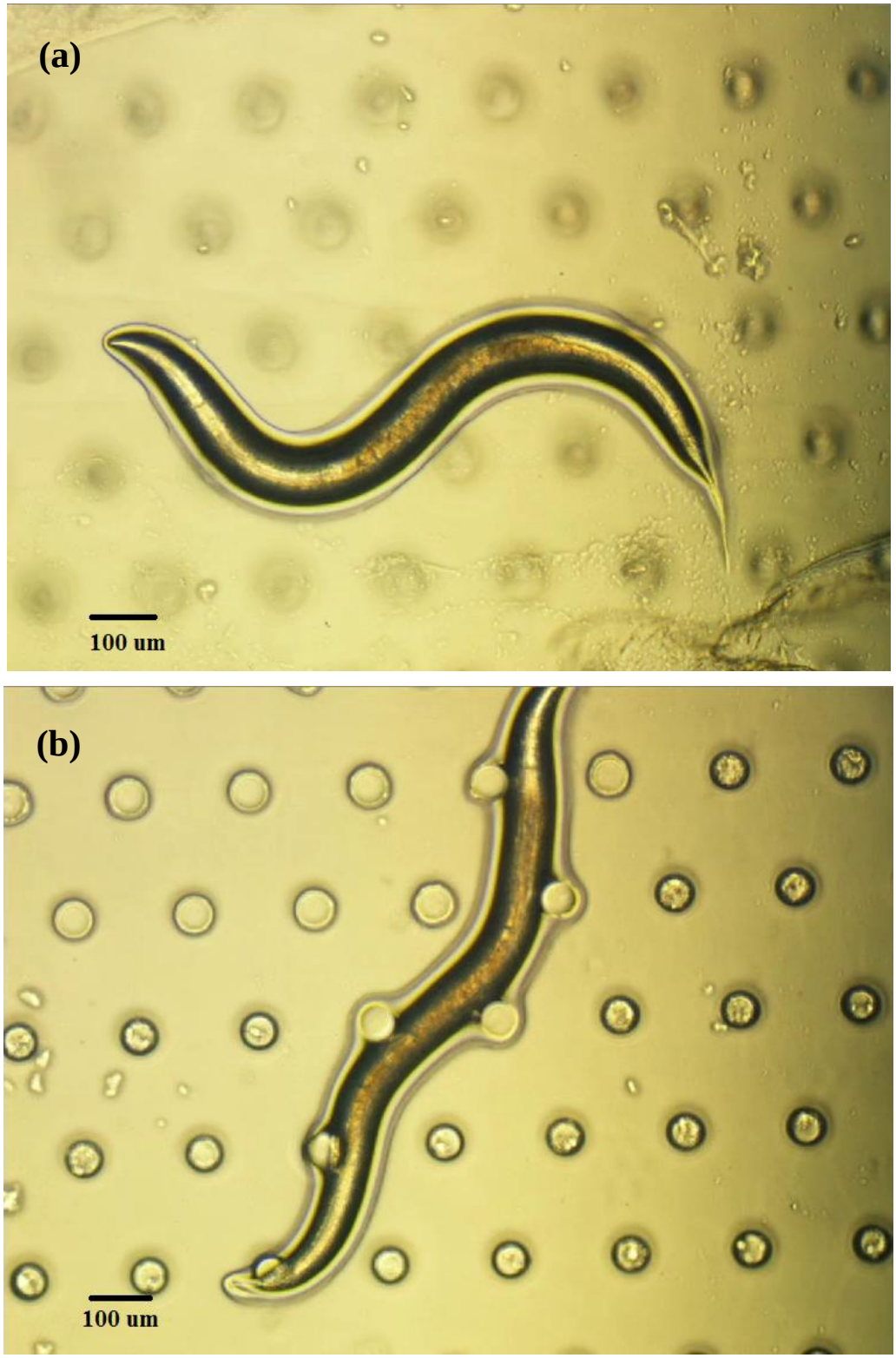

Figure 7.3: *Optical micrographs of* C. elegans *crawling on agar substrate (a) with the PDMS micropillars visible on top of the worm. (b) The moisture transferred from the worm's body often contaminates the tips of the PDMS micropillar.*

7.4 *C. elegans* Locomotion Forces on Microscope Glass Slides

Since any conclusive data from experiments conducted on conventional agar plates failed to be collected, the agar was substituted with standard glass microscope slides. The reason for choosing this substrate is because conventional microscope glass slides have been previously used in *C. elegans* locomotion studies, as reported by [98] . Studies of *C. elegans* locomotion in liquid, typically conducted within drops of fluid on a microscope slide, have shown that the worm is able to change its movement pattern especially when encountering a different substrate medium [96].

Initially, the glass slide was covered with a thin layer of liquid in order to provide a moisture rich environment for the nematodes. The thickness of the liquid is approximated to be less than a quarter of the worm height. A single worm was then placed on the moisturized glass and the device was controlled by the micromanipulator so that the worm's body touched the pillar tip during movement. When moving on the glass slide, the worm was observed to move unlike its familiar movement pattern (see Fig. 7.4) as observed on a conventional agar plates or in the experiments recorded in Chapter 5.

These patterns include an increase in the worm's undulation frequency, as well as the worm's body wavelength, which is consistent with the swimming behaviour as reported by [99]. This however was not the case for every single worm as some of them were found to mimic its conventional sinusoidal body shapes with the guidance of the pillars surrounding them (see Fig. 7.5).

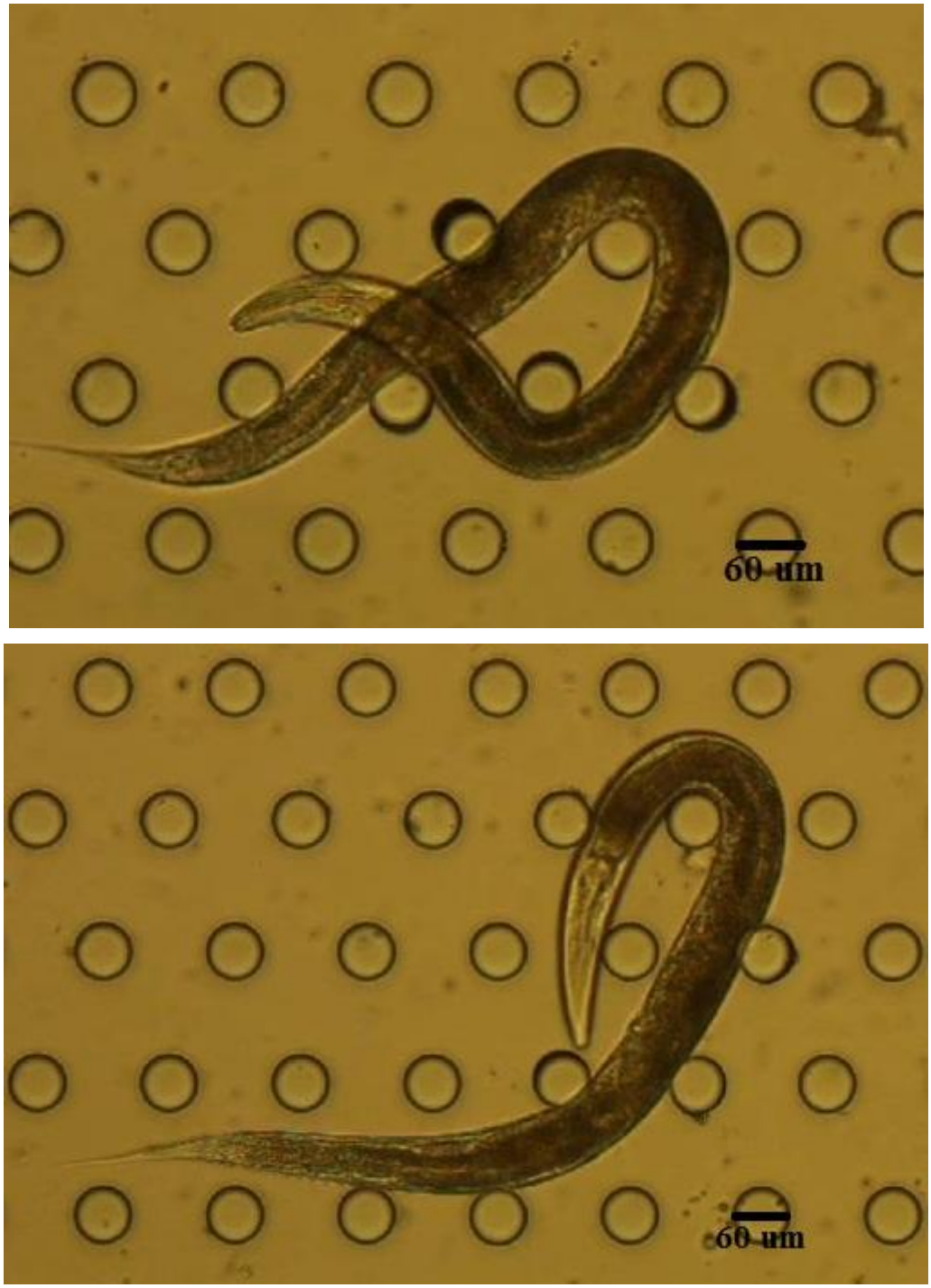

Figure 7.4: C. elegans *random movement observed when moving on a microscope glass slide with some parts of the worm body in contact with the pillar tip, causing the deflection.*

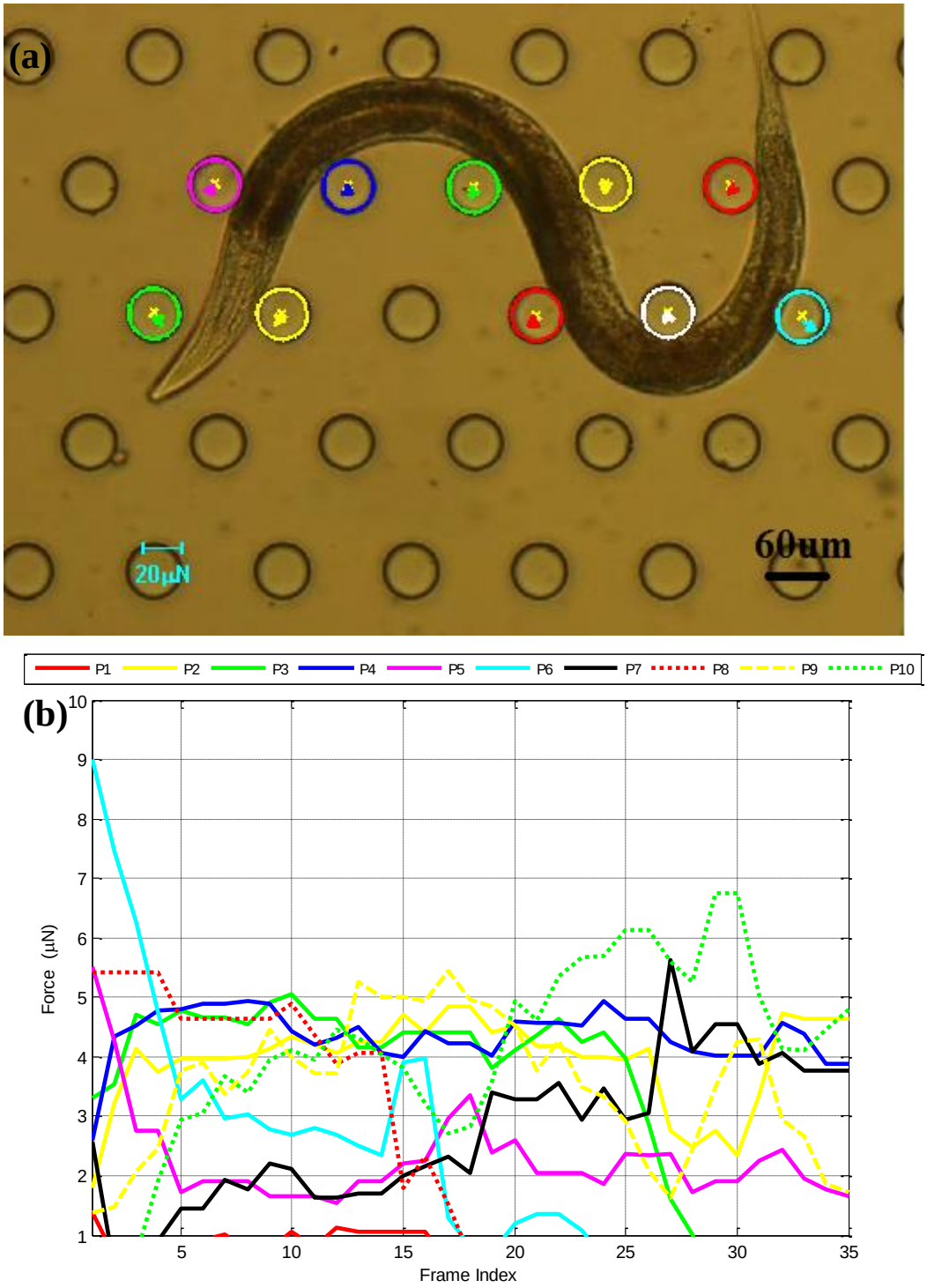

Figure 7.5: *(a) An example of worm behaviour during the experiment when moving on the glass slide. The worm is in contact with ten different pillars. (b) The force magnitude generated on ten different measurement pillars.*

Figure 7.5 shows an example of worm behaviour during the experiment when moving on the glass slide with the plot of the forces exerted by the corresponding worm over duration of 7 s. Ten pillars were involved during the recorded motion. The maximum force calculated was 9.05 µN and the observed locomotion produced an average force of 3 µN (from 360 data points). This result is consistent with the forces reported by Doll et al. [54], who measured in a similar manner.

Even though the substrate used in this chapter is different, the observed force pattern is similar to the one described in Chapter 5. Consider another example of a recorded worm movement on a glass slide for 33 frame images with the recorded force exerted depicted in Fig. 7.6. The increasing force pattern exerted from frame #2 to frame # 5 is related to the worm's head movement where it changes its direction during frame # 3 (see Fig. 7.7 below).

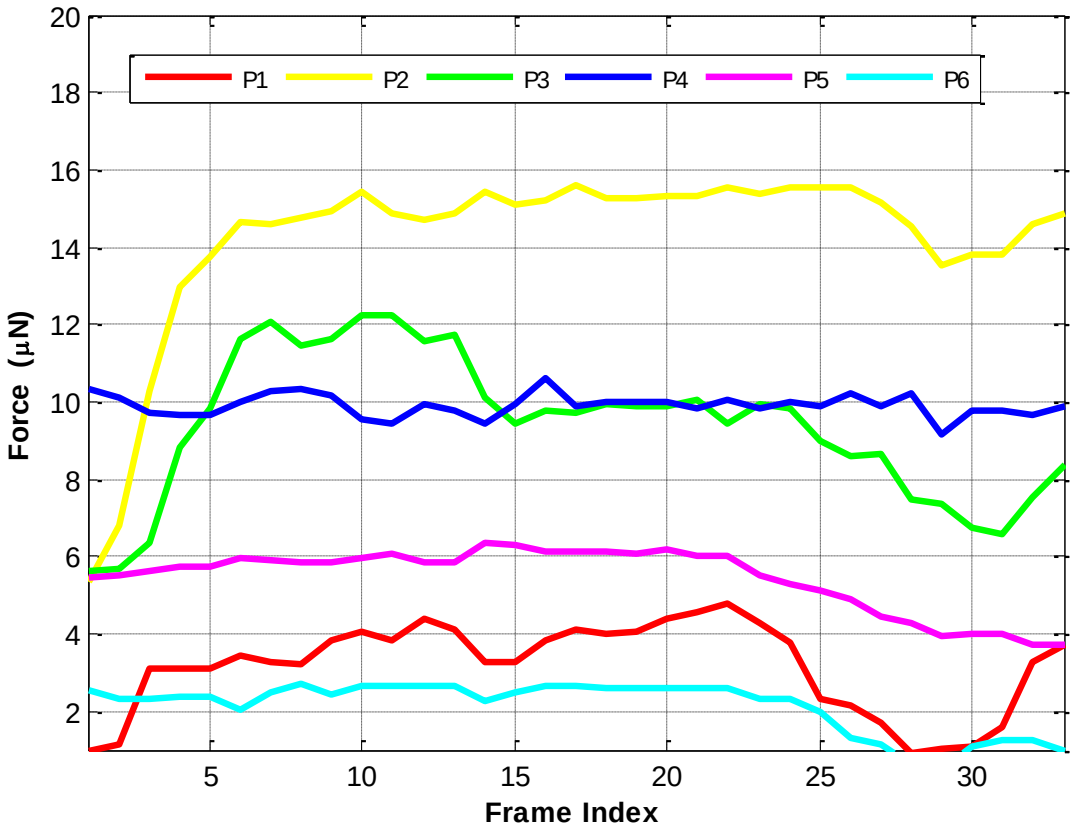

Figure 7.6: *The calculated force magnitude exerted by* C. elegans *locomotion on a glass slides on six pillars of interest for the duration of 6.6 s.*

This is comparable with the previous findings, where the generated force acting on the pillar increases/decreases whenever the worm is moving its head: particularly when changing its movement direction.

Another pattern that is consistent with the results found in Chapter 5 is that the maximum generated force occurs when the micropillars are in contact with the middle part of the worm's body. Figure 7.8 shows the pillar distribution over the worm's body during frame # 22 (refer to force pattern in Fig. 7.7). It is can be seen that the positions of pillar 2, 3, and 4 which are around the middle part of the worm's body exerted higher forces compared to the generated force corresponding to pillar 1, 5 and 6 which are located at the head and tail area of the worm's body segments respectively. This agrees with the theoretical analysis reported by [5] and stated in Chapter 5.

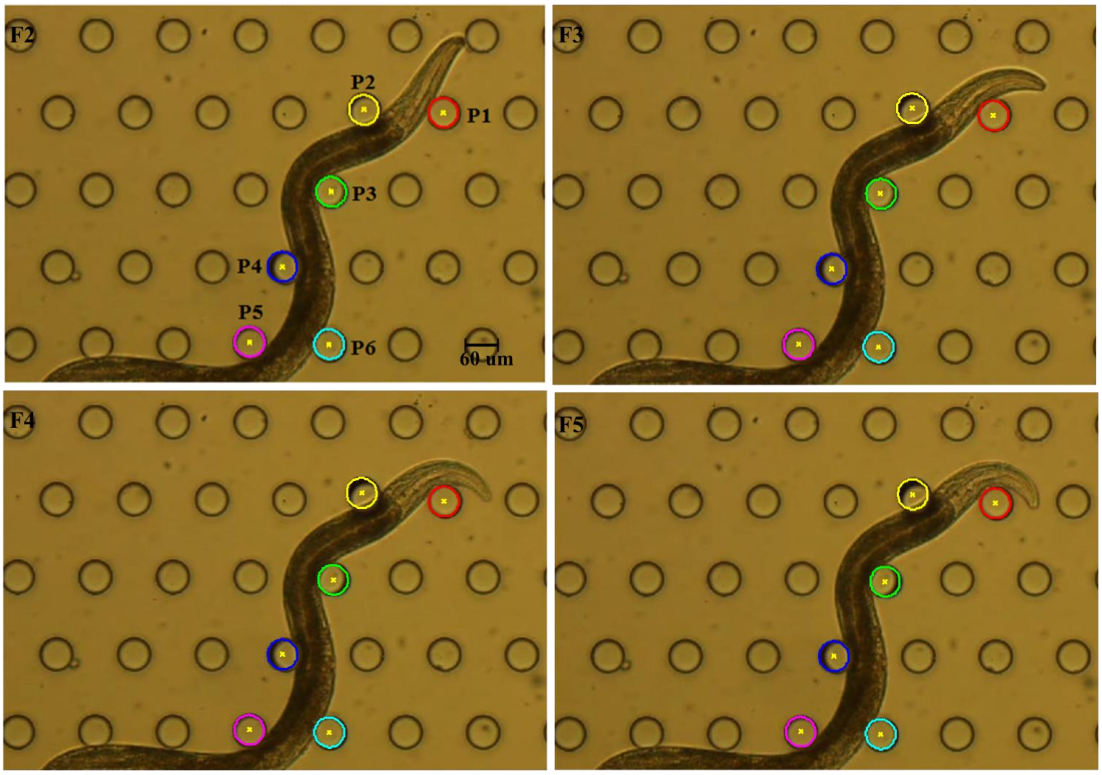

Figure 7.7: *Selected image frame # 2 to frame # 5 corresponding to force plot in Fig. 7.6, indicating the change of worm head movement during frame # 3.*

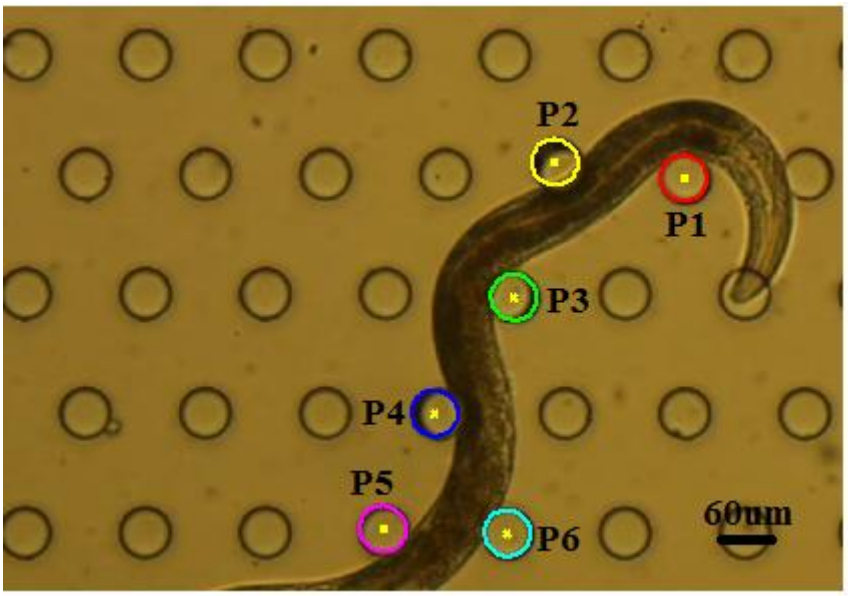

Figure 7.8: *Pillar distribution over the worm's body during frame # 22.*

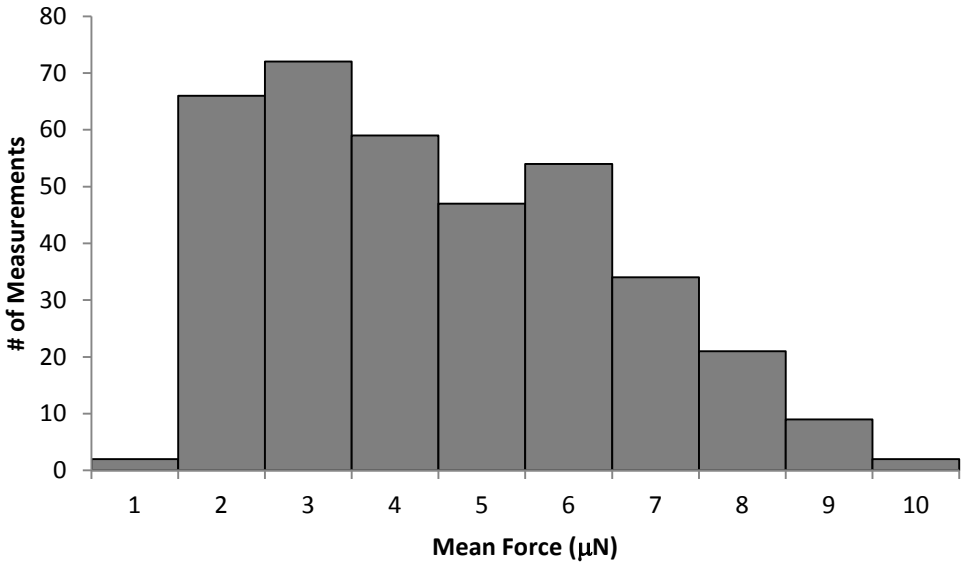

Figure 7.9: *Plot of the average generated forces against the number of measurements conducted during experiment.*

The primary result of this chapter is the demonstration of force measurements of *C. elegans* on different substrates conducted using the PDMS device in inverted fashion. As an example, 5 wild type *C. elegans* were used with each recorded for 30 to 35 frames during which the worms move actively on the glass slide. For each worm sample, 8 to 10 pillars that were deflected over the imaging time were processed to retrieve the force levels. Figure 7.9 shows the histogram of the measured forces from a number of 366 measurements for 5 different nematodes. The average force is calculated from the forces data generated during motion from different part of worm's body on all the contacted pillars, as defined in Equation (6.1.2). The recorded motion typically lasted for a brief 4 to 8 s. All the measured forces were less than 15 μN with 80% of the measured forces are between 2 to 6 μN.

7.5 Summary

The limitation of the substrate used to study *C. elegans* locomotion forces reported in Chapter 6 can be resolved by using the alternative measurement technique inspired by the proposed PDMS device described in this chapter. The experiment demonstrated above provides preliminary findings of the forces calculated from 5 different nematodes with the total of 366 measurements conducted. When moving on the glass slides, it was found that the worms use the micropillar tips to facilitate its movement. It is believed that the micropillars on the device assist the worms by providing a semi-fixed matrix to push against, thus guiding their movement and at the same time deflecting to indicate the applied forces. It also seems likely that even though with the micropillar tips on top of the worm body, the liquid on the glass slide surface enforced swimming motions which made movement unlike its conventional smooth sinusoidal wave crawling motion [5]. In addition to the microscope glass slide, this measurement technique can also be used to measure forces on other substrates, and worm locomotion behaviour in varying environments can be investigated further. The combination of the conventional measurement technique with the findings reported in this chapter show promise for biological measurements and other sensing application such as tactile force.

CHAPTER 8

Integration of Microvalves for *C. elegans* Manipulation

Having developed an existing force sensor, one of the central ideas behind the system developed in this thesis is to improve the performance of the established system by increasing the number of worms used during *C. elegans* locomotion analysis and allowing the device to analyze the behaviour of multiple worms simultaneously. The objective of this chapter is to demonstrate the combination of the force measurement application with an additional ability to increase control of worm selection and manipulation. This is accomplished by adding new components to the entire system which consists of a series of controllable microvalves. These microvalves require an additional thin PDMS layer membrane and pneumatic supply layer to operate. By carefully controlling the incorporated microvalves, the proposed device is able to select and direct worm movement on-chip and thus increase the number of force measurement results collected. Furthermore, the integration of the microvalve with the PDMS micropillar-based on chip system can be easily combined with other existing nematode screening and imaging systems and, also has the capability to facilitate high-throughput screening of force patterns in *C. elegans* locomotion behaviour.

8.1 Overview

One of the limitations in this study is that the current system is not able to handle the manipulation of multiple worms during an experiment: currently only one worm can be studied at a time. Since the size of the nematodes *C. elegans* is at the microscale level (~1 mm length and 100 μm width), manually loading and manipulating worms during an experiment can be extremely labour-intensive, tedious and time consuming. Hence, to overcome this problem, PDMS microfluidic systems for *C. elegans* selection and manipulation have been reported, with the purpose of integrating several functions on a single device. The existing PDMS microfluidic device designs already incorporate well-established two-layer PDMS microvalves [100] in order to function. For example, in a study by Ma et al. [28], a programmable microvalve-based microfluidic array was developed to individually capture and immobilize worms in order to monitor the mobility behaviour of the nematode. In a different study, an on-chip behaviour module which was developed to characterize the effect of immobilizing the worm using a deformable PDMS membrane to mechanically restrict the worm's movement was reported by Chokshi et al. [40]. The same method was used in [41] for a different application of sub-cellular imaging and microsurgery. An integrated chip combining the functions of sorting, screening and imaging has also been reported by Rohde and co-workers [49]. It has also been used as an automated microsystem integrating high-throughput microscopy and phenotype-based sorting function as demonstrated by Chung et al. [48].

Inspired by these works, a microvalve-based microfluidic device for the manipulation of *C. elegans* for force measurement application is introduced into the design in this chapter. The incorporation of the microvalves could largely facilitate individual worm manipulation and selection for force measurement, and has the potential of providing a high-throughput system in the future. The established structure is capable of collecting more data for detailed force analysis and *C. elegans* locomotion behaviour.

8.2 Device Design and Fabrication

In this section, the proposed design of the microfluidic device will be discussed. This will include the device design itself as well as the fabrication process used to manufacture the device. The microdevice design illustrated in Fig. 8.1 is composed of three PDMS layers fabricated using soft-lithography technique. The top and bottom layer of the device are separated by a thin membrane with the thickness of approximately 20 μm. The bottom layer is referred to as the fluidic layer, and it consists of multiple *x*-direction fluidic channels with two common fluidic inlets at the end and one *y*-direction channel for worm loading with two inlets. Each channel is similar to the prototype Design 2 (Section 4.1.2.2), containing four pillar arrays that function as an independent force measuring unit dedicated to individual *C. elegans*. As a proof of concept, the prototype device is designed to have three force measurement channels (Channels *A*, *B* and *C*) with each channel having four arrays of pillars. The layout and the arrangement of the pillars can be varied depending on the experiment conducted. It is important to note that the number of force measurement channels and arrays is not restricted to the three used in this prototype and can be increased if necessary. The purpose of having multiple force measurement channels is not only to allow multiple worms to be assayed in parallel in one device, but also to avoid the cross-contamination that occurs when multiple worms are subjected to the same channel. An additional benefit is that the experiment is consistent in the sense that for all channels, the same fabrication process will result in consistent and comparable force measurement values across channels.

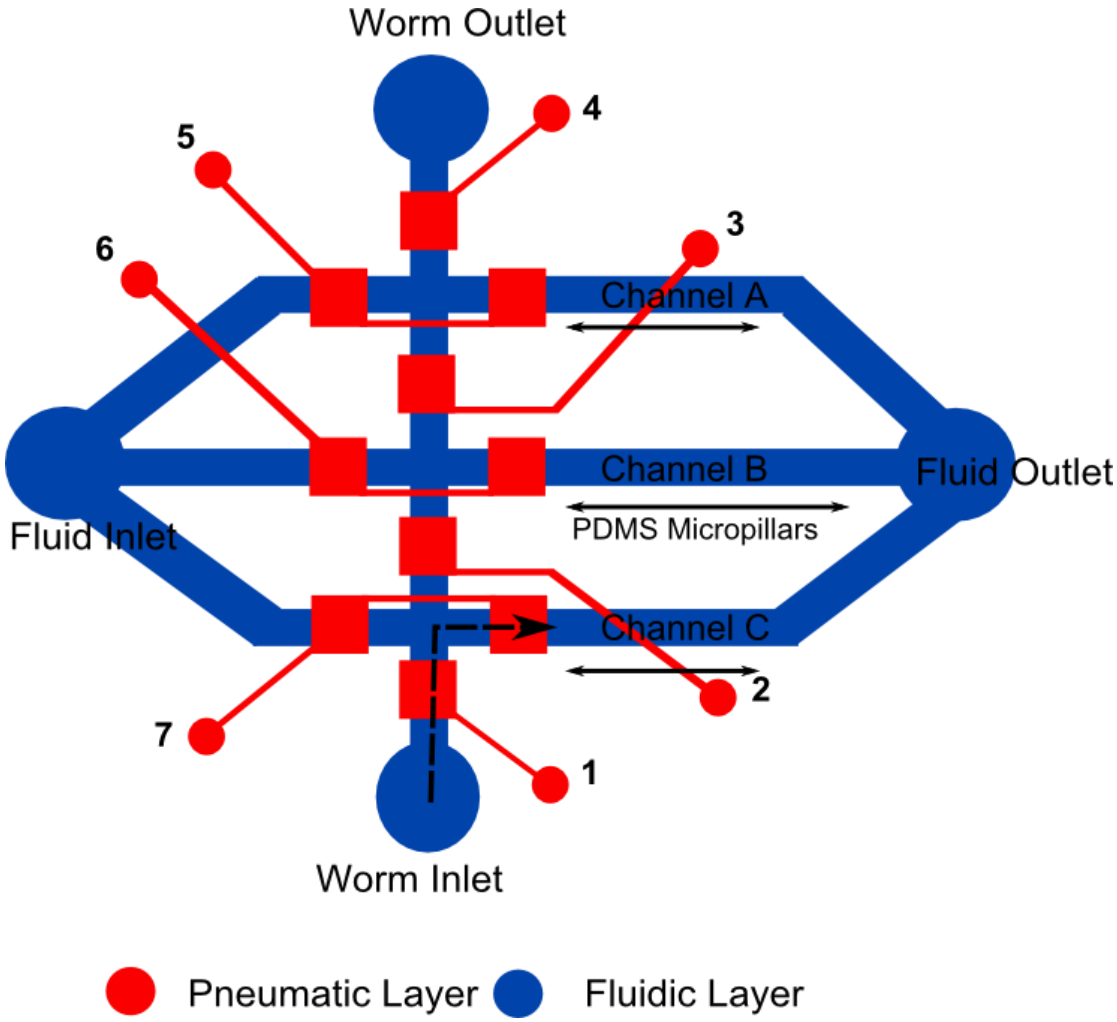

Figure 8.1: *Schematic of the proposed microfluidic device for the manipulation of* C. elegans *for the force measurement application. The arrow from the worm inlet indicates worm movement into a measurement channel.*

As depicted in Fig. 8.1, the top layer (red) is a pneumatic channel layer which functions as valves, whose operation is controlled pneumatically. There are seven inlets for the valves, with each valve located beside the junction of the intersecting channels. The thin membrane in the middle of the device is pressurized to close the channel and restrict the worms' movement; hence worms are separately directed to a certain force measurement channel.

The microfluidic device was fabricated in PDMS (Sylgard 184 Silicone Elastometer) by a replica molding process. Two separate master molds were required for the fluidic channel layer and the pneumatic channel layer. They were fabricated using standard soft-lithography process on a 4" silicon wafer as substrate (see Section 4.2 for

details). The pneumatic layer was prepared by spinning SU-8 2100 negative photoresist (Microchem) at a thickness of 100 µm and softbaked according to the resist datasheet. After that, the pneumatic layer design was patterned by photolithography using a Suess MA6 mask aligner. After exposure, the substrate was post-baked and the resist pattern was developed in SU-8 developer (1-methoxy-2-propyl) acetate in an ultra-sonic bath and finally rinsed with IPA.

The substrate mold for the fluidic device was prepared in the same way as the pneumatic layer with several additions to the process. As the fluidic layer is made of vertical channels and pillars, a two-layer photoresist mold is required. In brief: an initial layer of SU-8 2025 was spin-coated to a thickness of 15 µm, softbaked as determined by the resist datasheet and exposed in a Suess MA6 mask aligner using a high resolution chrome mask to form the channel outline. It was then followed by post-bake and after that a second 100µm thick layer of SU-8 2100 was deposited on top of the first layer. The wafer was softbaked again and exposed through a second mask containing both the channel outline and pillar array. Finally, the resist pattern was developed in (1-methoxy-2-propyl) acetate in an ultra-sonic bath, rinsed with IPA and hardbaked for 20 min at 150°C.

For PDMS replica molding, the polymer was prepared using Sylgard 184; a two-component heat-curing system which consists of a base part and a curing agent part. The polymer was weighed and thoroughly mixed according to 10:1 ratio (base: curing agent), followed by degassing using vacuum desiccators to remove air bubbles. Then the polymer mixture was poured onto the mold and degassed again to ensure that all air bubbles were removed. For a fluidic layer, the mold was then cured on a hot plate for an hour, and 2 hours for a pneumatic layer at 80°C. After cooling to room temperature, both replicas were carefully peeled off and the fluidic layer was cured for a further 3 hours at 80°C to ensure that the pillar structure were fully hardened and the material properties were stabilized. The resulting microfabricated structure of each layer is shown below in Fig. 8.2 on the left side, along with the PDMS cast of the structure on the right.

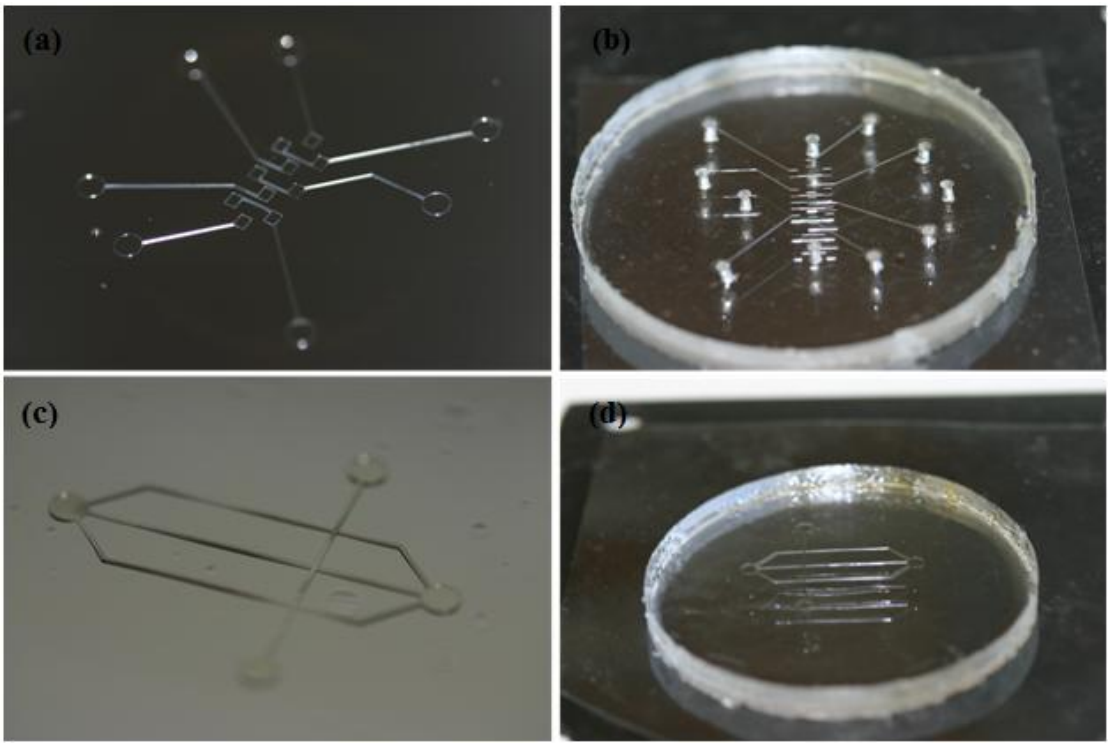

Figure 8.2: *SU-8 molds of the (a) pneumatic layer with its PDMS replicas in (b). The fluidic layer SU-8 mold is depicted in (c) with its replica in (d).*

The thin membrane separating both layers was prepared by spinning about 1 ml mixed PDMS base and curing agent on a blank Si wafer at 3000 rpm for 30 s (which resulted in the thickness ~20 μm) and then curing on a hot plate for 2 hours at 80°C. When both PDMS replicas were ready, the multilayer devices were bonded and assembled together using the oxygen plasma bonding technique.

The bonding of all three layers has to be carefully conducted in order to ensure perfect alignment between each layer. First, the PDMS cast of the pneumatic layer was bonded to the thin membrane layer. The assembly shown in Fig. 8.3(a) was cured on a hot plate for 20 min at 80°C to strengthen the bonding. Then, both the gas layer and the thin membrane were carefully peeled off the Si wafer. In order to ensure that the thin membrane was perfectly bonded to the pneumatic layer, visual inspection was conducted where the bonded area of the pneumatic layer on the thin membrane had been completely removed from the Si wafer (see Fig. 8.3(b)). Afterwards the bonded pneumatic layer and the thin membrane were aligned and bonded again to the fluidic

layer. Figure 8.3 shows the assembled system and key fabricated components of each device layer.

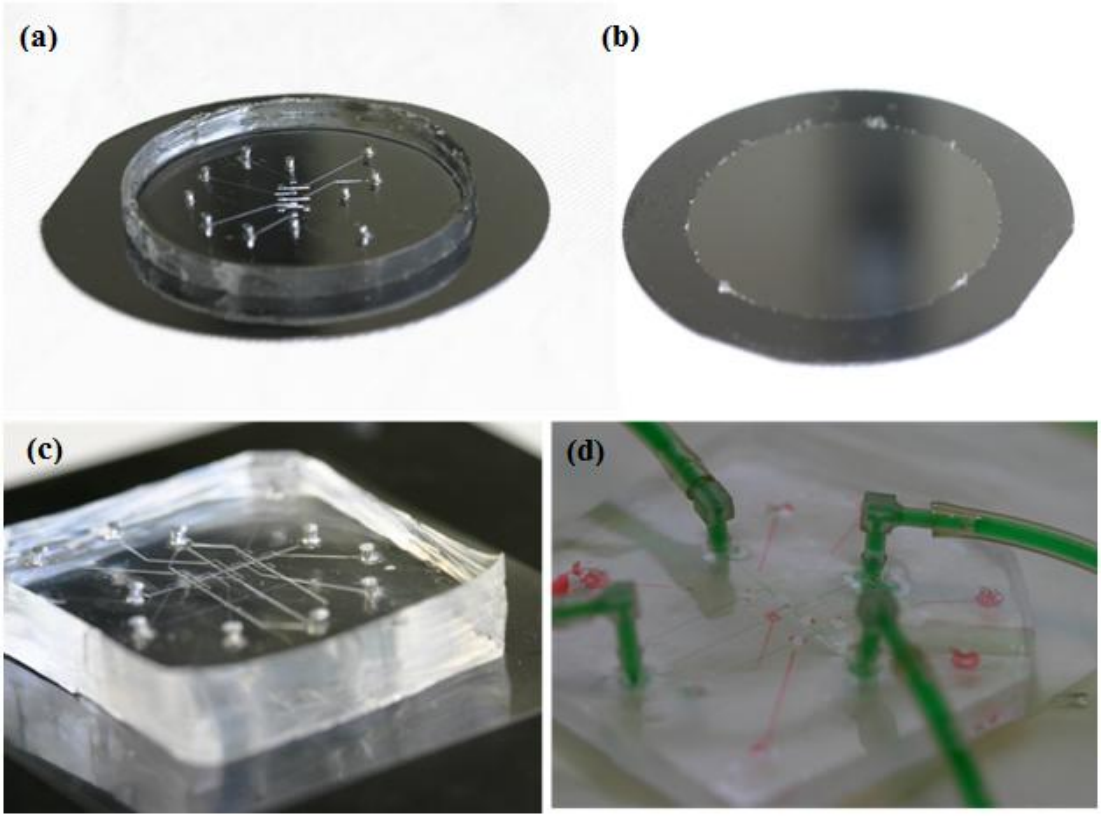

Figure 8.3: *Multi-layer* C. elegans *sorter device (a) The pneumatic layer is attached to the thin membrane and (b) peeled off after baking on a hotplate for 20 min at 80℃ (c) The fluidic layer is attached to the pneumatic layer and the thin membrane by careful alignment. (d) Image showing the different layers of the device. Red dye refers to the gas layer at the top, while green indicates the fluidic layer. Tygon tubes are connected to the inlet and outlet of the horizontal and vertical measurement channels.*

8.3 Experimental Setup

8.3.1 Microvalve operation

The concept of pneumatically actuated microvalves using multilayer soft-lithography was utilized for various microfluidic systems previously as reported by [100-106]. A simple analogy for the PDMS microvalve operation is a person stepping on a garden hose, and, when the applied pressure sufficiently deforms the hose, the flow within the hose will be restricted. A PDMS microvalve typically consists of a thin elastic membrane sandwiched in between two layers, namely a pneumatic layer on top and a fluidic layer at the bottom. When pressurized gas is applied to the upper pneumatic channel, the thin membrane in the middle is deflected, hence closing the fluidic channel underneath. The thin membrane was fabricated by spinning approximately 1 ml of PDMS onto a pre-treated with TMCS wafer for 30 s at 3000 rpm, which resulted in the thickness ~20 μm. The valve was closed with a pneumatic pressure of 150kPa. Figure 8.4(a) shows the fluidic layer consisting of green dye fluid injected underneath an open microvalve of the pneumatic layer. When the valve is closed, the fluid flow is restricted as illustrated in Fig. 8.4(b). In order to demonstrate the microvalve operation, a string of 100 μm beads was initially introduced into the channel and the valve was closed to stop the beads from moving (see Fig. 8.4(c)). Later, a single bead was isolated and the closed valve managed to stop the single bead from moving (Fig. 8.4(d)). *C. elegans* were then loaded into the channel and the microvalve proved to work efficiently by closing the channel to stop the nematode movement. An SEM image showing the cross-sectional view of the microvalve is shown in Fig. 8.4(e).

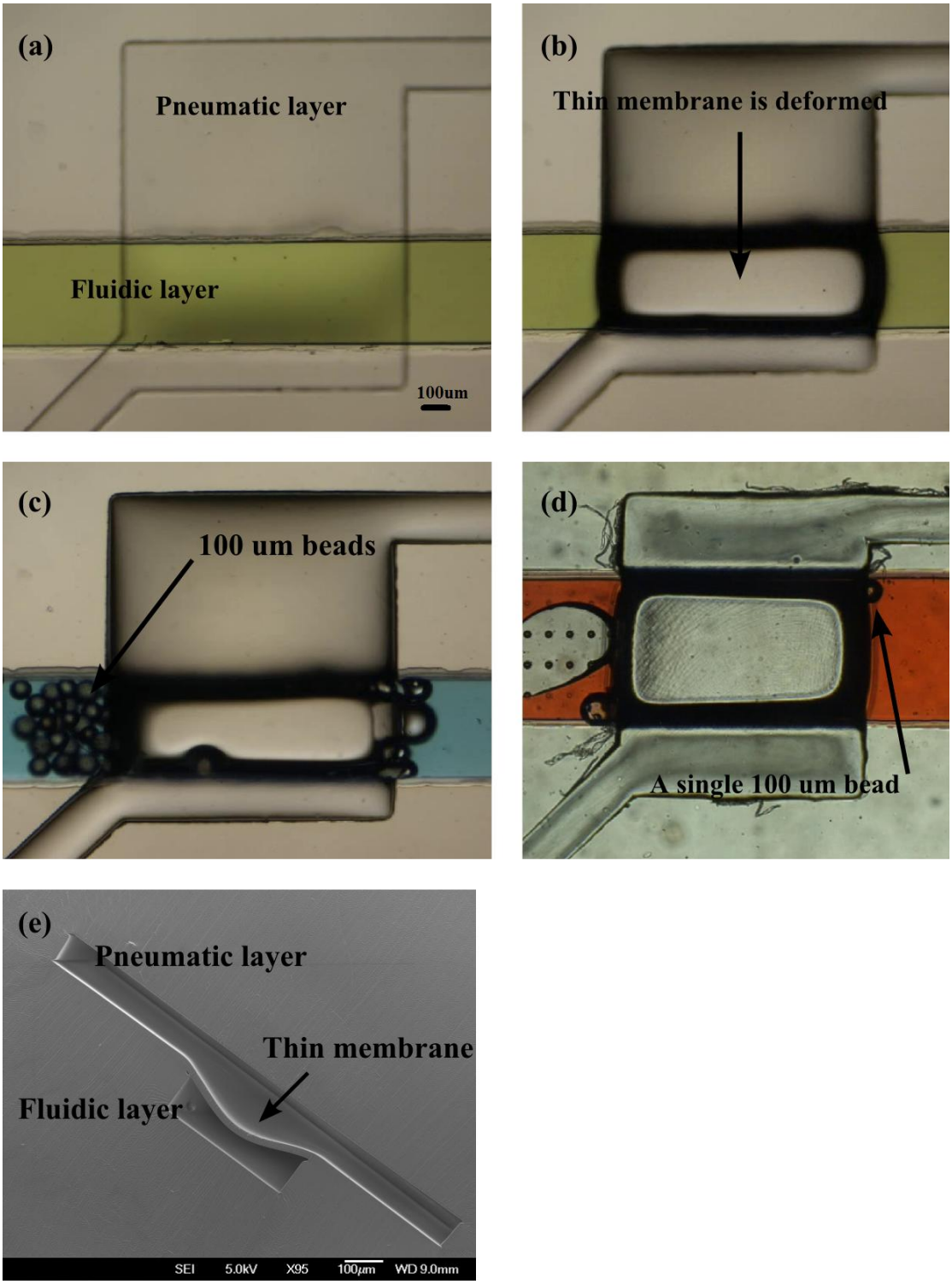

Figure 8.4: *Micrographs showing operation of the PDMS microvalves (a) Open valve (b) Stopping fluid flow and (c)&(d) 100 μm beads. SEM image of a cross-sectional view of the microvalve is shown in (e).*

8.3.2 Microfluidic device performance validation

Due to the addition of the microvalves, the PDMS device requires additional interface capability in order to control the microvalve operation and also the insertion of the worm into the device inlet. Figure 8.5 shows the experimental setup of the PDMS microfluidic device. All the inlets for the fluidic layer and the pneumatic layer are accessed from the top of the device, with tygon tubing (Cole-Parmer) inserted into each inlet. Fluidic inlets are connected to a PHD 2000 syringe pump (Harvard Apparatus, Holliston, MA) for continuous fluid flow actuation. The syringe pump allows precise control of the fluid flow rate from 0.0001 µl/hr to 220.82 ml/min with an accuracy of ±1%. The microfluidic device was placed under an inverted microscope (Nikon Eclipse 80i) for worm visualization.

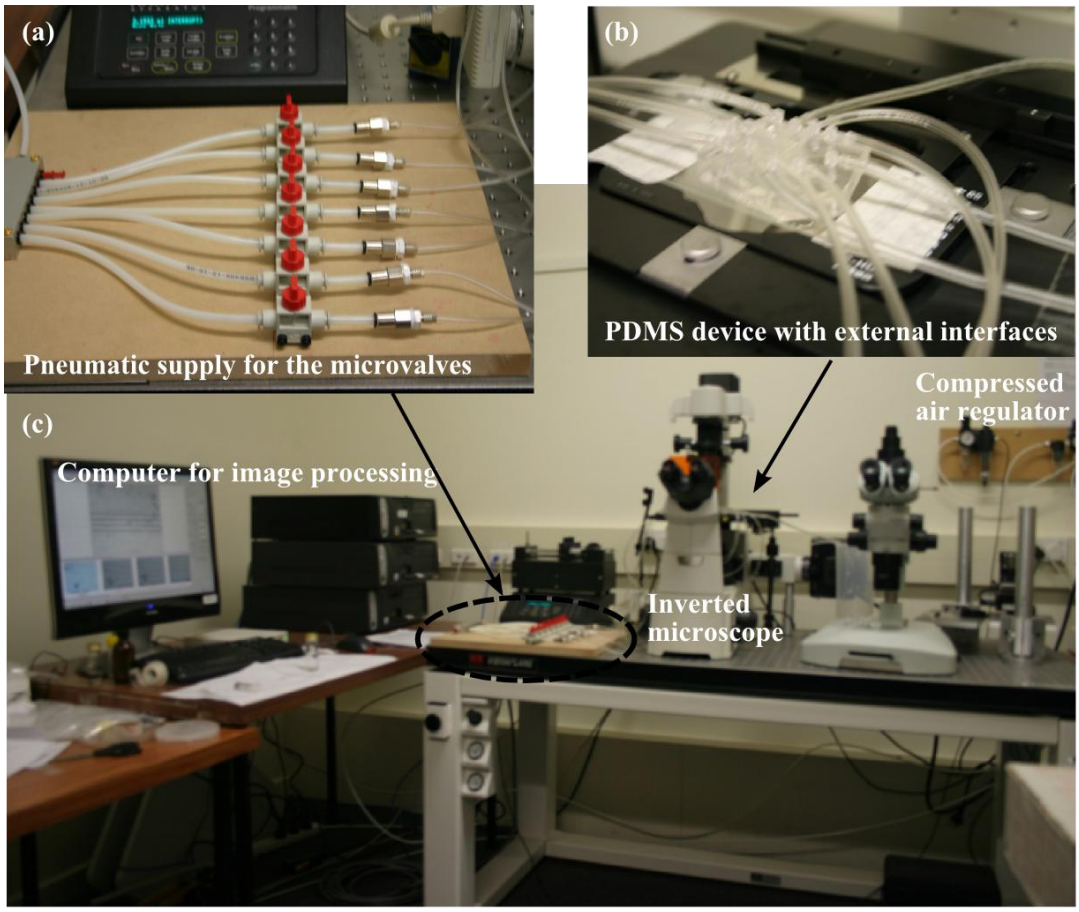

Figure 8.5: *Photographs of the experimental setup used to perform* C. elegans *manipulation for force measurement application. (a) Pneumatic supply and syringe pump. (b) PDMS device with fluidic and pneumatic interfacing. (c) Inverted optical microscope stage and PC for image processing.*

Prior to worm loading, de-ionized (DI) water was injected into the device channel to provide a moisturized environment that is required for the worm to move naturally. The worms were loaded from the inlets of the loading channel. Continuous fluid flow from the fluidic inlet to the outlet is provided by a syringe pump to assist the worms' movement. The opening and closing of the valves was controlled using a series of manifolds connected to a compressed air regulator (see Fig 8.5(a)).

Adult wild-type *C. elegans* were used to demonstrate the performance of the microfluidic device. In general, when the worm is loaded into the inlet, it will move freely in the liquid-filled channel. When the selected valves were closed, the nematodes will have no choice but to swim into an open channel containing pillars, hence force measurement can be conducted.

The complete schematic of the microfluidic device is shown in Fig 8.6(a). As displayed in Fig. 8.6(b), the worms were initially loaded into the inlet of the horizontal channel. During this process, all the microvalves (numbered from 1 to 7) were initially closed, which can be seen in Fig. 8.6(c) by the example of closed Valve 1. The first step was to direct a single worm to Channel *C*. When the worm was visually confirmed to be inside the fluidic inlet, Valve 1 was opened (see Fig 8.6(d)). Once the worm moved past Valve 1, the valve was then closed again as shown in Fig. 8.6(e) in order to prevent the worm from reversing back to the inlet. During the experiment, the worm was observed to move forward until it reached Valve 2. Because the objective was to direct the worm movement into Channel *C*, Valve 2 was also closed (see Fig. 8.6(f)) and the worm was observed to move back towards Valve 1. Since Valve 1 was still closed, the worm moved towards Valve 7 located in Channel *C* and shown in Fig. 8.6(g). The valve was initially closed before the worm arrived (see Fig. 8.6(h)) and was opened afterwards to allow the worm move towards the micropillars area. The latter is indicated in (Fig. 8.6(i)). Once the worm had passed the valve and moved inside the channel containing the micropillars, Valve 7 was closed again (see Fig. 8.6(j)) in order to keep the worm inside the measurement Channel *C*.

The same operation is repeated for the loading of other nematodes into the remaining channels. For example, in order to insert a loaded worm into channel *A*, only valves 4, 6 and 7 would be closed initially. Once the worm passed channel *C*, Valve 1 would be shut to ensure the worm's forward motion. Continuous fluid flow from the vertical fluidic inlet to the outlet would also assist the worms' motion into the measurement channel of choice. Valve 6 would then be closed in order to avoid the worm moving into Channel *B*. When the worm reaches channel *A*, Valve 5 would be closed to avoid the worm travelling back. Currently, the opening and closing of the valves is controlled manually but automated control of the microvalves using computer software should be developed in the future.

When all the worms have been directed to their respective measurement channel, the recording of the worm motion inside the micropillar array can be conducted as discussed in Chapter 5. By controlling the incorporated microvalves, the device is able to manipulate and direct individual worms into a certain channel for imaging and force measurement. As a result of having more than one channel, multiple force measurements of the worms can be performed hence increasing the throughput of data collection on the nematode locomotion study.

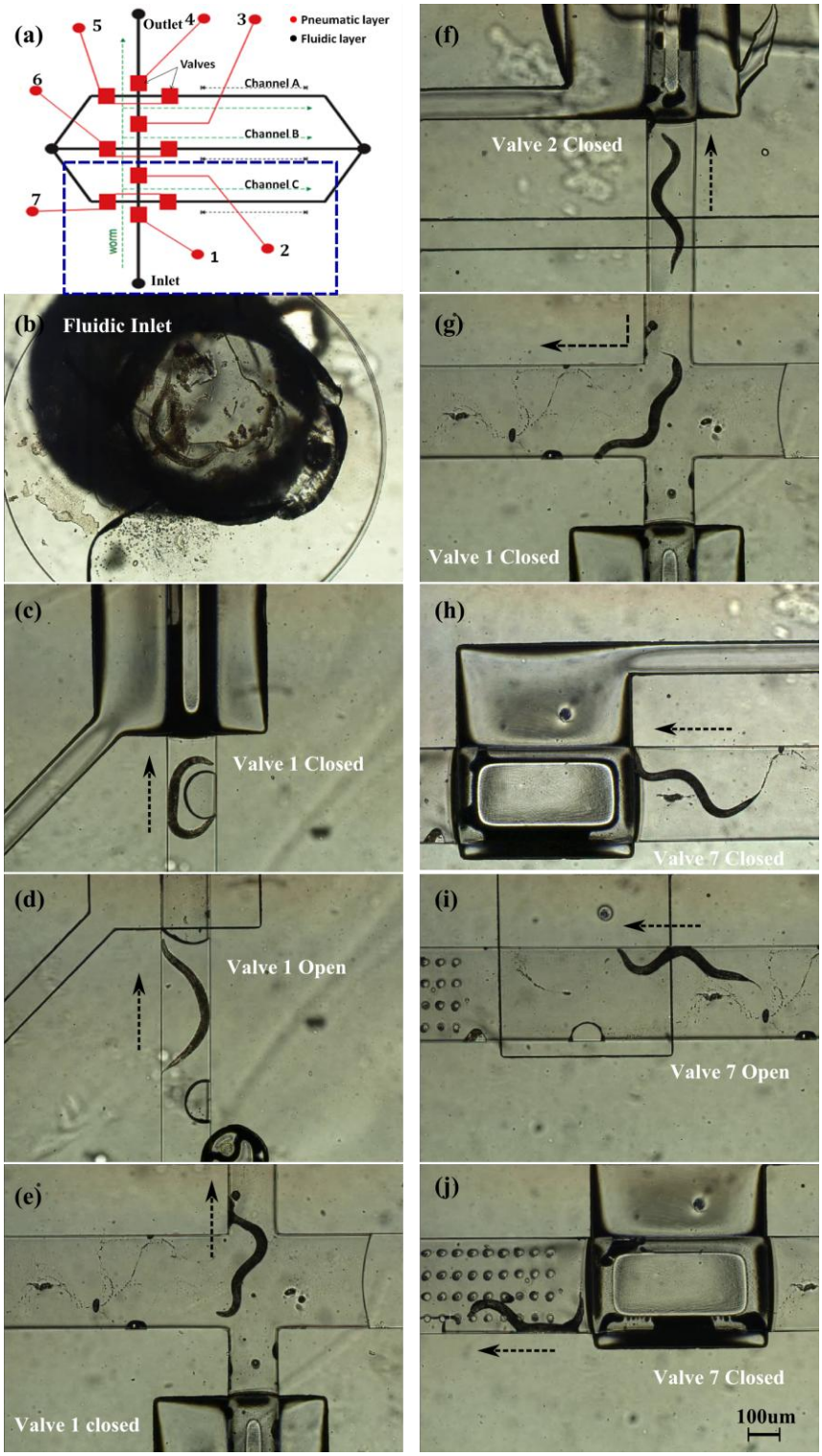

Figure 8.6: Device layout and operation. (a) Schematic of the microfluidic device. (b) Worms are loaded at the inlet. (c) Valve 1 is closed when worms are loaded. (d) Valve 1 is opened to allow worm moving forward. (e) Valve 1 is closed once worm passes it. (f)Valve 2 is closed to direct worm into Channel C. (g) Worm moves towards Valve 7 located in Channel C, (h) the valve was initially closed before the worm arrived and (i) was opened afterwards to allow the worm move towards the micropillars area. (j) Valve 7 was closed again in order to keep the worm inside the measurement Channel C. Scale bar applies to figure (b)-(j).

8.4 Summary

In this chapter, a microvalve-based microfluidic device for *C. elegans* force measurement and locomotion analysis was introduced and the applicability of the device was demonstrated. The device allows for easy manipulation and worm selection by controlling the incorporated microvalves to direct the worm movement into a certain channel, thus simplifying worm handling and making it automatable. In addition, the multiple channels included in the fluidic layer of the device can increase the collected experimental data. There are a few potential applications for the proposed device. The established system can be easily combined with existing screening and imaging systems for the application of drug resistance selection. For example, by improving the sealing performance of the microvalve, the multiple channels designed for force measurement application can be applied to different types of nematodes under different drugs exposures. Because drug resistance of the worms may be affiliated with the variation in the signalling-muscle-contraction pathways in the worm's body as demonstrated by [14, 15], it is possible to monitor the nematode drug resistance by determining the muscular locomotion forces of *C. elegans* under different drug or chemical exposure. Secondly, the development of the nematode *C. elegans* consists of four different stages, where each stage displays different sizes and specific genetic features. The inclusion of multiple channels in this work can be applied to investigate worm locomotion behaviour at different development stages. Having more than one measurement channel allows different pillar configurations to be included in the fluidic channels with dimensions tailored to the nematode size at each stage. In addition, this can also solve the negligible pillar deflection problem encountered from prototype device Design 1 (see Section 4.1.2.1), where the fluidic channel can be designed to match the amplitude of the nematode. Since the worm amplitude matches the size of the channel, it is anticipated that the worm locomotion can result in measurable deflection of the micropillars arranged in two parallel rows close to the channel wall. The microfluidic device discussed in this chapter also has the potential to facilitate high-throughput screening of force patterns in *C. elegans* locomotion behaviour study.

CHAPTER 9

Conclusions and Future Work

9.1 Thesis Summary and Conclusion

Knowledge of the locomotion forces of the model organism *C. elegans* can be advantageous for the development of therapies for muscle disorders, neurodegenerative diseases [1] and genetic disease observed in humans, such as muscular dystrophy [2-4]. Surprisingly, only three works specifically designed to study the worm forces had previously been reported. Although the relevant devices accomplished the function of force measurement capabilities, all three existing devices reviewed require complex microfabrication procedures. The first device limits the worm from locomotion as the worm is constrainted on a plate, while the inclusion of gold resistor as strain gauge and the single mode fiber optics cantilever in the other two devices requires highly complicated manufacturing process.

The work described in this thesis contributes to the development of *C. elegans* force measurement devices. For the first time, a force sensor which is capable of continuously measuring the horizontal equivalent force of *C. elegans* in motion is introduced. The system consists of a microfabricated PDMS device to load *C. elegans* in a matrix of micropillars in a channel, and an image processing algorithm to infer forces from measured micropillar deflections. The image processing algorithm was shown to detect the deflected pillar top circle and track its center point. The microdevice, sub-pixel resolution for visual tracking of the deflection, and experimental technique form an integrated system for measuring dynamic forces of moving *C. elegans* with force resolution of 3.13 μN for worm body width of 100 μm.

A method to estimate an equivalent point load to quantify the force exerted by the *C. elegans* on PDMS pillar was developed by considering the distributed force as a concentrated contact point force on the pillar. The worm-pillar contact point was

chosen and normalized to be at the middle of the pillar. The sensitivity of the system has been analyzed by calculating the force and the associated error based on the variation provided from the possible contact point with respect to the calculated force. This includes an investigation of the pillar stiffness and the force resolution based on varying the worm-pillar contact point, as well as calibration of the PDMS Young's Modulus.

Furthermore, the design optimization of the PDMS device has been described. This included the primary issue of pillar arrangement, wherein careful consideration has to be made in order to provide the best environment for force measurement experiments to succeed. Two initial designs have been reviewed and the design challenges that appeared during the process have been discussed. These include the worm squeezing into gaps adjacent to the channel wall that mimic the worms' burrowing behaviour, along with the negligible deflection of the pillars due to inapt pillar spacing and arrangement. Solutions to the aforementioned problem have been addressed and implemented in the final design.

Following this, the SU-8 mold fabrication procedures and the replication of the PDMS device using soft lithography were explained in detail. The production of high aspect-ratio features of reproducible quality is still a challenge. Particularly related to this research, the use of DRIE and changing the optical system of the MA6 mask aligner to match SU-8 photoresist compatibility could be potential solution for these issues.

The simplicity of the experimental setup, which only requires an off-the shelf digital camera and the PDMS device, make it readily accessible to most worm laboratories. To support this, the criteria for choosing the appropriate measurement pillars were reviewed and the detailed method of how to measure the pillar displacement using an image processing algorithm was discussed. Two sets of recorded videos of worm locomotion were analyzed in order to investigate the typical locomotion behaviour of *C. elegans*. For both sets of locomotion, the force magnitude and direction were obtained and the distinctive force pattern generated during the reverse motion was easily noticeable from the resulting plot. The information from the force pattern

exhibited by the worm during motion can also be used to identify the related worm body segments that were responsible for producing that certain amount of force. The experimental results demonstrate the efficacy of force measurement, leading to three preliminary but interesting findings on force patterns related to locomotion: (i) The generated force depends on the worm's head motion in particular when changing its movement direction, (ii) the worm sinusoidal body shape affects the exhibited force pattern, and (iii) the mid-body of the worm generates the maximum force level as predicted by existing theoretical analysis.

The main advantage of the proposed device is its capability to quantify multipoint forces of a moving *C. elegans* rather than single-point forces for a worm sample. This study demonstrated force data collection of up to ten simultaneous measurements from different worm body parts. This is a significant step forward as it enables researchers to explicitly quantify the relative difference in forces exerted by the worm's different body segments during movement. The device capability to determine multipoint forces of the nematode motion can also generate meaningful data to compare forces associated with different worm body muscles, gaining new understanding on how these muscles fire. The forces measured during locomotion in the micropillars could also be used to differentiate mutant phenotypes.

Apart from locomotion forces, the proposed device is also capable of conducting concurrent measurement of other locomotion parameters such as speed, amplitude and wavelength. This additional information can be useful to further quantify phenotypic behaviour of *C. elegans* and deepen the understanding of the theory behind worm locomotion forces measured in this work.

The relationship between *C. elegans* locomotion forces and their environment has been analyzed using two different micropillar layouts, namely the *'Honeycomb'* and *'Lattice'* design structure. Twelve wild-type *C. elegans* sample worms were tested during experiments to obtain a total of 4665 data points. The experimental results lead to several key findings. These include: (i) *C. elegans* locomotion forces are highly dependent on the structure of the surrounding environment, (ii) the worms' undulation frequency and locomotion speed increases steadily from the narrow spacing of

'*Honeycomb*' design to the wider spacing of '*Lattice*' pillar arrangement, and (iii) *C. elegans* maintained their natural sinusoidal movement in the microstructured device, despite the existence of the PDMS measurement pillars.

The results indicate that the microstructured environment significantly affects the worm's contraction force, locomotion speed and the undulation frequency. All three quantities depend on the micropillar spacing and arrangement. Nematode locomotion forces were greater in the *'Honeycomb'* structure and locomotion was enhanced inside the *'Lattice'* pillar arrangement. In comparison, the average locomotion forces in narrower spaced pillars increased by 50 to 64%, depending on the layout. The nematode navigation in the narrow pillar spacing particularly using the *'Honeycomb'* design was found to be relatively slow compared to the wider pillar spacing in the *'Lattice'* design.

The limitation of having to use PDMS as the substrate to measure *C. elegans* locomotion forces could be resolved using an alternative measurement technique based on the proposed pillar array. The experiments demonstrated in Chapter 7 provide preliminary findings of the force calculated from 5 different nematodes with the total of 366 measurements conducted. When moving on glass slides, it was found that the worms used the micropillar tips to facilitate their movement and it thus seems likely that the liquid on the glass slide surface enforced swimming motions which made movement unlike its conventional smooth sinusoidal wave crawling motion [5]. It is believed that the micropillars on the device assisted the worms by guiding their movement and at the same time deflected to indicate the applied forces. In addition to the microscope glass slide, this measurement technique can also be used to measure forces on other substrates, and worm locomotion behaviour in varying environment parameters can be investigated further. The combination of the conventional measurement technique with the findings reported show promise for biological measurements and other sensing application such as tactile force.

Finally, a microvalve-based microfluidic device for *C. elegans* force measurement and locomotion analysis was introduced where the feasibility of the device has also been demonstrated. The device allows easy manipulation and worm selection by

controlling the incorporated microvalves to direct the worm movement into a certain channel, thus making it fast to operate. In addition, the multiple channels included in the fluidic layer of the device can increase the collected experimental data. The established system can be easily combined with existing screening and imaging systems for the application of studying drug exposure. For example, the multiple channels accommodated for force measurement application can be applied to different types of nematodes under exposure to different drugs. The inclusion of multiple channels in this work can be applied to investigate worm locomotion behaviour at different development stages. Having more than one measurement channel also allows different pillar configurations to be included in the fluidic channels, thus facilitating high-throughput screening of force patterns in *C. elegans* locomotion.

In summary, a unique integrated system employing both PDMS micropillars and a visual feedback system to calculate the worm force has been developed. For the first time it is possible to measure the dynamic force of moving *C. elegans* simultaneously with other important locomotive metrics such as speed, wavelength and wave amplitude able to be collected. Extensive new experimental data about the force and locomotion patterns of *C. elegans* have been collected and the applicability of the system to nematode biology has been demonstrated, yielding new insight into worm behaviour. Additional functions of on-chip worm selection, sorting, and imaging have been integrated with the proposed device to point the way to future developments of fully integrated worm-on-a-chip devices.

9.2 Future Work

As discussed in Chapter 4, the production of high aspect-ratio PDMS micropillars is still a challenge. The pillar diameter needs to be sufficiently small as to allow deflection and at the same time conducting very sensitive force measurement. One possible option to resolve this issue is by using deep reactive-ion etching (DRIE), an anisotropic etching process that enables the creation of deep hole structures in the substrate. Though this facility is not available in the Nanofabrication laboratory in Canterbury University, collaboration can be made with other research institutes that have such equipment, namely Callaghan Innovation Research Ltd (formerly known as Industrial Research Ltd or IRL) in Wellington. There have been discussions with researchers from Callaghan Innovation Research Ltd on the possibility of using their DRIE, however at the time this research project was conducted the tool had not yet been commissioned. This can significantly increase the pillar sensitivity, and hence produce more accurate force measurement data.

Another possibility for future work is to study the associate muscles that the worm uses during worm locomotion. Since the nematode is transparent, it is possible to identify which body parts of the worm are in contact with the measurement pillars. By identifying the body part, it is possible to imply which muscle sets are in contact with the pillars. The current work presented here is not able to resolve individual muscle fibers or cells inside the worm body due to the image resolution used to compute the locomotion forces. By optimizing the pillar dimensions and experimental setup through inclusion of fluorescent myosin staining of muscle cells [107] a more detailed picture of the internal locomotion process should be obtainable.

Although the assay presented here focuses on wild type *C. elegans*, the method can be easily applied to its mutants and other organisms. The correlation between muscle arms and the contraction force can also be resolved by using *C. elegans* strains (RP472, RP526, RP247, and RP398) with different numbers of muscle arms [90]. During movement, *C. elegans* depends on the transduction of their touch receptor neurons in order to navigate its environment. For example, it has been reported that mechanosensory mutants (mec-4, mec-10) [37] fail to navigate in short agar pillar

structures. Thus, it will be of interest to quantify the force exerted from such mutants and compare it with the forces exhibited by wild type *C. elegans* reported here. The comparison should provide new insight into the connection between the worm's touch receptors and its locomotion system.

The information acquired from the force measurement data collected can be used for several potential applications. Because drug resistance of the worms may be affiliated with the variation in the signalling-muscle-contraction pathways in the worm's body, it is possible to monitor the nematode drug resistance by determining the muscular locomotion forces of *C. elegans* under different drug or chemical exposure. This can be helpful in the drug screening procedure often conducted in the research of pharmacology and drug development.

The work presented here can also be applied to investigate worm locomotion behaviour at different development stages. The *C. elegans* life cycle consists of four different stages, where each stage displays different sizes and specific genetic features. It would be beneficial to better understand the fundamental mechanism behind the growth of the organism and its biological development.

Finally, the integration of the microvalve with the PDMS micropillar-based on chip system discussed in Chapter 8 can be easily combined with existing screening and imaging systems [41]. The automation of the microvalves used to manipulate the nematode during experiments can facilitate high-throughput screening of force patterns in *C. elegans* locomotion behaviour.

References

[1] M. Dimitriadi, J. N. Sleigh, A. Walker, H. C. Chang, A. Sen, G. Kalloo, J. Harris, T. Barsby, M. B. Walsh, J. S. Satterlee, C. Li, D. Van Vactor, S. Artavanis-Tsakonas, and A. C. Hart, "Conserved Genes Act as Modifiers of Invertebrate SMN Loss of Function Defects," *PLoS Genetic*, vol. 6, p. e1001172, 2010.

[2] C. I. Bargmann, "Neurobiology of the Caenorhabditis elegans genome," *Science*, vol. 282, pp. 2028-33, 1998.

[3] J. E. Mendel, H. C. Korswagen, K. S. Liu, Y. M. Hajdu-Cronin, M. I. Simon, R. H. Plasterk, and P. W. Sternberg, "Participation of the protein Go in multiple aspects of behavior in C. elegans," *Science*, vol. 267, pp. 1652-5, 1995.

[4] L. S. Nelson, M. L. Rosoff, and C. Li, "Disruption of a neuropeptide gene, flp-1, causes multiple behavioral defects in Caenorhabditis elegans," *Science*, vol. 281, pp. 1686-90, 1998.

[5] X. N. Shen, J. Sznitman, P. Krajacic, T. Lamitina, and P. E. Arratia, "Undulatory Locomotion of Caenorhabditis elegans on Wet Surfaces," *Biophysical Journal*, vol. 102, pp. 2772-81, Jun 20 2012.

[6] S. Brenner, "The genetics of Caenorhabditis elegans," *Genetics*, vol. 77, pp. 71-94, 1974.

[7] *The Brain and Nervous System.*, accessed January 2010, Available: http://www.humanillnesses.com/Behavioral-Health-A-Br/The-Brain-and-Nervous-System.html

[8] C. I. Bargmann, "Chemosensation in C. elegans," in *WormBook*, M. Chalfie and J. E. Mendel, Eds., ed, 2006.

[9] S. J. Dixon and P. J. Roy, "Muscle arm development in C. elegans," *Development* vol. 132, pp. 3079-3092, 2005.

[10] T. Wakabayashi, I. Kitagawa, and R. Shingai, "Neurons regulating the duration of forward locomotion in Caenorhabditis elegans," *Neurosci Res,* vol. 50, pp. 103-11, Sep 2004.

[11] K. Hoshi and R. Shingai, "Computer-driven automatic identification of locomotion states in Caenorhabditis elegans," *J Neurosci Methods,* vol. 157, pp. 355-63, Oct 30 2006.

[12] W. Wang, Y. Sun, S. J. Dixon, M. Alexander, and P. J. Roy, "An Automated Micropositioning System for Investigating C. Elegans Locomotive Behavior," *Journal of Laboratory Automation,* vol. 14, pp. 269-276, 2009.

[13] K. Nishikawa, A. A. Biewener, P. Aerts, A. N. Ahn, H. J. Chiel, M. A. Daley, T. L. Daniel, R. J. Full, M. E. Hale, T. L. Hedrick, A. K. Lappin, T. R. Nichols, R. D. Quinn, R. A. Satterlie, and B. Szymik, "Neuromechanics: an integrative approach for understanding motor control," *Integrative and Comparative Biology,* vol. 47, pp. 16-54, 2007.

[14] E. Devaney, A. D. Winter, and C. Britton, "microRNAs: a role in drug resistance in parasitic nematodes?," *Trends in Parasitology,* vol. 26, pp. 428-33, 2010.

[15] R. J. Martin, G. Bai, C. L. Clark, and A. P. Robertson, "Methyridine (2-[2-methoxyethyl]-pyridine]) and levamisole activate different ACh receptor subtypes in nematode parasites: a new lead for levamisole-resistance," *British Journal of Pharmacology,* vol. 140, pp. 1068-1076, 2003.

[16] Y. Sun, K.-T. Wan, K. P. Roberts, J. C. Bischof, and B. J. Nelson, "Mechanical property characterization of the mouse zona pellucid," *IEEE Transactions on NanoBioscience,* vol. 2, pp. 279-286, 2003.

[17] Y. Sun and B. J. Nelson, "Biological cell injection using an autonomous microrobotic system," *International Journal of Robotics,* vol. 21, pp. 861-868, 2002.

[18] Y. Sun, D. P. Potasek, S. N. Fry, and B. J. Nelson, "Characterizing fruit fly flight behavior using a microforce sensor with a new comb drive

configuration," in *17th IEEE International Conference on Micro Electro Mechanical Systems (MEMS)*, Maastricht, The Netherlands, 2004, pp. 837-840.

[19] G. Lin, R. E. Palmer, K. S. Pister, and K. P. Roos, "Miniature heart cell force transducer system implemented in MEMS technology," *IEEE Transactions on Bio-medical Engineering*, vol. 48, pp. 996-1006, 2001.

[20] M. E. Fauver, D. L. Dunaway, D. H. Lilienfeld, H. G. Craighead, and G. H. Pollack, "Microfabricated cantilevers for measurement of subcellular and molecular forces," *IEEE Transactions on Bio-medical Engineering*, vol. 45, pp. 891-8, 1998.

[21] J. Conia, B. S. Edwards, and S. Voelkel, "The micro-robotic laboratory: optical trapping and scissing for the biologist," *Journal of Clinical Laboratory Analysis*, vol. 11, pp. 28-38, 1997.

[22] C. G.T., P. P. Lehenkari, and H. M.A., "Atomic force microscopy can be used to mechanically stimulate osteoblasts and evaluate cellular strain distributions," *Ultramicroscopy*, vol. 86, pp. 85-95, 2001.

[23] J. N. Fass and D. J. Odde, "Tensile force-dependent neurite elicitation via anti-beta1 integrin antibody-coated magnetic beads," *Biophysical Journal*, vol. 85, pp. 623-36, 2003.

[24] R. M. Hochmuth, "Micropipette aspiration of living cells," *Journal of Biomechanics*, vol. 33, pp. 15-22, 2000.

[25] W. Shi, H. Wen, B. Lin, and J. Qin, "Microfluidic Platform for the Study of Caenorhabditis elegans," *Topics in Current Chemistry*, vol. 304, pp. 323-38, 2011.

[26] A. Ben-Yakar, N. Chronis, and H. Lu, "Microfluidics for the analysis of behavior, nerve regeneration, and neural cell biology in C. elegans," *Current Opinion in Neurobiology*, vol. 19, pp. 561-7, 2009.

[27] N. Chronis, "Worm chips: Microtools for C. elegans biology," *Lab Chip,* vol. 10, pp. 432-437, 2010.

[28] H. Ma, L. Jiang, W. Shi, J. Qin, and B. Lin, "A programmable microvalve-based microfluidic array for characterization of neurotoxin-induced responses of individual C. elegans," *Biomicrofluidics,* vol. 3, p. 44114, 2009.

[29] W. Shi, H. Wen, Y. Lu, Y. Shi, B. Lin, and J. Qin, "Droplet microfluidics for characterizing the neurotoxin-induced responses in individual Caenorhabditis elegans," *Lab Chip,* vol. 10, pp. 2855-63, 2010.

[30] J. Qin and A. R. Wheeler, "Maze exploration and learning in C. elegans," *Lab Chip,* vol. 7, pp. 186-92, 2007.

[31] P. Rezai, A. Siddiqui, P. R. Selvaganapathy, and B. P. Gupta, "Behavior of Caenorhabditis elegans in alternating electric field and its application to their localization and control," *Applied Physics Letters,* vol. 96, 2010.

[32] S. Pandey, A. Joseph, R. Lycke, and A. Parashar, "Decision-Making by nematodes in complex microfluidic mazes," *Advances in Bioscience and Biotechnology,* vol. 2, pp. 409-415, 2011.

[33] S. E. Hulme, S. S. Shevkoplyas, A. P. McGuigan, J. Apfeld, W. Fontana, and G. M. Whitesides, "Lifespan-on-a-chip: microfluidic chambers for performing lifelong observation of C. elegans," *Lab chip,* vol. 10, pp. 589-97, 2010.

[34] D. Ying, K. Zhang, N. Li, X. Ai, Q. Liang, Y. Wang, and G. Luo, "A droplet-based microfluidic device for long-term culture and longitudinal observation of Caenorhabditis elegans," *BioChip Journal,* vol. 6, pp. 197-205, 2012.

[35] K. E. McCormick, B. E. Gaertner, M. Sottile, P. C. Phillips, and S. R. Lockery, "Microfluidic devices for analysis of spatial orientation behaviors in semi-restrained Caenorhabditis elegans," *PLoS ONE,* vol. 6, p. e25710, 2011.

[36] H. S. Chuang, D. M. Raizen, A. Lamb, N. Dabbish, and H. H. Bau, "Dielectrophoresis of Caenorhabditis elegans," *Lab Chip,* vol. 11, pp. 599-604, 2011.

[37] S. Park, H. Hwang, S. W. Nam, F. Martinez, R. H. Austin, and W. S. Ryu, "Enhanced Caenorhabditis elegans locomotion in a structured microfluidic environment," *PLoS ONE,* vol. 3, p. e2550, 2008.

[38] S. R. Lockery, K. J. Lawton, J. C. Doll, S. Faumont, S. M. Coulthard, T. R. Thiele, N. Chronis, K. E. McCormick, M. B. Goodman, and B. L. Pruitt, "Artificial dirt: microfluidic substrates for nematode neurobiology and behavior," *Journal of Neurophysiology*, vol. 99, pp. 3136-43, 2008.

[39] A. Parashar, R. Lycke, J. A. Carr, and S. Pandey, "Amplitude-modulated sinusoidal microchannels for observing adaptability in C. elegans locomotion," *Biomicrofluidics*, vol. 5, p. 24112, 2011.

[40] T. V. Chokshi, A. Ben-Yakar, and N. Chronis, "CO2 and compressive immobilization of C. elegans on-chip," *Lab Chip,* vol. 9, pp. 151-157, 2009.

[41] F. Zeng, C. B. Rohde, and M. F. Yanik, "Sub-cellular precision on-chip small-animal immobilization, multi-photon imaging and femtosecond-laser manipulation," *Lab Chip* pp. 653-656, 2008.

[42] S. E. Hulme, S. S. Shevkoplyas, J. Apfeld, W. Fontana, and G. M. Whitesides, "A microfabricated array of clamps for immobilizing and imaging C. elegans," *Lab Chip,* vol. 7, pp. 1515-23, 2007.

[43] M. F. Yanik, C. B. Rohde, and C. Pardo-Martin, "Technologies for Micromanipulating, Imaging, and Phenotyping Small Invertebrates and Vertebrates," *Annual Review of Biomedical Engineering,* vol. 13, pp. 185-217, 2011.

[44] J. A. Carr, A. Parashar, R. Gibson, A. P. Robertson, R. J. Martin, and S. Pandey, "A microfluidic platform for high-sensitivity, real-time drug screening on C. elegans and parasitic nematodes," *Lab Chip,* vol. 11, pp. 2385-96, 2011.

[45] J. Krajniak and H. Lu, "Long-term high-resolution imaging and culture of C. elegans in chip-gel hybrid microfluidic device for developmental studies," *Lab Chip,* vol. 10, pp. 1862-8, 2010.

[46] B. Han, D. Kim, U. H. Ko, and J. H. Shin, "A sorting strategy for C. elegans based on size-dependent motility and electrotaxis in a micro-structured channel," *Lab Chip*, vol. 12, pp. 4128-34, 2012.

[47] X. Maniere, F. Lebois, I. Matic, B. Ladoux, J. M. Di Meglio, and P. Hersen, "Running worms: C. elegans self-sorting by electrotaxis," *PLoS One*, vol. 6, p. e16637, 2011.

[48] K. Chung, M. M. Crane, and H. Lu, "Automated on-chip rapid microscopy, phenotyping and sorting of C. elegans," *Nature Methods*, vol. 5, pp. 637-643, 2008.

[49] C. B. Rohde, F. Zeng, R. Gonzalez-Rubio, M. Angel, and M. F. Yanik, "Microfluidic system for on-chip high-throughput whole-animal sorting and screening at subcellular resolution," *Proceedings of the National Academy of Sciences*, vol. 104, pp. 13891-13895, 2007.

[50] M. Pomeroy, A. Ferrante, G. O'Connor, and W. P. Hansen, Application Note: Automated Detection and Sorting of C.elegans at Different Development Stages From a Mixed Population, Somerville, USA.

[51] *National Center for Biotechnology Information.*, accessed September 2009, Available: http://www.ncbi.nlm.nih.gov/pubmed

[52] S. J. Park, M. B. Goodman, and B. L. Pruitt, "Analysis of nematode mechanics by piezoresistive displacement clamp," *Proceedings of the National Academy of Sciences*, vol. 104, pp. 17376-81, 2007.

[53] S. J. Park, B. Petzold, M. B. Goodman, and B. L. Pruitt, "Piezoresistive Cantilever-based Force-Clamp System for the Study of Mechanotransduction in C. Elegans," in *IEEE 22nd International Conference on Micro Electro Mechanical Systems (MEMS)*, Sorrento, 2009, pp. 188-191.

[54] J. C. Doll, N. Harjee, N. Klejwa, R. Kwon, S. M. Coulthard, B. Petzold, M. B. Goodman, and B. L. Pruitt, "SU-8 force sensing pillar arrays for biological measurements," *Lab Chip*, vol. 9, pp. 1449-54, 2009.

[55] W. S. Ryu and A. D. Samuel, "Thermotaxis in Caenorhabditis elegans analyzed by measuring responses to defined Thermal stimuli," *Journal of Neuroscience,* vol. 22, pp. 5727-33, 2002.

[56] P. Liu, D. Mao, R. J. Martin, and L. Dong, "An integrated fiber-optic microfluidic device for detection of muscular force generation of microscopic nematodes," *Lab Chip,* vol. 12, pp. 3458-66, 2012.

[57] K. A. Beningo and Y.-L. Wang, "Flexible substrata for the detection of cellular traction forces," *Trends in cell biology,* vol. 12, pp. 79-84, 2002.

[58] W. F. Hughes and J. A. Brighton, *Schaum's Outline of Theory and Problems of Fluid Dynamics*. New York: McGraw-Hill, 1999.

[59] A. C. Ugural and S. K. Fenster, *Advanced Strength and Applied Elasticity*. NJ: Prentice-Hall, 2003.

[60] H. Bruus, *Theoretical microfluidics*: Oxford U. Press, 2008.

[61] J. M. Gere and S. P. Timoshenko, *Mechanics of materials*: Cheltenham, U.K.: Stanley Thornes, 1999.

[62] X. Liu, W. H. Wang, B. M. Lansdorp, and Y. Sun, "Vision-based cellular force measurement using an elastic microfabricated device," *Journal of Micromechanics and Microengineering,* vol. 17, pp. 1281-1288, 2007.

[63] Y. Zhao, C. C. Lim, D. B. Sawyer, R. Liao, and X. Zhang, "Microchip for subcellular mechanics study in living cells," *Sensors and Actuators* vol. 114, pp. 1108-1115, 2006.

[64] Q. Cheng, Z. Sun, G. A. Meininger, and M. Almasri, "Note: Mechanical study of micromachined polydimethylsiloxane elastic microposts," *The Review of scientific instruments,* vol. 81, p. 106104, 2010.

[65] Y. Xiang and D. A. LaVan, "Analysis of soft cantilevers as force transducers," *Applied Physics Letters,* vol. 90, 2007.

[66] I.-K. Lin, Y.-M. Liao, Y. Liu, K.-S. Chen, and X. Zhang, "Elastic and Viscoelastic Characterization of Polydimethylsiloxane (PDMS) for Cell-Mechanics Applications," *MRS Online Proceedings Library*, vol. 1052, 2007.

[67] D. Armani, C. Liu, and N. Aluru, "Re-configurable fluid circuits by PDMS elastomer micromachining," in *Twelfth IEEE International Conference in Micro Electro Mechanical Systems (MEMS)*, Orlando, FL, USA, 1999.

[68] D. Fuard, T. Tzvetkova-Chevolleau, S. Decossas, P. Tracqui, and P. Schiavone, "Optimization of poly-di-methyl-siloxane (PDMS) substrates for studying cellular adhesion and motility," *Microelectronic Engineering*, vol. 85, pp. 1289-1293, 2008.

[69] O. du Roure, A. Saez, A. Buguin, R. H. Austin, P. Chavrier, P. Silberzan, and B. Ladoux, "Force mapping in epithelial cell migration," *Proceedings of the National Academy of Sciences*, vol. 102, pp. 2390-5, 2005.

[70] J. E. Mark, *The Polymer Data Handbook*, 2 ed.: Oxford University Press, Incorporated, 2009.

[71] H. Wen and J. Qin, "Analysis of Caenorhabditis elegans in microfluidic devices," *SCIENCE CHINA Chemistry*, vol. 55, pp. 484-493, 2012.

[72] Y. N. Xia and G. M. Whitesides, "Soft lithography," *Annual Review of Materials Science*, vol. 28, pp. 153-184, 1998.

[73] J. Liu, B. Cai, J. Zhu, G. Ding, X. Zhao, C. Yang, and D. Chen, "Process research of high aspect ratio microstructure using SU-8 resist," *Microsystem Technologies*, vol. 10, pp. 265-268, 2004.

[74] H. Lorenz, M. Despont, N. Fahrni, N. LaBianca, P. Renaud, and P. Vettiger, "SU-8: a low-cost negative resist for MEMS," *Journal of Micromechanics and Microengineering*, vol. 7, p. 121, 1997.

[75] *SU-8: A thick photo-resist for MEMS.*, accessed January 2010, Available: http://aveclafaux.freeservers.com/SU%2D8.htm

[76] Microchem. *Nano SU-8 2000 Negative Tone Photoresist Formulations 2002-2025*., accessed January 2010 Available: http://www.microchem.com/products/pdf/SU8_2002-2025.pdf

[77] *MicroChem SU-8 2000 Permanent Epoxy Resists*., accessed January 2010, Available: http://microchem.com/Prod-SU82000.htm

[78] S. K. Mitra and S. Chakraboty, *Microfluidics and Nanofluidics Handbook: Fabrication, Implementation, and Applications*: CRC Press, 2011.

[79] T. Kohlmeier and H. H. Gatzen, "Challenges in using photosensitive embedding material to planarize multi-layer coils for actuator systems," *Journal of Magnetism and Magnetic Materials,* vol. 242–245, Part 2, pp. 1149-1152, 2002.

[80] J. Zhang, M. Chan-Park, J. Miao, and T. Sun, "Reduction of diffraction effect for fabrication of very high aspect ratio microchannels in SU-8 over large area by soft cushion technology," *Microsystem Technologies,* vol. 11, pp. 519-525, 2005.

[81] L. Gitlin, P. Schulze, and D. Belder, "Rapid replication of master structures by double casting with PDMS," *Lab Chip,* vol. 9, pp. 3000-2, 2009.

[82] T. Stiernagle, "Maintenance of C. elegans," *WormBook,* pp. 1-11, 2006.

[83] Z. F. Altun and D. H. Hall. (2002-2006). *WormAtlas*., accessed August 2009, Available: http://www.wormatlas.org/

[84] (2000). *The Source for Microscopy Education*., accessed July 2011, Available: http://www.microscopyu.com/

[85] A. Ghanbari, V. Nock, R. J. Blaikie, J. G. Chase, X. Q. Chen, C. Hann, and W. H. Wang, "Force pattern characterization of Caenorhabditis elegans in motion," *International Journal of Computer Application Technology,* vol. 39, pp. 137-144, 2010.

[86] A. K. Corsi, "A biochemist's guide to Caenorhabditis elegans," *Analytical Biochemistry,* vol. 359, pp. 1-17, 2006.

[87] N. Tavernarakis and M. Driscoll, "Molecular modeling of mechanotransduction in the nematode Caenorhabditis elegans," *Annual Review Physiology*, vol. 59, pp. 659-89, 1997.

[88] B. C. Petzold, S. J. Park, P. Ponce, C. Roozeboom, C. Powell, M. B. Goodman, and B. L. Pruitt, "Caenorhabditis elegans body mechanics are regulated by body wall muscle tone," *Biophysical Journal*, vol. 100, pp. 1977-85, 2011.

[89] J. Gray, "Undulatory Propulsion," *Quarterly Journal of Microscopical Science*, vol. s3-94, pp. 551-578, 1953.

[90] W. H. Wang, Y. Sun, S. J. Dixon, M. Alexander, and P. J. Roy, "A micropositioning system with real-time feature extraction capability for quantifying C. elegans locomotive behavior," in *IEEE International Conference on Automation Science and Engineering (CASE)*, Scottsdale, AZ, USA, 2007, pp. 243-248.

[91] M. Chalfie, "A molecular model for mechanosensation in Caenorhabditis elegans," *Biological Bulletin*, vol. 192, p. 125, Feb 1997.

[92] N. Chronis, M. Zimmer, and C. I. Bargmann, "Microfluidics for in vivo imaging of neuronal and behavioral activity in Caenorhabditis elegans," *Nature Methods*, vol. 4, pp. 727-31, 2007.

[93] (2004). *ImageJ Image Processing and Analysis in Java.*, accessed February 2011, Available: http://rsb.info.nih.gov/ij/

[94] S. Berri, J. H. Boyle, M. Tassieri, I. A. Hope, and N. Cohen, "Forward locomotion of the nematode C. elegans is achieved through modulation of a single gait," *Journal of Human Frontier Science Program*, vol. 3, pp. 186-193, 2009.

[95] N. A. Croll, *The behaviour of nematodes : their activity, senses and responses*: London: Edward Arnold (Publishers) Ltd., 1970.

[96] J. T. Pierce-Shimomura, B. L. Chen, J. J. Mun, R. Ho, R. Sarkis, and S. L. McIntire, "Genetic analysis of crawling and swimming locomotory patterns in C. elegans," *Proceedings of the National Academy of Sciences* vol. 105, pp. 20982-7, 2008.

[97] J. Korta, D. A. Clark, C. V. Gabel, L. Mahadevan, and A. D. Samuel, "Mechanosensation and mechanical load modulate the locomotory gait of swimming C. elegans," *Journal of Experimental Biology,* vol. 210, pp. 2383-2389, 2007.

[98] C. Fang-Yen, M. Wyart, J. Xie, R. Kawai, T. Kodger, S. Chen, Q. Wen, and A. D. Samuel, "Biomechanical analysis of gait adaptation in the nematode Caenorhabditis elegans," *Proceedings of the National Academy of Sciences,* vol. 107, pp. 20323-8, 2010.

[99] N. A. Croll, "Components and patterns in the behaviour of the nematode Caenorhabditis elegans," *Journal of Zoology,* vol. 176, pp. 159-176, 1975.

[100] M. A. Unger, H. P. Chou, T. Thorsen, A. Scherer, and S. R. Quake, "Monolithic Microfabricated Valves and Pumps by Multilayer Soft Lithography," *Science,* vol. 288, pp. 113-116, 2000.

[101] S. R. Quake and A. Scherer, "From micro- to nanofabrication with soft materials," *Science (New York, N.Y),* vol. 290, pp. 1536-40, 2000.

[102] A. Y. Fu, H.-P. Chou, C. Spence, F. H. Arnold, and S. R. Quake, "An Integrated Microfabricated Cell Sorter," *Analytical Chemistry,* vol. 74, pp. 2451-2457, 2002.

[103] H.-P. Chou, M. Unger, and S. Quake, "A Microfabricated Rotary Pump," *Biomedical Microdevices,* vol. 3, pp. 323-330, 2001.

[104] J. Liu, M. Enzelberger, and S. Quake, "A nanoliter rotary device for polymerase chain reaction," *Electrophoresis,* vol. 23, pp. 1531-1536, 2002.

[105] J. Liu, C. Hansen, and S. R. Quake, "Solving the “World-to-Chip” Interface Problem with a Microfluidic Matrix," *Analytical Chemistry*, vol. 75, pp. 4718-4723, 2003.

[106] T. Thorsen, S. J. Maerkl, and S. R. Quake, "Microfluidic Large-Scale Integration," *Science*, vol. 298, pp. 580-584, 2002.

[107] G. M. Benian and H. F. Epstein, "Caenorhabditis elegans muscle: a genetic and molecular model for protein interactions in the heart," *Circulation Research*, vol. 109, pp. 1082-95, 2011.